Membrane and Performance Study in Polymer Electrolyte Membrane Fuel Cells and Hydrogen Bromine Redox Flow Batteries

A Dissertation Presented for the
Doctor of Philosophy
Degree
The University of Tennessee, Knoxville

Yujia Bai
December 2013

Copyright © 2013 by Yujia Bai
All rights reserved.

Dedication

To my role model, my mentor, my beloved grandfather
Ji-Wen, Huo

Acknowledgements

I would like to express my deep gratitude to Prof. Thomas Zawodzinski for his continuous support and guidance during my tenure in graduate school. I would like to thank Dr. Matthew Mench, Dr. Robert Counce and Dr. Alexander Papandrew for serving on my dissertation committee; especially, Dr. Alexander Papndrew for the advice, expertise and time he shared with me during my research. I would like to thank my whole team from University of Tennessee and ORNL; especially, Dr. Gabriel Goenaga, Dr. Douglas Aaron, Dr. Che-Nan Sun and Dr. Manale Maalouf for their gracious help during my research. Thanks also to Kai Kang, Yijia Zhang, Bo Yu, Naxiong Jin, Nan Zhang, Max Huang, Muzi Zheng, Jeffery Law and Xizi Cai for their encouragement and friendship throughout my project.

I would like to express my appreciation to the U.S. Department of Energy, Volkswagen Group and University of Tennessee for providing my studying and research funding. Thanks to 3M Company for providing the membrane samples, and special thanks to Dr. Steven Hamrock for the meaningful discussions with me about 3M-membrane structure and characterization.

Abstract

This dissertation represents the consideration of the problems of polymer electrolyte membrane fuel cells (PEMFC) and hydrogen-bromine redox flow batteries (RFB). Due to the importance of water management in PEMFCs, all the experiments were strictly controlled at different water hydration conditions. Water uptake and densities were measured for Nafion® and a series of 3M ionomer membranes. The thermodynamics of water and polymer was analyzed based on water uptake experiment and calorimetry. Furthermore, partial molar volumes (PMV) of water/membrane system was defined for the first time and used to analyze the interaction between water and polymers. Three states of water were identified.

The performance of hydrogen bromine redox flow batteries was investigated. The experimental conditions were varied and optimized with respects of cell temperature, electrolyte concentration, membrane types and electrode layers. In addition, more detailed study of battery kinetics and transport limit issues was implemented by inserting a dynamic hydrogen reference electrode (DHE). Electrochemical Impedance Spectroscopy (EIS) method was utilized to further separate the losses occurred during battery charging and discharging process. It is believed that the bromine/bromide existence in the membrane, carbon paper electrode and Pt catalyst could harm the cell performance. The effective control of bromine and bromide ions is the key to improve the cell performance.

Preface

This dissertation is ultimately based on the experiment and data from Yujia Bai with assistance of his research group in University of Tennessee and ORNL. This is an original intellectual product of the author Yujia Bai.

This dissertation has five parts, each of which focuses on a different aspect of PEM fuel cell and hydrogen bromine redox flow battery. Chapter 1 reviews the history and state of art of PEM fuel cells and redox flow batteries. The importance of membrane and water management in the battery is emphasized in this chapter. Chapter 2 analyzes the water and polymer interaction within the membrane using density measurement. Different states of water are analyzed by calculating the partial molar volume of water. Chapter 3 analyzes the performance of a hydrogen bromine redox flow battery. With in-situ polarization curve measurement, the features of cell kinetic, ohmic and mass transport losses are presented. Chapter 4 focuses on the kinetics of hydrogen bromine redox flow batteries. Some issues of polarization curves with this type of batteries are addressed in this chapter. Chapter 5 uses the electrochemical impedance spectroscopy (EIS) to separate the losses mentioned in Chapter 3 and 4 and further studies their mechanisms. The discussion of membrane hydration in this chapter is related to that of Chapter 2.

Table of Contents

Chapter 1 Literature Review 1

1.1 Polymer Electrolyte Membrane Fuel Cells 1

1.1.1 Applications of PEM Fuel Cell 2

1.1.2 Related Fundamental Research 3

1.1.2.1 Membrane. 4

1.1.2.2 Catalyst Layers. 9

1.1.2.3 Gas Diffusion Layers. 11

1.1.2.4 Other Components. 14

1.1.2.5 GDL/GFC Interface. 16

1.1.2.6 Stack. 18

1.2 Water Management 19

1.2.1 General Issues 19

1.2.2 Membrane Dehydration 22

1.2.3 Cell Flooding 23

1.2.4 Cathode Flooding 25

1.2.5 Anode Flooding 29

1.2.6 Flow Channel Flooding 29

1.3 Proton Exchange Membranes 30

1.3.1 Proton Conducting Mechanisms 31

1.3.2 Proton Exchange Membranes Synthesis 34

1.3.2.1 Perfluorinated Ionomeric Membranes. 34

1.3.2.2 Non-fluorinated Hydrocarbon Membranes. 35

1.3.2.3 Acid–base Complexes. 36

1.3.3 Modification of Proton Exchange Membranes 37

1.4 Hydrogen Bromine Redox Flow Battery 40

1.4.1 Introduction 40

1.4.2 Transport Phenomena 44

1.4.3 Bromine Crossover and Poisoning Effect 44

1.4.4 Redox Reaction and Kinetics of the Flow Battery 47

1.4.5 Cell Design and Modeling 48

1.4.5.1 Membrane. 48

1.4.5.2 Electrodes. 49

1.4.6 Polysulfide Bromine Redox Flow Battery 49

Chapter 2 Density Measurement and Partial Molar Volume Analysis of Membranes for Polymer Electrolyte Membrane Fuel Cells 51

2.1 Introduction 51

2.2. Experiment 54

2.2.1 Materials 54

2.2.2 Water Uptake 55

2.2.3 Gas Displacement Pycnometry 55

2.2.4 Calorimetry 56

2.3 Result and Discussion 57

2.3.1 Water Uptake 57

2.3.2 Enthalpy 60

2.3.3 Free Energy 62

2.3.4 Density 64

2.3.5 Partial Molar Volume 70

2.3.5.1 Calculation....70

2.3.5.2 Partial Molar Volume....73

3.4. Conclusion....81

Chapter 3 Performance Study of Hydrogen Bromine Redox Flow Batteries... 83

3.1. Introduction....83

3.2. Experiment....85

3.2.1 Cell Configuration....85

3.2.2 Acid Uptake and Conductivity....87

3.2.3 Dynamic Hydrogen Electrode....88

3.3. Results and Discussion....90

3.3.1 Acid/Water Uptake and Conductivity Measurement....90

3.3.2 Cell Performance....95

3.4 Conclusion....107

Chapter 4 Kinetic Study of the Hydrogen Bromine Rodox Batteries....108

4.1 Introduction....108

4.2 Experiment....109

4.2.1 Materials and Cell Configuration....109

4.2.2 Polarization Curves....110

4.2.3 State of Charge....110

4.2.4 Electrochemical Impedance Spectroscopy....111

4.3 Results and Discussion....111

4.3.1 Tafel Plot and Kinetics....111

4.3.2 State of Charge....117

4.4 Conclusion....131

Chapter 5 Electrochemical Impedance Spectroscopy (EIS) Study of Hydrogen Bromine Redox Flow Battery.....132

5.1 Introduction.....132

5.2 Experiment.....134

5.3. Results and Discussion.....135

5.3.1 Regular Asymmetric Whole Cell.....137

5.3.2 Symmetric Cell.....147

5.4 Conclusion.....154

List of References.....155

Vita.....187

List of Tables

TABLE 1 EXCHANGE CURRENT OF H_2 ON PT AND BROMINE ON CARBON PAPER 116

TABLE 2 STATE OF CHARGE AND TURNOVER POTENTIAL DURING CYCLING 125

List of Figures

FIGURE 1.1 SCHEMATIC OF HYDROGEN/OXYGEN PEM FUEL CELLS 2

FIGURE 1.2 PROTON EXCHANGE MEMBRANE AT SUB-FREEZING TEMPERATURE 7

FIGURE 1.3. WATER UPTAKE AND WATER ACTIVITY 8

FIGURE 1.4. SEM GRAPHS OF AGED MEA 10

FIGURE 1.5 CARBON PAPER AND CARBON CLOTH FIBERS 12

FIGURE 1.6 WATER FLOODING PATTERN IN A PEM FUEL CELL. 24

FIGURE 1.7 EFFECT OF CATHODE FLOODING ON A PEM FUEL CELL PERFORMANCE 26

FIGURE 1.8 VOLTAGE REVERSAL EFFECT IN A PEM FUEL CELL. 28

FIGURE 1.9 WATER TRANSPORT IN MEMBRANE THROUGH HOPPING MECHANISM 32

FIGURE 1.10 WATER TRANSPORT IN MEMBRANE THROUGH VEHICULAR MECHANISM 33

FIGURE 1.11 A SCHEMATIC OF A REDOX FLOW BATTERY 43

FIGURE 1.12 CYCLIC VOLTAMMETRY OF BROMINE CONTAMINATED ELECTRODE. 46

FIGURE 2.1 MOLECULAR STRUCTURE OF NAFION AND 3MIONS. 52

FIGURE 2.2 WATER CONTENT OF 3M PFSA (EW636, 825 AND 1000). 58

FIGURE 2.3 WATER UPTAKE OF OBA, PFIA, NAFION®117 AND NAFION®211 59

FIGURE 2.4 HEAT GENERATED OF NAFION®117 IN CONTACT WITH LIQUID WATER 61

FIGURE 2.5 GIBBS FREE ENERGY OF WATER UPTAKE 63

FIGURE 2.6 DENSITY OF 3M PFSAS WITH DIFFERENT EQUIVALENT WEIGHTS. 66

FIGURE 2.7 DENSITIES OF NAFIONS® MEMBRANES 67

FIGURE 2.8 DENSITIES OF 3M PFIA AND OBA. 69

FIGURE 2.9 CURVE FITTING OF 3M PFSA825. 72

FIGURE 2.10 PARTIAL MOLAR VOLUME OF 3M PFSA825 75

FIGURE 2.11 PARTIAL MOLAR VOLUME OF 3M PFSA 636 76

FIGURE 2.12 PARTIAL MOLAR VOLUME OF 3M PFIA 77

FIGURE 2.13 PARTIAL MOLAR VOLUME OF OBA. 79

FIGURE 2.14 PARTIAL MOLAR VOLUME OF NAFION®211 80

FIGURE 3.1 SCHEMATIC OF A DHE IN THE HYDROGEN BROMINE REDOX FLOW BATTERY 89

FIGURE 3.2 WATER AND ACID CONTENT IN NAFION®117 IN HBR AQUEOUS SOLUTION. 92

FIGURE 3.3 ACID CONTENT VS. WATER CONTENT IN THE MEMBRANE 93

FIGURE 3.4 NAFION117 CONDUCTIVITY IN HBR ACID. 94

FIGURE 3.5 COMMERCIAL MEA DISCHARGING POLARIZATION CURVE 96

FIGURE 3.6 DISCHARGING POLARIZATION CURVE WITH INCREASED CONCENTRATION 98

FIGURE 3.7 TEMPERATURE DEPENDENCE OF CELL PERFORMANCE. 100

FIGURE 3.8 POLARIZATION CURVES WITH MORE CARBON PAPER LAYERS 102

FIGURE 3.9 POLARIZATION CURVES WITH 3M PFSA (A) AT 30 C; (B) AT 50 C 104

FIGURE 3.10 DISCHARGE AND CHARGE POLARIZATION CURVE WITH DHE 106

FIGURE 4.1 CHARGE AND DISCHARGE TAFEL PLOT FOR H/BR SYSTEM. 113

FIGURE 4.2 CURVE FITTING WITH 1ST ORDER BUTLER-VOLMER EQUATION. 115

FIGURE 4.3 DISCHARGING POLARIZATION CURVE OF THE WHOLE CELL. 119

FIGURE 4.4 SOC AND OCV CHANGE DURING DISCHARGING CYCLING. 120

FIGURE 4.5 DISCHARGE POLARIZATION CURVE AT DIFFERENT SOC. 123

FIGURE 4.6 POWER DENSITY AT DIFFERENT SOC. 124

FIGURE 4.7 THE CHANGE OF TURNOVER POTENTIAL DURING CYCLING 129

FIGURE 4.8 IN-SITU CYCLIC VOLTAMMETRY FOR HYDROGEN ON PT 130

FIGURE 5.1 EQUIVALENT CIRCUIT OF EIS 136

FIGURE 5.2 WHOLE CELL EIS 138

FIGURE 5.3 BROMINE ELECTRODE EIS 141

FIGURE 5.4 RESISTANCES AND CAPACITANCE AT THE BROMINE ELECTRODE 142

FIGURE 5.5 THE HYDROGEN ELECTRODE DISCHARGE POLARIZATION CURVE EIS 145

FIGURE 5.6 RESISTANCE AND CAPACITANCE FOR THE HYDROGEN ELECTRODE 146

FIGURE 5.7 HYDROGEN SYMMETRIC CELL CHARGE EIS 149

FIGURE 5.8 BROMINE SYMMETRIC CELL DISCHARGE EIS 150

FIGURE 5.9 HYDROGEN SYMMETRIC CELL DISCHARGE EIS 152

FIGURE 5.10 BROMINE SYMMETRIC CELL CHARGE EIS 153

Chapter 1

Literature Review

1.1 Polymer Electrolyte Membrane Fuel Cells

Due to the growing concerns about the depletion of petroleum based energy resources as well as the pollution from traditional energy systems, polymer electrolyte fuel cells (PEMFCs) have received more attention during the past decades. Fuel cells directly convert chemical energy stored in fuels such as hydrogen/oxygen to electrical energy. The high efficiencies and low emissions allow fuel cells to become the most promising energy converters for automotive, stationary, and portable applications. Consequently PEMFCs have increasingly been cited as a possible pathway to the reduction of greenhouse gas emissions.[1] A polymer electrolyte membrane (PEM) serving as a proton conductor is usually positioned in the middle of a PEMFC. Generally, a platinum (Pt) based catalyst is utilized for the electrochemical reactions. Fig 1.1 shows a schematic of a typical hydrogen/oxygen PEMFC, which represents the cell structure and reaction mechanism of most fuel cells. As shown in the Fig 1.1, hydrogen flows into the anode and oxygen flows into the cathode through the flow channels. The fuels diffuse through the gas diffusion layers (GDL) and reach the Pt based catalyst. On the Pt surface, the hydrogen is oxidized to protons, which transport through the proton exchange membrane and react with oxygen to produce water at the cathode. Meanwhile, the oxidation of hydrogen liberates electrons, which travel through the external circuit and

generate electricity. Water distribution in the cell plays an important role through out this process.

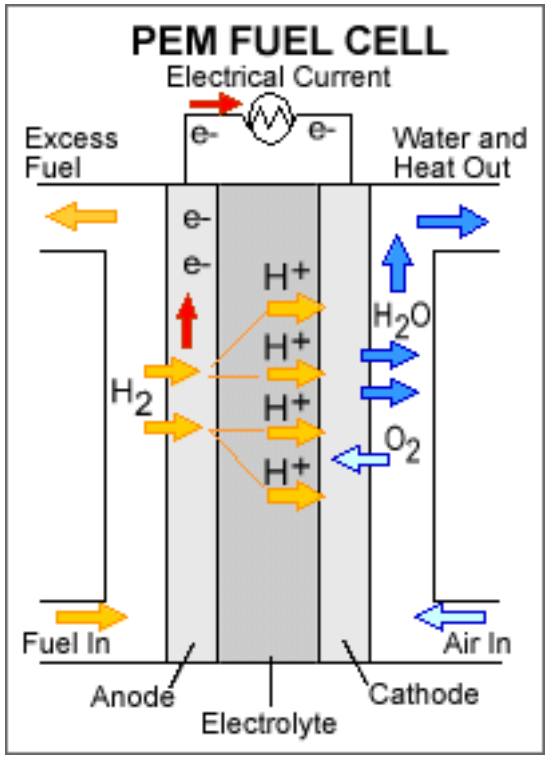


Figure 1.1 Schematic of Hydrogen/Oxygen PEM fuel cells[2]

1.1.1 Applications of PEM Fuel Cell

A major application of PEM fuel cells focuses on electrical automobiles[2] because of their high energy density and excellent dynamic characteristics compared with other types of fuel cells. In addition, PEMFCs are also considered for applications related to distributed/stationary and portable devices. Most major motor companies are developing fuel cell vehicles (FCV), and many models have been demonstrated such as: GM Hydrogen 1, Ford Demo (Focus), Daimler Chrysler, Honda FCX-V3, Toyota FCHV,

Nissan XTERRA FCV, VW Bora HyMotion, and Hyundai Santa Fe FCV.[3] In addition, distributed PEM fuel cell power systems are primarily focused on small scale (<250 kW) applications for decentralized use or households.[4] As for portable power supplies, the high energy density of hydrogen offers a possibility for modern electric devices to achieve longer operating periods. Major electronics companies, such as Toshiba, Sony, Motorola, LG, and Samsung, have in-house R&D units for portable fuel cells.[5]

The two greatest barriers to fuel cell commercialization are durability and cost.[6] The set goal of cell lifetime required by a commercial light-weight vehicle is 5000 operating hours and 40,000 hours for stationary power generation with less than 10% performance decay.[7] At present, most fuel cells exhibit major performance decay after about a thousand hours of operation.[8] 3M has successfully achieved a durability test of over 7500 h with their membrane electrode assembly (MEA).[9] Over the past several years, the fuel cell cost for automotive applications has been reduced from $275/kW to $61/kW, but is still more than twice as expensive as internal combustion engine systems.[10] One primary component of the fuel cell cost comes from the MEA, which consists of a Nafion® membrane coated with Pt-based catalyst layers. The Pt loading has been reduced by two orders of magnitude in the past decade and there is still room for further loading reduction.[11]

1.1.2 Related Fundamental Research

Various phenomena occur during fuel cell operation, including mass transport, heat transfer and chemical reactions. Further scientific breakthroughs are required to

overcome barriers related to cost and durability to enable fuel cell commercialization. These phenomena occur in various components, namely the membrane electrode assembly (MEA), micro-porous layer (MPL), gas flow channels (GFC), and bipolar plates (BP). Hydrogen and air flow down the anode and cathode GFCs, respectively, and through the porous GDLs/MPLs and diffuse into the catalyst layers (CLs). Hydrogen is oxidized at the anode CL and generates protons and electrons. The protons migrate through the membrane along with some water while electrons are conducted via carbon support to the anode current collector, and then to the cathode current collector via an external circuit. Meanwhile oxygen is reduced with protons and electrons at the cathode CL and forms water, which is then transported out of the cathode CL through cathode GDL/MPL. Heat is generated mainly in the cathode CL due to the sluggish oxygen reduction reaction (ORR), and is conducted out of the cell via the carbon in the electrode and the BPs. All of the transport phenomena are three-dimensional due to the complexity of the cell structure, and liquid water is present within the fuel cell under practical current loads.

1.1.2.1 Membrane. Generally, the proton exchange membranes used in PEM fuel cells are 20-200 μm thick. Nafion®, was first developed by the DuPont Company in 1960s and was followed by many other membrane based on Teflon® backbone. The Nafion®-based membranes are costly due to their complex fabrication process.[12] Many other companies are trying to decrease the production cost via polymer design or different manufacturing methods. Solvay Solexis is developing a short side-chain ionomer Hyflon® which exhibits a better performance and durability than Nafion®.

However, severe degradation has been observed for this membrane.[13] Phosphoric acid-doped polybenzimidazole (PBI) membranes are acknowleged to have high proton conductivity at temperatures up to 200 °C and low methanol/ethanol permeability. However, the low proton conductivity at low temperature and low oxygen solubility is problematic, as are stack material compatibility issues.[14]

To describe the transport issues in the membrane, structural studies were undertaken by Gierke and Hsu *et al*. using a cluster model. The cluster sizes depend on local water content, and the main driving force for proton transport is the electrolyte potential gradient. Two classic proton transport mechanisms are "vehicular" and "hopping" mechanisms. A "vehicular" diffusion mechanism describes one mode through which water supports proton transport. In the "vehicular" mode, protons in the form of hydronium ions (H_3O^+) migrate accross potential or proton concentration gradients.[15] A "hopping" mechanism takes place when sufficient water content is present and gathered around the acid groups. This forms a consistent water channel in between the acid groups for protons migrating directly from one site to another.[16,17] One of the most utilized water models is the empirical correlation developed by Springer *et al*.[18] for the Nafion®117 membrane:

$$\kappa = (0.005193\lambda - 0.00326)\exp[1268(\frac{1}{303} - \frac{1}{273 + T_{cell}})] \quad (1)$$

The water and proton conduction at subfreezing temperature were also studied. The Nafion® membrane remains conductive to protons due to the existence of non-frozen water in the membrane (Fig 1.2).[19–22] The water content λ, defined as the moles of water

per mole of acid sites, is directly related to the environmental water activity (Fig 1.3).[18] Springer *et al*. indicated that a discontinuity exists in the membrane water content between the membrane with liquid water and with saturated water vapor at equilibrium, where in both cases the water activity is unity. This phenomenon, generally referred to as ‘‘Schröeder’s paradox”, is observed in a wide variety of polymer materials and solvents.[23–25] Water diffusivity also depends on the local membrane water content.[18,26] In addition, the electro-osmotic drag which propels water from the anode to the cathode can be a function of water content.[27–32] Hydraulic permeation also can take place when liquid water is present on the membrane surface and provides a pressure gradient.[33] Many modeling studies were implemented in this area as well and showed the water content and its impact on fuels and performance etc.[34,35]

The transport phenomena in the membranes are crucial. Generally, the transport includes water, protons, and electrons as well as the fuels (H_2/O_2). Water plays a crucial role in the species transport. For instance, the ionic transport resistance is reflected in the cell ohmic loss overpotential. The hydration level of a membrane can tremendously affects ionic conductivity. Membrane drying effects can cause cracks and degradation issues. In addition, Springer *et al*. developed an empirical correlation between the proton conductivity and water content and the electro-osmotic drag coefficient and water content (Eq. (7)). A comprehensive model was developed by Weber and Newman, which took into account both liquid and vapor equilibrated transport modes using a single chemical potential driving force.[36]

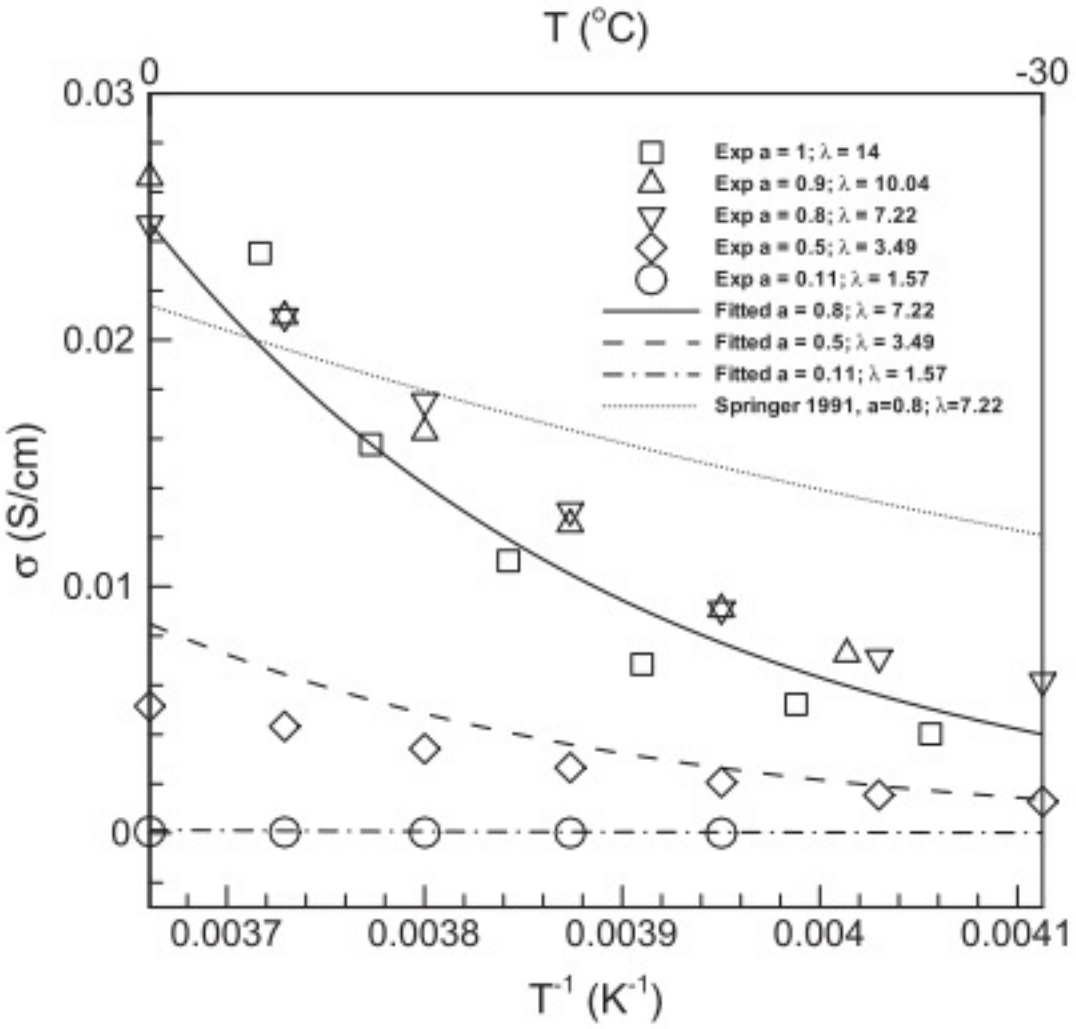


Figure 1.2 Proton Exchange Membrane at Sub-freezing Temperature

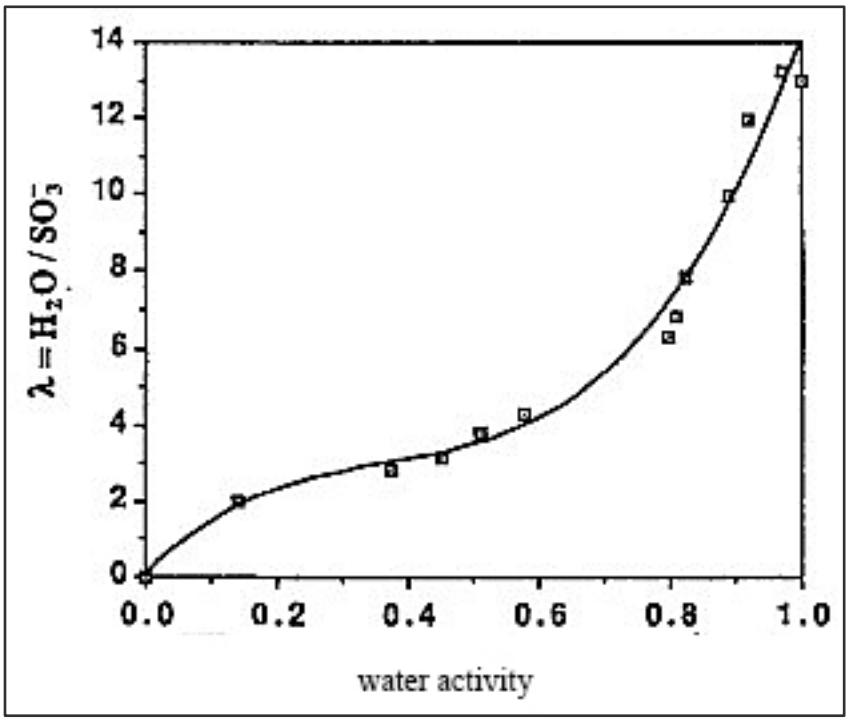


Figure 1.3. Water Uptake and Water Activity

1.1.2.2 Catalyst Layers. The catalyst layer (CL) is where the chemical reaction happens, and energy is transformed from chemicals to electricity. The typical PEM fuel cell CL consists of carbon/Pt catalyst particles and ionomer. Hydrogen fuel is oxidized in the anode whereas the ORR takes place in the cathode. The CL contributes a significant portion of the cost for a fuel cell due to the expense of Pt. Platinum and some of its alloys exhibit good catalyst kinetics in the PEM fuel cell. Reducing Pt loading is one of the main goals of developing CLs. 3M achieves 0.15 mg/cm^2 using PtCoMn alloy.[37] In addition, replacement of Pt with a less expensive precious metal or non-precious metal is another approach under intense research. Cobalt alloys or some of its complexes are sythesized and utilized in PEM fuel cells.[38–43]

Improving the Pt utilization or increasing the active area surface is another approach to reduce the Pt in use. Catalyst layers in the PEM fuel cell generally consist of several interconnected networks for proton, electron, and reactant transport, respectively. Mukherjee and Wang *et al*. proposed a numerical technique to digitally reconstruct this microstructure.[44] Despite the thickness, the reaction rates may vary significantly across the layer arising from transport resistance. Modeling was developed for oxygen and proton transport within the catalyst layer based on their reconstructed CL and predicted a spatially varied profile of reaction rate.[45–47]

The catalyst layer is susceptible to material degradation during operation. A primary degradation mechanism is Pt agglomeration or loss of activation sites. Ferreira *et al*. showed that platinum particles dissolved in the ionomer and reformed on larger particles, called Ostwald ripening.[48] X-ray Diffraction (XRD) analysis that platinum

particles may not be sufficiently anchored to the carbon support, move into the ionomer portion, and during cycling will coalesce onto bigger particles.[49] Platinum could possibly be transfered from the electrode into the membrane, which reduces the active catalyst area as well.[50–54] Fig 1.4 shows SEM micrographs of some aged MEAs, indicating a band of platinum inside the membrane on the cathode side during potential cycling. As the number of cycles is increased, the cathode becomes noticeably thinner decreasing from about 17 μm at 0 cycles to 14 μm at 10,000 cycles [55]. Due to the impurity of fuels, many chemicals such as NH_3,H_2S, CO, NO_x and SO_2 can impact the performance of the PEM fuel cell by poisoning the Pt.[56–61]

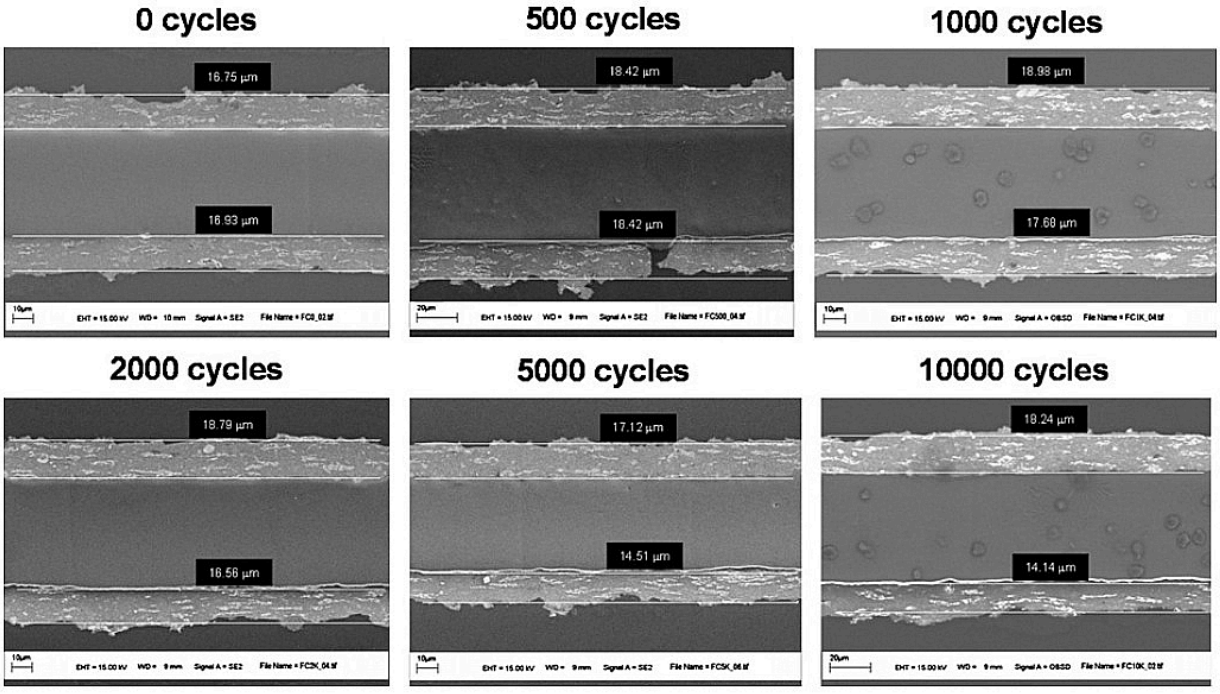


Figure 1.4. SEM Graphs of Aged MEA

In addition, water content and cathode flooding are closely related. Modeling of transport and electrochemical reactions in CLs on the cathode, where the ORR is sluggish and inefficient, is a common route in attempting to increase performance. The water content of the cathode CL directly affects the protonic conductivity in this domain and thus the reaction-rate distribution. To elucidate mechanisms of CL liquid-water transport and evaporation, some microstructural and surface prototyping models were made, which are also applied to explain CL microstructure and wettability.[62–66] Three different approaches for describing the cathode catalyst layer are a thin-film model, discrete-catalyst volume model, and agglomerate model. For a given electrode overpotential, the thin film model significantly over-predicts the current density and exaggerates the variation in current density both along and across the channel, and the agglomerate model predicts noticeable mass transport losses. In addition, the CL is usually thin, but may be subjected to mass transport limitation[46,47] or a considerable ohmic loss. In this regard, further reducing the CL thickness is necessary to improve its performance. A CL model that properly captures the key transport phenomena and reactions at the three-phase interface can be employed to optimize the CL thickness.

1.1.2.3 Gas Diffusion Layers. Gas diffusion layers (GDLs) and microporous layers (MPLs) have the following functions: (1) electronic connection between the bipolar plate with channel-land structure and the electrode; (2) passage for reactant transport and heat/water removal; (3) mechanical support to the MEA; and (4) protection of the catalyst layer from corrosion. Physical processes in the GDLs, in addition to diffusive transport, include bypass flow induced by in-plane pressure differences between

neighboring channels,[67,68] through-plane flow induced by mass source/sink due to electrochemical reactions,[69,70] heat transfer,[71,72] two-phase flow,[73–76] and electron transport.[34,77]

Transport inside GDLs is closely related to the GDL structural feature. The typical thickness of a GDL is approximately 100–300 μm. Carbon fiber is commonly used for the GDL: the fibers are either woven to form a cloth, or bonded by resins to form a paper (Fig 1.5).

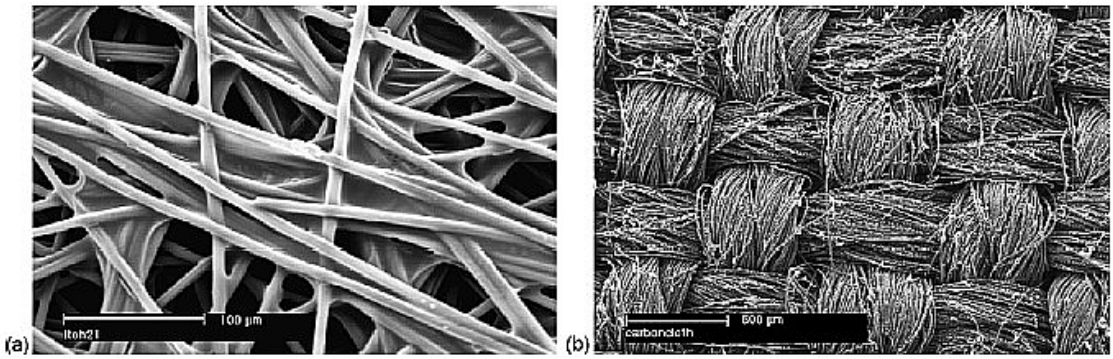


Figure 1.5 Carbon Paper and Carbon Cloth Fibers

Wang *et al*., using experimental data and numerical modeling comparison, studied the structural and cell performance difference between carbon cloth and paper. High tortuosity structure of the carbon paper leads to severe mass transport limitation under high humidified conditions, while carbon paper exhibits better performance under dry conditions.[78]

Multi-phase flow, originating from the water production by the ORR, is an important feature to control for fuel cell water management. The presence of excess liquid water hinders the reactant delivery to the catalyst sites, increasing the concentration polarization. This is generally referred to as the ‘‘flooding” phenomenon and can raise concerns of durability and performance reduction due to reactant starvation. The GDL materials are usually rendered hydrophobic to facilitate liquid water drainage. Polytetrafluoroethylene (PTFE) is frequently adopted to modify the GDL wettability.[79] Sinha and Wang used a pore-network model of GDLs, and found that liquid water preferentially flows through the connected hydrophilic pore network of a GDL with mixed wettability.[80] Pore-network models have also been employed by Gostick, and some macroscopic models of two-phase flow in the GDL have been developed.[81–85] The capillary pressure is usually expressed as a function of saturation via the Leverett function in the literature, and the capillary-pressure gradient is expressed as a function of the saturation gradient. To improve the multi-phase, particularly liquid, flow characteristics, an MPL can be added and placed between the GDL and CL. This layer is composed of carbon black powder with fine pore structure. Studies have shown that adding MPLs contribute to better water drainage characteristics and fuel cell performance. With the presence of the MPL, the GDL saturation point for water break-in is drastically lowered by 80%.[86] Although the reasoning may be flawed, it has been suggested that the MPL could act as a “valve” that drives water away from the electrodes to reduce electrode flooding.[87,88]

In addition, the macroscopic two-phase flow approach has been widely employed to model liquid-water transport through the GDL and MPL.[71,72,74,89,90] In this approach, capillary pressure is usually expressed as a function of saturation via the Leverett function.[91] To build the relationship between the capillary pressure and saturation of GDLs, first, the capillary pressure needs to be experimentally measured as a function of saturation;[92] the local capillary pressure is a function of pore radius and contact angle, which can be used to account for non-uniform hydrophilic and hydrophobic properties.

In addition, GDLs may be subjected to degradation after long-term operations, such as wettability change due to PTFE loss and fiber breakage arising from freeze/thaw cycling. The surface properties were evaluated, using a single-fiber contact-angle and surface-energy data of a wide GDL spectrum to delineate the effects of hydrophobic postprocessing treatments.[93] Wood and Borup further presented the cathode CL and GDL mass-transport overpotentials and analyzed the changes in a durability test.[94] They found little increase in the GDL mass-transport overpotential during the first period of about 500 h, but a substantial increase during the second period of approximately 500 h. Modeling degradation mechanisms are still lacking and remain a challenge at present, requiring further studies.

1.1.2.4 Other Components. Gas flow channels (GFCs) are important components of the PEM fuel cell and they supply and distribute hydrogen fuel and oxygen for reactions and remove byproduct water. They are normally carved into the bipolar plates with a typical cross-sectional dimension of around 1 mm. Insufficient supply of reactants will lead to hydrogen/oxygen starvation, reducing cell performance and durability.

Bipolar plates provide mechanical support over diffusion media and conductive passages for both heat and electron transport. Fabrication of bipolar plates, together with GFCs, can significantly affect fuel cell cost. Bipolar plate degradation, such as metal plate corrosion and graphite cracking, can occur and reduce fuel cell lifetime. Cooling channels can be machined within the bipolar plates, and are essential for waste heat removal for large-scale fuel cells. Local hot spot formation can degrade the membrane and cause pinhole or crack formation.

In GFCs, partially or fully humidified hydrogen and air are injected into the anode and cathode, respectively. Several types of flow fields have been developed, including parallel, serpentine, pintype, interdigitated, and porous media designs.[95] Jeon *et al*. investigated single channel, double channel, cyclic single channel, and symmetric single channel patterns, and found that fuel cell performance varies in different configurations.[96] Numerical simulation is implemented to investigate parallel channel flows with a small variation (<2%) of flow velocity among channels.[97–102]

Convection is the dominant force for species transport in a GFC, and the flow has been customarily treated using the single-phase approach, either considering the vapor phase as super-saturated or treating it as mist flow, but neither of these two approaches can accurately describe flow in GFCs. The streams frequently fall in the two-phase regime due to water addition from the ORR. Liquid may block channels, hampering reactant supply and unstable fuel cell operation.[98,103–106] Due to the important role of liquid water in the channel flow, the wettability of the GFC wall tremendously impacts the channel two-phase flow. Hydrophilic GFC walls seem to be favored by practitioners

since they facilitate the formation of a thin liquid-water film and provide a steady flow of air to reaction sites, whereas the hydrophobic GFC walls can result in unsteady PEMFC operation.

The bipolar plates (BPs) are a major contributor to the total fuel cell weight. The DOE target on the BP weight is <0.4 kg/kW by 2015 and cost target of $3/kW by 2015. Adrianowycz showed their development status in 2009 is 0.57 kg/kW.[107] Some attributes of BP material include chemical stability and high conductivity to electrons and heat. Non-porous graphite is a popular material to manufacture BPs. However, its disadvantages, such as brittleness and cost, limit the manufacturing BPs with graphite. Other alternative materials include aluminum, iron, stainless steel, titanium, nickel, polymer composites, silicon, and carbon-based materials. In addition, metallic alloys can be ideal materials for bipolar plates; merits include: low-cost, high-volume manufacturing, high thermal and electrical conductivities, and formability into thin sheets or foil. However, metals are subject to corrosion in PEMFC operating environments. Coating seems to benefit the corrosion resistance of metallic bipolar plates, however pinholes and defects can exist as well and result in local corrosion and metallic ion contamination of the membrane. Studies of pinhole free coating have been conducted.[108,109] Another approach is to improve the methods of engineering graphite plates. For instance, stamp/molding methods are promising to significantly reduce cost compared with machining graphite bipolar plates.[110]

1.1.2.5 GDL/GFC Interface. At the cathode GDL/GFC interface, oxygen transports to the electrode where it reacts with protons and electrons to produce water,

which eventually enters the channel. The interfacial resistance for reactant transport will be significantly increased due to the presence of liquid water. Liquid water exists as droplets on the GDL surface, and is either taken away by the gas flow[98,103,105,106,111,112] or attaches itself to the channel wall.[98] The behavior of liquid water droplets at the GDL/GFC interface consists of three sub-processes: transport from the catalyst layer to the GDL/GFC interface via capillary action; removal at the GDL/GFC interface via detachment or evaporation; and transport through the GFC in form of films, droplets and/or vapor. The growth and detachment of water droplets are influenced by two factors: the operating conditions of the fuel cell and the physical (e.g., surface roughness) and chemical (e.g., wettability) material characteristics of the GDL surface. Chen *et al*. pioneered the analysis of droplet instability and detachment and they indicated that the static contact angle and contact angle hysteresis are both important parameters in determining the force required to move a droplet across a surface.[113] Instability diagrams were developed to explore the operating conditions stability. Unstable conditions are desirable to operate the fuel cell under such conditions that droplets can be removed instantaneously from the GDL/GFC interface so as to prevent blockage of pathways for oxygen transport to the three-phase reaction sites. In addition, the VOF-based modeling has also been conducted to investigate the droplet dynamics at the interface.[114–118] The droplets on the GDL surface increase reactant transport resistance into the GDL as well as liquid flow inside. Given that the droplets appear randomly at the GDL surface, statistical methods might be adopted to evaluate the portion of area covered by liquid. Also the GFC–GDL interface bridges the transport in channels and GDL, therefore a

fundamental understanding of this connection and a mathematical model that can describe the connection is highly needed. A simplified explicit mode was developed to analyze water-droplet detachment in the inertia-dominating regime.[119] A realistic water-flux boundary condition at the GDL/GFC interface was also discussed. Further detailed study on more realistic droplet emerging/detachment in a real fuel cell channel, a wide range of regimes, as well as its coupling with the transport and electrochemical reaction is in high demand.

1.1.2.6 Stack. In order to obtain a higher power and voltage outputs, single cells are arranged a stack and connected in either series or parallel mode. At the stack level, water and heat management becomes more complex due to the interactions of constituent sub-cells. Electrical connection is one of the essential issues. A local high electronic resistance will significantly affect the stack performance, since the electrical current flows through each individual cell in a series stack. Another issue is the flow field. In practice, several single cells share one inlet/outlet manifold in a stack. Therefore, a fuel cell with high flow resistance receives smaller amounts of the reactants, causing local reactant starvation, which further leads to cell performance decay and material degradation as discussed before. Heat transfer connection is also important. A fuel cell exhibiting a larger thermal resistance or that is insufficiently cooled will become subject to a higher temperature and conduct heat to adjacent cells. Detailed fundamental study at the stack level becomes challenging. Promislow and Wetton developed a simplified steady-state thermal transfer stack model.[120] The model is appropriate for straight coolant channel unit cell designs and considers quantities averaged over the cross-channel

direction, ignoring the impact of the gas and coolant channel geometries. Many numerical models were developed for stacks as well.[121–129]

At the stack level, the following issues are also considered important areas requiring further study: optimization of the stack system; the fuel processing sub-system; power and electric subsystems; thermal management sub-system; and ancillary sub-system. Modeling and simulation of PEM fuel cell stacks provide a powerful tool for stack design and optimization. Comprehensive models are still under development.

1.2 Water Management

1.2.1 General Issues

As shown in Fig 1.1, a single PEM fuel cell consists of a membrane electrode assembly (MEA), two gas diffusion layers, two graphite flow field plates machined with flow channels and two current collectors. The MEA consists of two Pt electrodes and a proton exchange membrane. At the anodic membrane-electrode interface, hydrogen is oxidized electrochemically into protons and is transported to the cathode where the protons combine with oxygen and yield water as a product. The product water is transported along the gas channels. In addition, water molecules are usually clustered around protons, therefore resulting in electro-osmotic drag. The voltage drop through the fuel cell can draw the proton/water cluster from one side to the other through the membrane. Proton migration associated with water molecule transport normally happens in the direction from anode to cathode.[130–132] As a result, water is accumulated at the

cathode. The water concentration gradient between the anode and cathode causes water back diffusion from cathode to anode, which prevents the dehydration of the membrane from the anode. The gradient between anodic and cathodic water concentration is determined by the thickness of the membrane, its water content and humidity of the reactant gases. The latter in turn is dependent on the gas inlet humidification and on the temperature and pressure in the gas channels [133]. Sridhar *et al*. claimed that at low current densities back diffusion prevails on electro-osmotic drag, while at high current densities electro-osmotic drag prevails over back diffusion. Thus the anode will tend to dry out, even if the cathode is well hydrated.

Water in the membrane could benefit proton transport in the ionomer, because protons move through ionomer via dissociation of sulfonic acid bonds.[134] Under dry condition, proton migration tremendously decreases due to the rigid sulfonic acid bonds, which leads to the decrease of ionic conductivity as well. Low ionic conductivity also decreases the proton accessibility to the catalyst active sites on Pt, which slow down the kinetics of activation polarization.[135] Furthermore, under extremely dry conditions, membrane degradation such as delamination and pinholes, etc. start to occur within 100 sec, which is claimed to be irreversible.[136,137] Such degradation causes some gaps in between the membrane and the electrodes, which increases the ohmic loss in the fuel cell. On the contrary, a fully hydrated membrane can achieve ca. 300 times higher conductivity than a dehydrated membrane.[138] Hence, maintaining a high membrane hydration level is crucial to improve the ionic conductivity. However, excess water can accumulate and block the flow channels and catalyst active sites and cause cathode

flooding, which could limit the cell performance. Liquid water can flood both electrodes, but flooding at the cathode is especially critical, where water can also be produced due to the oxygen reduction reaction.[139–141] The liquid water in the flow-field, electrodes and gas diffusion layers (GDL) must be removed. Generally, flooding of an electrode happens at high current density operation where more water is produced than the amount of water removed. Cathode flooding effects strongly depend on the operating conditions, especially at low flow rates and temperature.[142]

Cold start is another challenge for the PEMFCs. Under freezing conditions, the water management in fuel cell needs more attention. Water can freeze and destroy the fuel cell membrane and other parts, but can also serve as a lubricant under cold weather. Similarly, excess water can flood the cell while insufficient water can lower the proton conductivity, with both conditions lowering the cell performance.[143]

Fuel cell stack operation and scale up of the active area on each single cell bring on even more issues. Operating series-connected single cells creates issues along the stack axis in addition to MEA in-plane problems. An even fluid distribution to all the individual cells and a homogeneous temperature distribution needs to be achieved.[144] Due to the fact that these operating parameters directly affect water management, it is an even more challenging task to maintain a proper water balance in a fuel cell stack than in a single cell alone.[145]

1.2.2 Membrane Dehydration

Dehydration of the membrane normally occurs at the anode. The three main reasons are: (1) insufficient humidification in the gas streams; (2) water formation at the cathode is unable to hydrate the membrane at higher cell operating temperatures; and (3) electro-osmotic drag takes water molecules away from the anode during discharge.[7] Increasing the discharge current density will enhance the electro-osmotic drag and will immediately drag water molecules away from the anode. In addition, anode dehydration should be more intense at the inlet of the cell because of the higher water back-diffusion to the anode at the outlet of the cell.[146] Moreover, under dehydrated conditions the membrane pores will shrink, leading to lower back-diffusion rates. During operation this effect can be aggravated by poor thermal management.[147]

The dehydration of the membrane leads to a lower conductivity and higher ionic resistance. As a result, the ohmic loss leads to a substantial overpotential and thus a temporary power loss.[147–149] Long term degradation and MEA performance was also tested at zero external humidification: after 1,200 hrs the current density dropped from 170 to 130 mA/cm^2 at a constant potential of 0.61 V.[150] But this temporary current decay can be recovered by humidification of the membrane. The recovery time depends on membrane thickness and the water diffusion coefficient.[148,149] However, dry cell operation over a long period can cause some irreversible damage to the membrane; the membranes even become brittle and cracked. The cracks in the memrbane could lead to gas crossover of H_2 and O_2, which react with each other in the cell and create abnormal hot spots [151]. Furthermore, these hot spots are highly chemically active areas and can

possibly burn through the membrane and create pinholes, which contributes to even more gas crossover. Thus, this vicious cycle of gas crossover and pinhole production is established.[152] Therefore, the drier the operating condition, the shorter the cell life.

1.2.3 Cell Flooding

Water flooding is the accumulation of excess water and can happen at both the anode and cathode sides of the membrane. Flooding leads to an instant increase in mass transport losses, particularly at the cathode. The transport rate of the reactants to the catalyst active sites is significantly reduced.[153] Excess water blocks the pores of the GDL and thus prevents the reactants from reaching the catalyst active sites, leading to gas starvation and a mass tranport overpotential. The time dependent oscillation of cell potential at fixed current density is shown in Fig 1.6.[154] When the operating conditions allow the liquid water to accumulate to some extent and severe flooding occurs, the gas flow path can be temporarily blocked, giving rise to a sharp reduction in current density; then the blocking of the gas flow path can result in a sudden build-up of local pressure that quickly flushes out the excess liquid water, thereby resulting in a quick restoration of the current density. The periodic build-up and removal of liquid water in the cell causes the observed fluctuation in the cell performance, causing unstable, unreliable and inconsistent cell performance.[154]

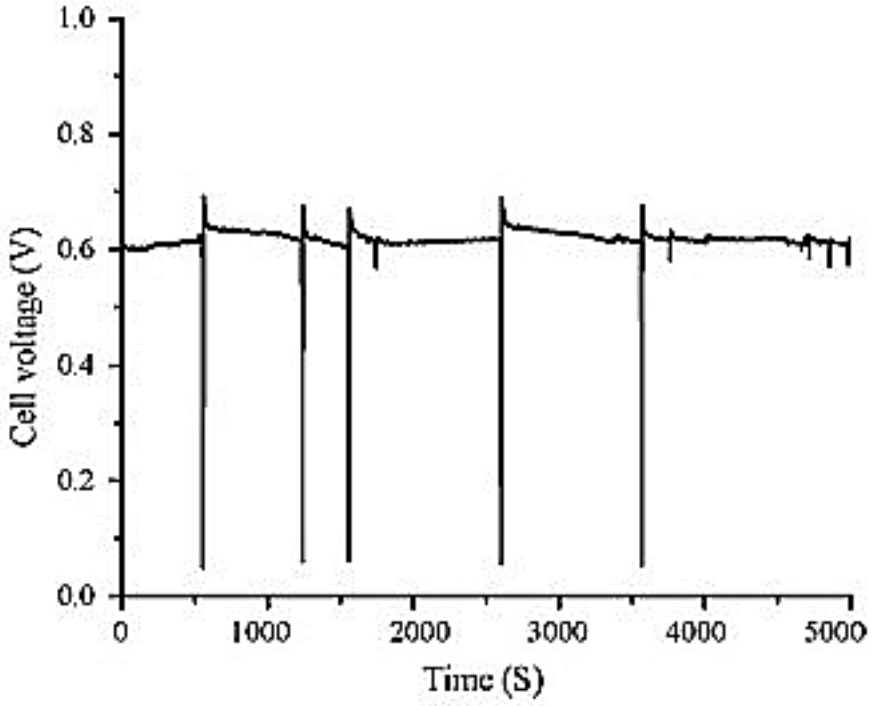


Figure 1.6 Water Flooding Pattern in a PEM Fuel Cell. Several spikes in the figure representing the tremendous voltage loss due to the cathode flooding.

1.2.4 Cathode Flooding

Generally, flooding is prone to occur at the cathode, owing to the following three mechanisms: (1) Water formation from the ORR increases with increasing current density. (2) Electro-osmotic drag pulls water molecules along with the protons from the anode to the cathode. The rate of transported water depends on the hydration level of the membrane, which increases with increasing current density as well.[147] (3) Over-humidified reactant gases and liquid water injection also lead to flooding. The water accumulated in the cathode is usually removed out of the porous electrode via evaporation, water–vapor diffusion and capillary transport through the GDL into the flow channels or by the water back-diffusion through membrane to the anode. However, study shows that back diffusion does not occur easily, unless the current density is lower than 0.3 A/cm^2.[147] Cathode flooding is more prone to occur at higher current densities accompanied by the fact that electro-osmotic drag is beyond back diffusion, resulting in higher water content at the cathode, thus further aggravating the flooding effect.[155] Water evaporation and water vapor diffusion usually occur at relatively high operational temperatures and flow rates, where the surface tension and water viscosity decrease and benefit water drainage.[153]

Once the accumulated water cannot be efficiently removed out of cathode, water flooding will negatively affect fuel cell performance, as shown in Fig 1.7. For example, at higher current densities (above 0.55 A/cm^{-2}) the partial gas pressure drop at the cathode due to flooding increases significantly, which results in a considerable cell voltage drop.

Furthermore, if the cathode pressure drop doubles from 1.5 kPa to around 3 kPa, the initial cell voltage of 0.9 V decreases to about one third of its initial value.[153]

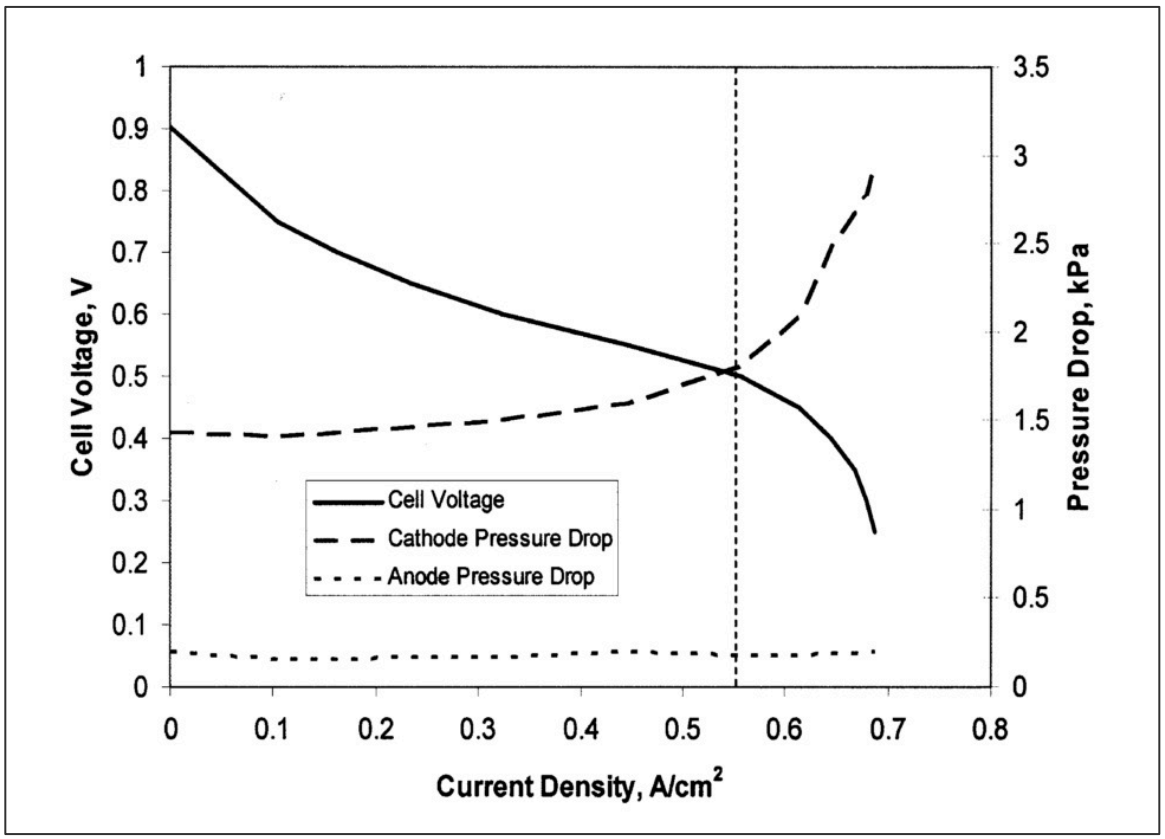


Figure 1.7 Effect of Cathode Flooding on a PEM Fuel Cell Performance

Previous modeling studies show that cathode flooding can also hinder the oxygen access to the Pt surface,[85,156,157] which leads to oxygen starvation at the cathode.[158] Presumably under steady state the net mass flow rate of oxygen into the system is equal to the oxygen consumed by the electrochemical reaction. However, in transient condition a sudden increase in power requirement from the fuel cell, oxidant supply to the system could lag behind the demand and lead to local oxygen starvation thus increasing oxygen concentration overpotential at the cathode. With depleting oxygen, the proton reduction reaction (water electrolysis) can also happen at the cathode instead of the oxygen reduction reaction.

In the case of oxygen starvation, the original electron consuming process ORR (2) would be replaced by the new electron consuming process (3):

$$O_2 + 4H^+ + 4e^- = 2H_2O \qquad E_0 = 1.23V \tag{2}$$

$$2H_3O^+ + 2e^- = H_2 + 2H_2 \qquad E_0 = 0.00V \tag{3}$$

In this case, the cathode potential would drop from 1.23 V to 0.00 V at current off and probably from 0.8 V to –0.1 V at current on with this reaction substitution. Electrode polarization occurs with current flowing through the electrode. The cathode polarization causes a potential shift toward negative direction and the anode polarization toward positive direction. For the hydrogen oxidation reaction (HOR) taking place at the anode:

$$H_2 - 2e^- = 2H^+ \ (E_0 = 0.00V) \tag{4}$$

With current flowing, the electrode potential will shift toward the positive direction (e.g. 0.1 V). Thus, the cell voltage will change from the original 0.7 V (0.8 to 0.1V) to –0.2 V (–0.1 to 0.1V) as shown in Fig 1.8. The output voltage of the cell, which is under oxygen starvation, will likely be reversed from a positive value, for instance 0.7 V, to a negative value, for instance –0.2V, with substitution of PRR for the ORR. This phenomenon is known as the voltage reversal effect (VRE) in a PEMFC.[159,160] In a stack of PEMFCs, when VRE happens in a single cell not only does it not contribute to the performance output of the whole stack, but also can counteract partial effective output voltage from other single cells. Therefore, as long as the VRE appears, the output of the stack will be seriously impaired.

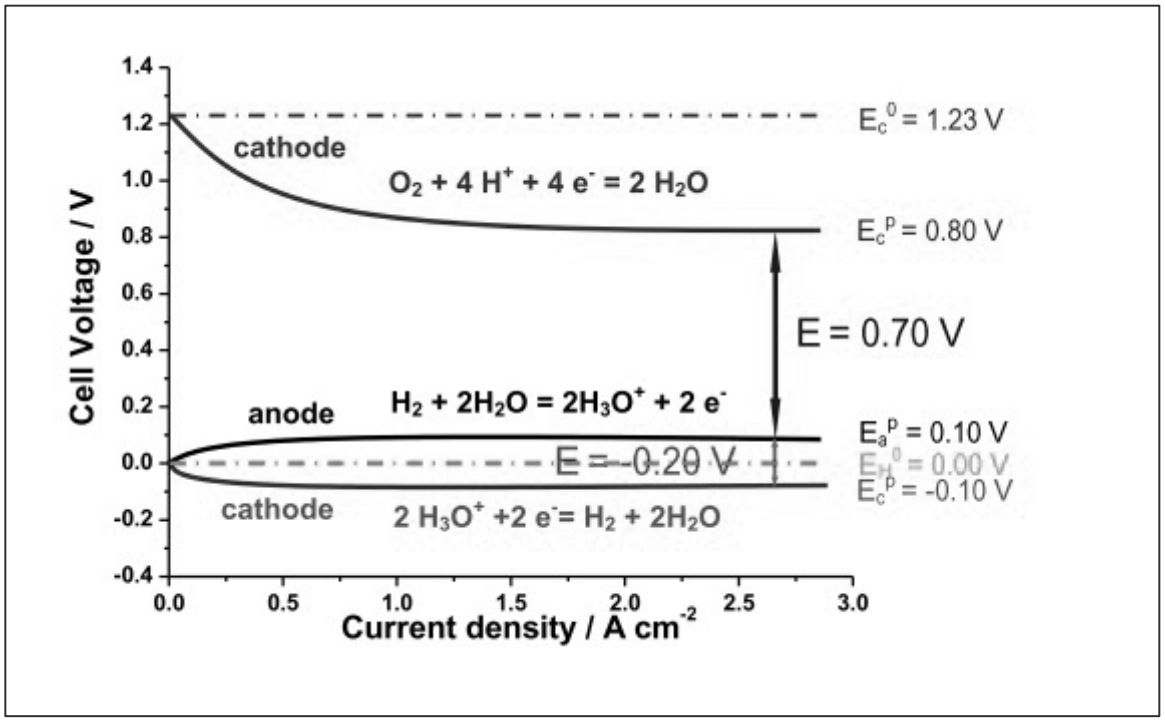


Figure 1.8 Voltage Reversal Effect in a PEM Fuel Cell.

1.2.5 Anode Flooding

Anode flooding can also happen at low hydrogen flow rates, leading to hydrogen starvation, carbon substrate oxidation and oxygen evolution. The following are the conditions which can cause anode flooding: (1) Wang *et al*. claimed that anode flooding is often observed at low current densities ($0.2A/cm^2$), especially at low flow rates and temperatures.[142,161] (2) Anode flooding can also be caused by water back-diffusion from the cathode together with a low hydration state of the fuel gas stream. At low current density, if the relative humidity is not as high as at the cathode, water back-diffusion through the GDL to the anode will surpass the electro-osmotic drag effect leading to the increase of water content at anode, especially at the flow channel exit.[147] (3) Liquid water injection for cooling and humidification together with moderate cell temperatures can lead to the anode flooding as well.

1.2.6 Flow Channel Flooding

Noted that flooding occurs not only in the GDL, it occurs in the flow channels as well. Flow channel flooding is highly influenced by the machining of the BPs and operating conditions. Flow channel flooding can hinder the fuel access to the porous electrodes and impair the power output of the fuel cell. Flooding of one flow channel can lead to a multiple parallel channel starvation region growing. As a result, the power and voltage output decreases in an operating PEM fuel cell, and changes the cell characteristics: locally low current density, locally elevated temperature from water condensation, and pressure drop within the PEM fuel cell.[141,153,154]

1.3 Proton Exchange Membranes

As mentioned above, the general membrane is the core component of the PEM fuel cell. The polymeric membrane in the PEM fuel cells plays three main roles as follows: it is a charge carrier for protons, separates the reactant gases, and acts as an electronic insulator to prevent passing of electrons through the membrane. Since DuPont developed Nafion® in 1970s, this type of perfluorosulfonic acid (PFSA) soon became a standard for the PEMFC and remains so still today. The Dow Chemical Company and Asahi Chemical Company synthesized advanced PFSA membranes with shorter side chains and a higher ratio of SO_3H to CF_2 groups.[162]

Nafion® has a structure of copolymer from fluor 3,6-dioxo 4,6-octane sulfonic acid with polytetra-fluorethylene (PTFE). The Teflon® backbone of this structure gives the hydrophobic nature for the membrane; and the hydrophilic sulfonic acid groups (HSO_3^-) have been grafted chemically into the backbone. These ionic groups cause the absorption of the large amount of water by the polymer and therefore lead to the hydration of polymer. Thus, the factors affecting the performance of a proton exchange membrane are the level of hydration and thickness of the membrane, which play important roles in deciding the membrane's suitability for application in a fuel cell.[163] The proton exchange membrane performance is related to the extent of its proton conductivity and the proton conductivity is also related to the extent of the humidity of the membrane. Higher hydration condition leads to higher proton conductivity. One of the ways to avoid water drag or water crossover is to reduce the membrane thickness thereby enabling an improvement in fuel cell performance. Other advantages of reduced

thickness include lower membrane resistance, lower cost and rapid hydration. However, there is a limit to the extent to which membrane thickness can be reduced because of difficulties with durability and fuel by-pass. To achieve high efficiency in fuel cell applications, the polymer electrolyte as a membrane must possess the following desirable properties: high proton conductivity to support high currents with minimal resistive losses, zero electronic conductivity, adequate mechanical strength and stability, chemical and electrochemical stability under operating conditions, moisture control in the stack, extremely low fuel or oxygen by-pass to maximize columbic efficiency, and production costs compatible with the intended applications.[12]

1.3.1 Proton Conducting Mechanisms

Proton conduction is fundamental for proton exchange membrane fuel cells and is usually the first characteristic considered when evaluating membranes for potential fuel cell use. Resistive loss is proportional to the ionic resistance of the membrane and high conductivity is essential for the required performance especially at high current density. At a molecular level, the proton transport in hydrated polymeric matrices is in general described on the basis of either of the two principal mechanisms: (1) “proton hopping” or “Grotthus mechanism” and “diffusion mechanism” or “vehicular mechanism”.[164–166]

In the proton hopping mechanism protons hop from one hydrolyzed ionic site (SO_3^- H_3O^+) to another across the membrane. In this mechanism, ionic clusters were swelled in the presence of water and formed the percolation mechanism for proton transferring. The simple scheme of the hopping mechanism has been shown in Fig 1.9.

The hopping mechanism has little contribution to conductivity of perfluorinated sulfonic acid membranes such as Nafion®. The second mechanism is a vehicular mechanism. In this mechanism hydrated proton (H_3O^+) diffuses through the aqueous medium in response to the electrochemical difference. In vehicular mechanism, the water connected protons ($H^+(H_2O)_x$) carry the one or more molecules of water through the membrane and itself are transferred with them. The major function of the formation of the vehicular mechanism is the existence of the free volumes within polymeric chains in the proton exchange membrane, which allow the transferring of the hydrated protons through the membrane. The schematic design of the vehicular mechanism in proton conduction in pristine and nano-composite membranes has been shown in Fig 1.10 (a, b). Water also has two suggested transport mechanisms: electro-osmotic drag and concentration gradient driven diffusion (this probably occurs as self-associated clusters: $(H_2O)_y$). The hydrophobic nature of the Teflon® backbone facilitates the water transfer through the membrane because the surfaces of the hydrophobic holes tend to repel the water molecules.[167]

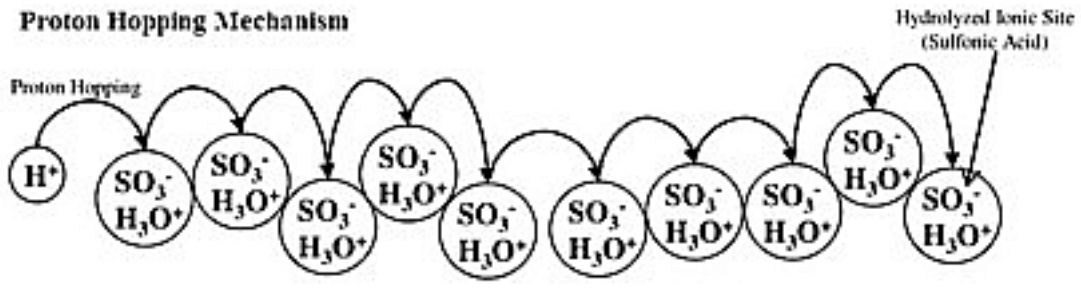


Figure 1.9 Water Transport in Membrane Through Hopping Mechanism[167]

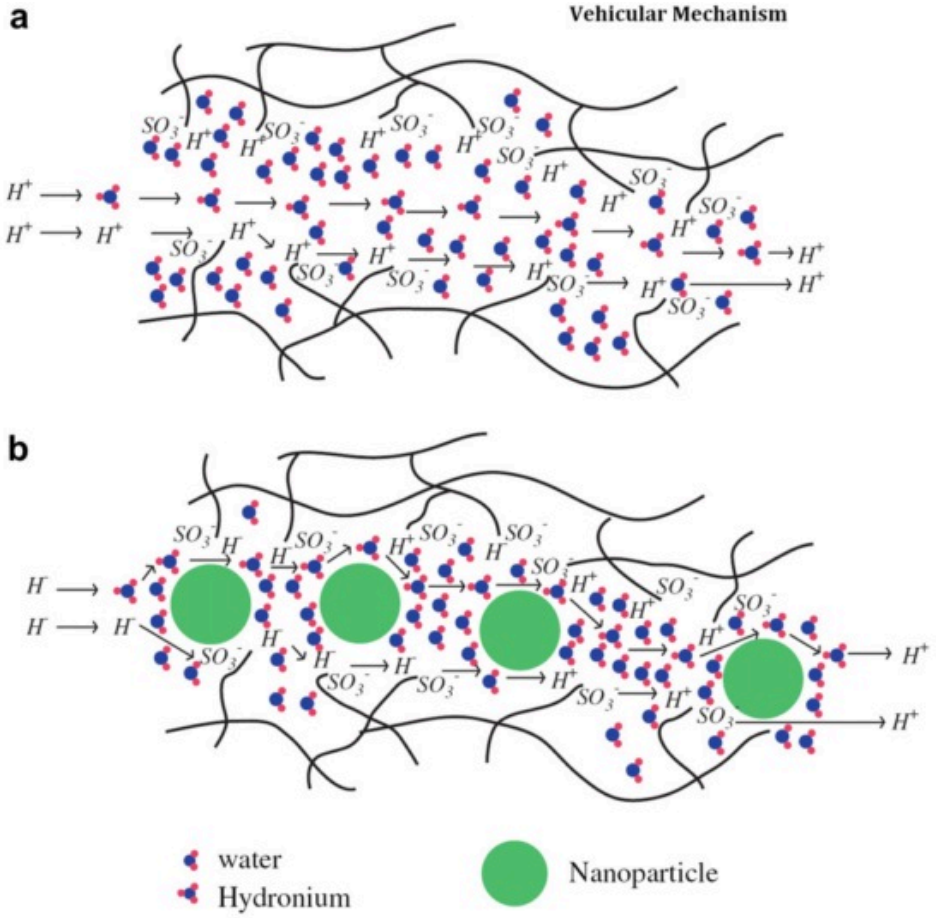


Figure 1.10 Water Transport in Membrane Through Vehicular Mechanism[165,168]

The prevalence of one or the other mechanism depends on the hydration level of the membrane. On the other hand, the mechanism of proton transport within nano-composite and hybrid systems based on the aforementioned membranes is a much more complex process as it involves both the surface and chemical properties of the inorganic and organic phases. Although the exact role of inorganic components in stabilizing the proton transport properties of nano-composites based on Nafion® and other polymers is still under discussion, it may be presumed that the primary function of the nano-particles is to stabilize the polymer morphology with increasing temperature. If the inorganic additive happens to be an alternative proton transporter like heteropolyacids, their contribution to the transport processes also has to be analyzed. Proton conductivity improvements would, however, depend upon whether the fraction of bulk water and the bulk proton concentrations are increased as a result of the inorganic additives or not.

1.3.2 Proton Exchange Membranes Synthesis

1.3.2.1 Perfluorinated Ionomeric Membranes. The Perfluorinated polymers due to the small size and the high electronegativity of the fluorine atom have a strong C-F bond and a low polarizability. These polymers due to their thermostability, chemical inertness and the enhanced acidity of sulfonic acid group in $-CF_2SO_3H$, have been utilized in chlor-alkali process and as proton exchange membranes for fuel cell applications.[169] These membranes are prepared by the polymerization of monomers, which contain a moiety that can be made either cationic or anionic by further treatment; and these are high equivalent weight (EW) perfluorinated membranes and have limited

their use in fuel cells because they consume high power density.[170] Similar polymers are Flemion® produced by Asahi Glass and Aciplex-S® produced by Asahi Chemical.

1.3.2.2 Non-fluorinated Hydrocarbon Membranes. The other type of materials used in proton exchange membrane synthesis, are non-fluorinated hydrocarbon polymers which can be aliphatic or aromatic polymers having benzene ring structures in the polymeric backbone of membrane or in the bulky pendant groups from this membrane polymeric backbone. Presently, one of the most promising routes to high-performance proton conducting polymer electrolyte membranes is the use of hydrocarbon polymers for polymer backbones.[171] Hydrocarbon membranes provide some definite advantages over perfluorinated membranes. They are less expensive, commercially available and their structure permits the introduction of polar sites as pendant groups.[12] Hydrocarbon polymers containing polar groups have high water uptakes over a wide temperature range, and the absorbed water is restricted to the polar groups of polymer chains. Decomposition of hydrocarbon polymers can be depressed to some extent by proper molecular design. Hydrocarbon polymers are easily recycled by conventional methods.

In order to enhance stability at elevated temperatures, aromatic hydrocarbons can be (a) incorporated directly into the backbone of a hydrocarbon polymer or (b) polymers modified with bulky groups in the backbone to render them suitable for conduction of protons.[12,172] Polyaromatic membranes are high temperature rigid polymers with Tg > 200 °C owing to the presence of inflexible and bulky aromatic groups.[173] The aromatic rings offer the possibility of electrophilic as well as nucleophilic substitution. Polyether sulfones (PESF),[174–176] polyether ketones (PEK) with varying number of ether and ketone

functionalities, poly(arylene ethers), polyesters and polyimides (PI) are some of the relevant examples of main chain polyaromatics.[177] Poly(2,6-dimethyl-1,4-phenylene oxide) (PPO) can meet most of the requirements for application in PEMFCs because it is a hydrophobic polymer with high glass transition temperature (Tg = 210 °C), high mechanical strength, and excellent hydrolytic stability. Although the structure of PPO is simple as compared to other aromatic polymers, it allows many modifications in both aryl and benzyl positions: (1) electrophilic substitution on the benzene ring, (2) radical substitution of the hydrogen from the methyl groups, (3) nucleophilic substitution of the bromomethylated PPO, (4) capping and coupling of the terminal hydroxyl groups in PPO chains, and (5) metalation of PPO with organometallic compounds.[178] Polyaromatics are often preferred for fuel cell application due to their thermal stability. Also, the polyaromatics from oxidant point of view are stable in the acidic medium.

1.3.2.3 Acid–base Complexes. Acid–base complexes have been considered as a viable alternative for membranes that can maintain high conductivity at elevated temperatures without suffering from dehydration effects. In general, the acid–base complexes considered for fuel cell membranes involve incorporation of an acid component into an alkaline polymer base to promote proton conduction.[12]

The phosphoric acid-doped polybenzimidazole (PBI/H_3PO_4) membrane seems so far the most successful system for high temperature PEMFC preferably under ambient pressure. It has in recent years motivated extensive research activities covering polymer synthesis, membrane casting, physicochemical characterizations and fuel cell technologies. Acid-doped PBI membranes have been extensively characterized. Related

fuel cell technologies have been developed and high temperature PEMFC has been successfully demonstrated at temperatures of up to 200 °C under ambient pressure. No gas humidification is mandatory, which enables the elimination of the complicated humidification system, compared with Nafion® cells. Other operating features of the PBI cell include easy control of air flow rate and cell temperature.[14]

1.3.3 Modification of Proton Exchange Membranes

Recently, the modification of the fluorinated membranes such as Nafion® and non-fluorinated membranes such as sulfonated polyether ether ketones, sulfonated polyether sulfones, sulfonated polyether imides and other types of proton exchange membranes have been studied and investigated in fuel cell applications. It is clear that Nafion® and related polymers are still being intensely examined in view of the complex cell requirements of high proton conductivity and outstanding chemical stability combined with longevity of 60,000 h at 80 °C. The major disadvantages of these perfluorosulfonic acid (PFSA) materials are: the high cost of membrane amounting to US$ 700 per square meter,[179] requirement of supporting equipment,[180,181] and temperature related limitations. Degradation of PFSA membrane properties at elevated temperatures is another serious drawback. Conductivity at higher temperatures (up to 100 °C) is reduced than lower temperatures.[171] Also, the phenomena related to membrane dehydration, reduction of ionic conductivity, decreased affinity for water, loss of mechanical strength due to softening of polymer backbone and increased parasitic losses through high fuel permeation are observed at temperatures above 80 °C. With regard to

the application in direct methanol fuel cells (DMFC), Nafion® exhibits a high methanol permeability greater 80,000 Barrers at 80 °C, which drastically reduces the DMFC performance and renders it unsuitable for DMFCs.[182] Efforts are directed to eliminate the disadvantages such as crossover problems and loss of hydration above 100 °C. However, it is likely that Nafion® will be replaced by an alternative membrane in the future.[183] In order to overcome few of the disadvantages of the PFSA membranes enumerated above, the authors are also carrying out research work to identify promising alternatives.[184,185]

Basically, there are two ways to enhance the properties of proton exchange membrane: polymeric blend membranes and polymer/inorganic composite membranes. The latter is easier to fabricate. This type of composite can be configured in a number of ways:

- Both polymer and inorganic components can be ionically conductive;
- Ionic polymer with inorganic filler for mechanical support;
- Ionic polymer with water-retaining inorganic filler;
- Ionically conductive inorganic additive with supporting polymer.[186]

This partial list only covers a few of the possible combinations. Polymer inorganic composite membranes are interesting because many of the inorganic additives used are able to operate at much higher temperatures than the pure polymers. Some of the possible advantages of incorporating inorganic compounds into composite membranes include, enhanced proton conductivity, water retention at high temperatures, and mechanical support. Rikukawa and Sanui[171] suggest that in order to produce materials that are less expensive than Nafion®, some sacrifice in material life-time and mechanical

properties may be acceptable, provided the cost factors are commercially realistic. Hence the use of hydrocarbon polymers, even though they had been previously abandoned due to low thermal and chemical stability, has attracted renewed interest. Therefore, the efforts to develop these higher temperature membranes include modification of the conventional host polymers. The most important goals of modification of the proton exchange membranes in PEM fuel cells can be mentioned such as preparation of the proton exchange membranes with lower cost compared to the fluorinated membranes, the desirable water uptake and retain in the elevated temperatures, desirable proton conductivity in the higher temperatures, the lower extent of the reactant gaseous and methanol crossover through the membrane, improved thermal stability, higher mechanical and chemical strength and also creation of the self-humidity of the membranes in elevated temperatures.

As mentioned in above, Nafion®, the conventional proton conducting polymer electrolyte membrane is expensive, mechanically unstable at temperatures above 100 °C, and conductive only when soaked in water, which limits fuel cell operating temperatures to 80 °C, which in turn results in lower fuel cell performance due to slower electrode kinetics and low CO tolerance.[132] Thus, the development of membranes, which are mechanically and chemically stable at higher temperatures (above 100 °C) is an active area of research for producing economical fuel cells. A wide range of the fillers such as SiO_2, zirconium phosphate, phosphotungestic acid,[187,188] molibdophosphoric acid, suspending SiO_2, organically modified silicates, silane based fillers and zeolites are used for the preparation of the Nafion®-based composite proton exchange membranes.

Composite membranes are shown the promising characteristics such as lower H_2, O_2 and methanol crossover, good thermal stability, increased proton conductivity, and higher water uptake. In the following sections, the types of the modified proton exchange membranes in the PEM fuel cells are investigated.

1.4 Hydrogen Bromine Redox Flow Battery

1.4.1 Introduction

Nowadays, the needs for electricity have been increased dramatically. Because of the energy crisis and the needs of environmental friendly, solar and wind energy are receiving more and more attention. But there are certain disadvantages of this type of energy, for example, solar energy is only able to generate electricity during daylight hours, which means for around half of each day, solar panels are not producing energy for your home. Also, the weather can affect the efficiency of solar cells too. This situation is not just an issue for the US. Many developing countries such as China, India, and Mexico are constantly requiring a large amount of electricity energy for industrial production too. Some certain areas, such as Mexico have abundant wind and solar energy sources, but unlike the US, they do not have a well-established electricity grid system. So the electricity that generated from wind or solar power cannot be transferred from one site to another site. The need for energy storage for these intermitted power supply is very urgent. Batteries for large-scale gird storage require durability for large numbers of charge/discharge cycles as well as calendar life, high round trip efficiency, an

ability to respond rapidly to changes in load or input, and reasonable capital costs.[189] The hydrogen bromine redox flow battery is considered as one of the good candidates, which is suitable for large-scale electricity grid energy storage. On one hand, like all the other the chemical reactants that provide their energy are stored in external tanks, so it can provide more energy just by increasing its storage capacity of the external tanks. On the other hand, the system includes the fast kinetics of the hydrogen and bromine electrode, which leads to a high electric-electric efficiency.

The hydrogen bromine redox flow battery is also called hydrogen bromine fuel cell, because of its similarity with a polymer electrolyte fuel cell (PEFC). Our research started with an elementary study of a PEFC. Fuel cells and flow batteries are both electrochemical devices that directly convert chemical to electrical energy. During operation, the PEFC is typically fed with hydrogen at the anode and oxygen at the cathode. The protons produced by the hydrogen oxidation reaction are conducted to the cathode through the electrolyte membrane, and the electrons released at the anode travel along the external circuit to the cathode and generate the electrical current.

A key component in PEFCs is the polymer electrolyte (i.e. proton exchange membrane), which is the same type of membrane used in a hydrogen bromine redox flow battery. Basic requirements for the membrane are that it has high proton conductivity to minimize the cell resistance and is electrically insulating to prevent shorting. In addition, these membranes work as a reactant gas barrier and must have good mechanical properties and chemical stability to maximize the lifetime of the system.

Here, we demonstrate several methods to investigate the proton exchange membrane properties. Density measurements using gas pycnometers (Accupyc 1340, Micromeritics) and partial molar volume calculations have been demonstrated to study the structure as well as some thermodynamics properties of the membrane. Acid/water uptake experiments have been done by titration using DL15 Titrator (Mettler Toledo), and some transport properties were studied. To further investigate the performance of hydrogen bromine redox flow batteries, we systematically studied the influence of temperature, acid concentration, catalyst layer and different ion exchange membranes on battery performance. The membranes in use include Nafion®, and 3Mion PFSA with different thickness and equivalent weight, etc. This research mainly focuses on membrane fundamental study and characterization, as well as studies of the effects of HBr uptake and transport into the membrane. Some cell testing and diagnostics development are also included for a hydrogen bromine redox flow battery.

The hydrogen bromine fuel cell was originally designed by NASA as a power source suitable for space applications. Recently Lawrence Berkeley National Lab (LBNL) has been designing a flow battery for grid storage that relies on a hydrogen-bromine chemistry which could be more efficient, last longer and cost less than today's lead-acid batteries. This battery could also be used on earth for large-scale energy storage in load-leveling applications.[190–193] The advantages of this type of aqueous system include inexpensive electrolyte with high ionic conductivities, fast kinetics on the electrodes, and ability of scaling up to grid storage etc. Hydrogen bromine redox flow batteries can also be operated with shallow discharges and can tolerate both overcharge

and over-discharge.[194] If the electrolyte is mainly absorbed in the separators, and the quantity of electrolyte suitably adapted, aqueous electrolyte batteries may be operated in a sealed, maintenance-free condition.[195]

The typical structure for a halogen redox flow battery is shown in Fig 1.11.[196] And the reaction of hydrogen bromine redox flow battery is shown as following equations (5) and (6):

$$Br_2\ (aq) + 2e^- = 2Br^- \qquad E^0 = 1.0873 \qquad (5)$$

$$H_2 = 2H^+ + 2e^- \qquad E^0 = 0V \qquad (6)$$

But, in the presence of bromide bromine forms the tribromide ion (Br_3^-). The species are in equilibrium according to Eq. (7):

$$Br_3^-(aq) + 2e^- = 3Br^- \qquad E^0 = 1.062V \qquad (7)$$

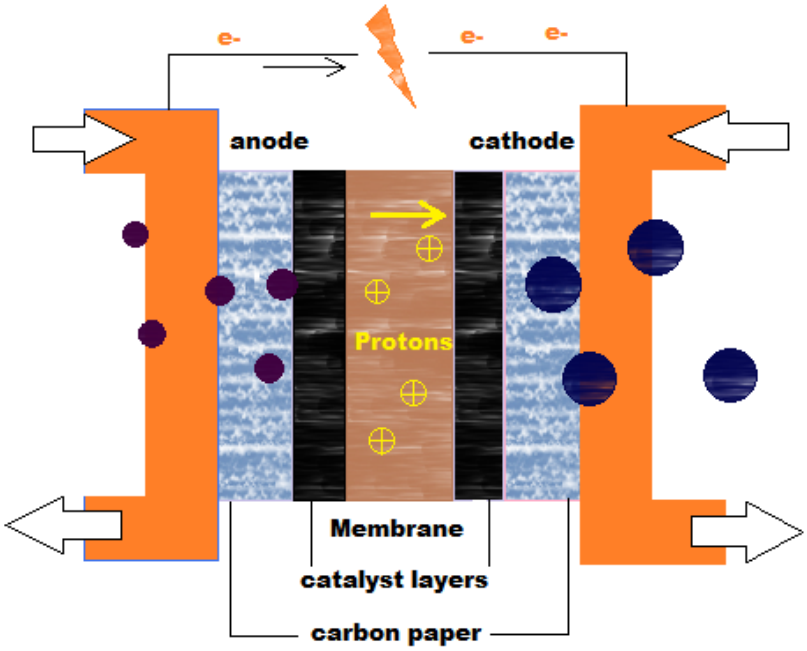


Figure 1.11 A Schematic of a Redox Flow Battery

Thus, a potential difference is always observed, as the solution is Br_3^- and Br_2 mixed. Because of the crossover issue of hydrogen bromine redox flow batteries, some of the research focuses on membrane composition and other methods to reduce the bromine or bromide crossover. By using a diffusion cell, chronoamperometry is applied to measure the transient current when bromine is added into the solution.

1.4.2 Transport Phenomena

The water uptake and transport properties in Nafion®117 have been studied by Zawodzinski *et al*. at room temperature and 30 °C.[131] Diffusion coefficient and relaxation time of water in the membrane and the proton conductivity of the membrane as functions of membrane water content were measured. The ratio of water molecules carried across the membrane per proton transported, the electro-osmotic drag coefficient, also was determined for a limited number of membrane water contents. This work has been considered as the basic theory for my water/acid uptake experiment, and partial molar volume of the membranes were calculated based on the water uptake work. As for Br_2 transport in membrane, a dialysis cell was adapted by A Heintz, C Illenberger *et al*.[197] According to their model, a high concentration of Br^- can diminish the effective concentration of neutral Br_2 molecules.

1.4.3 Bromine Crossover and Poisoning Effect

One of the disadvantages of hydrogen bromine flow battery is that the effect of bromine crossover can poison the platinum on the anode and prevent the effective

hydrogen reaction. A study has been done by M. Goor-Dar *et al*.[198] about hydrogen redox reactions on platinum nanoparticles in different concentrations of HBr and Br_2. Cyclic voltammetry shows that high concentration of hydrobromic acid can affect the hydrogen redox reaction. From RDE study of the platinum electrode, they found that at low concentrations of HBr solution (up to 1mM) the bromide adsorption is reversible, as shown in Fig 1.12. But at high concentrations of HBr (3M), only some of the bromide can be desorbed by scanning the potential to more negative values (-30mV).

To reduce the effect of bromine/bromide poisoning effect, complexation of bromine is studied by Daniel J. Eustace.[199] Four different sulphonic acid based membranes, Nafion®, sulphonated polystyrene (S-PS), sulphonated polystyrene irradiation grafted onto perfluoroalkoxyl co-polymer (PFA-g-S-PS), sulphonated polystyrene chemically grafted onto polytetrafluoroethylene (PTFE-g-S-PS) and polystyrene (PS) are tested by FTIR. Results showing that sulphonate type membranes, where the sulphonate functional group is attached to the polymer backbone via a phenyl group, are susceptible to chemical attack in bromine environments. The effects of temperature and the ratio of bromine to bromide concentrations are also important, as they determine the activity of free bromine, both increasing the degradation rates significantly.

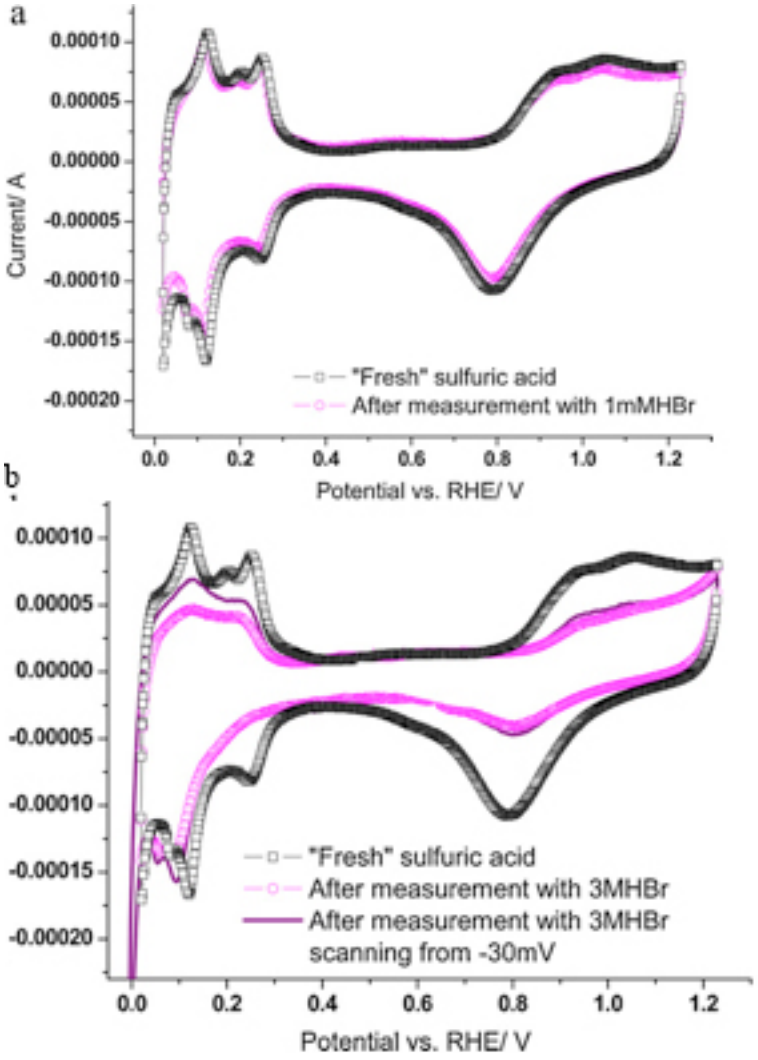


Figure 1.12 Cyclic Voltammetry of Bromine Contaminated Electrode.Voltammograms for 50% carbon-supported Pt with platinum loading of 9μg (Pt) in 0.5 M H_2SO_4 with 20 mV s−1 scan rate and 900 rpm electrode-rotation rate. (a) After measurement with 1 mM HBr and (b) after measurement with 3 M HBr.

1.4.4 Redox Reaction and Kinetics of the Flow Battery

The kinetics study of the redox reaction is the most fundamental and important electrochemistry study of the system. The general equation of the redox reaction is shown as below:

$$O+ne^- = R \tag{8}$$

Where, O is the oxidized state and R the reduced state of the ion. Because of the high reaction potential and oxidation state of the halide ion couples, the halides are usually used as an oxidant on the positive electrode and other elements such as hydrogen/proton, metal/metal ions are used on negative electrode.

The concentration of the reactants is a key parameter to evaluate the potential and current of the battery system. According to Nernst equation (9), the relationship between open circuit voltage and reactant concentration for a single electron reaction is:

$$E = E^0 + \frac{kT}{e}\ln\frac{[Ox]}{[\mathrm{Re}\,d]} = E^0 - \frac{RT}{F}\ln\frac{[\mathrm{Re}\,d]}{[Ox]} \tag{9}$$

Where, E^0 is the standard potential for the cell redox reaction, R is the gas constant, T is temperature, F is the Faraday constant, [Red] and [Ox] represent the concentration for different species. Thus, the concentration can affect the cell potential at different stages of the reaction. V. Livshits, A. Ulus, and E. Peled *et al.*, also

demonstrated how the temperature would affect the performance of hydrogen bromine redox flow batteries by making polarization curves at different temperature.[200]

1.4.5 Cell Design and Modeling

The cell design for halide ion redox flow battery is almost the same as other redox flow batteries. One thing that needs to be mentioned is that most halogen elements are toxic or highly volatile, thus safety is a very important factor when designing the cell structure. Also, unlike sulfuric acid, which is compatible with most plastic materials, compatibility is an issue for most halogen elements. For Br_2/HBr all the tubing has to be PTFE to ensure compatibility, and the tubing has to go through the metal endplate to avoid any metal contact with acid. Because of the crossover issue, the needs of designing new membrane or micro porous separators by composition or other methods are demanded. Electrodes are usually carbon fiber or felt and graphite flow channels are applied to the membrane.

1.4.5.1 Membrane. Stability of sulphonate type membranes in aqueous bromine/bromide environments has been studied by P. Morrissey *et al*.[199] The rate of degradation is critically dependent on the activity of free bromine. They present four types of membrane stability with the presence of different Br_2 concentrations as shown below. Those sulphonate groups that are directly bonded to the benzene rings are susceptible to rapid replacement by bromine, thus reducing the membrane performance.

Another issue for the membrane is cost. Most of the redox flow batteries are using Nafion® as the membrane, and contributes to the main cost of the cell assembly. Several

research groups are now focusing on reducing the cost of the membrane. V. Livshits, A. Ulus, E. Peled *et al*. have developed a nanoporous proton-conducting membrane (NP-PCM) of ceramic nano-powder and PVDF.[201–203] The advantage of this membrane is its lower cost, higher conductivity, and low fuel crossover. The hydraulic water permeation is 10 times more than Nafion®. Thus, there is no need of hydrogen humidification for the anode, and the water comes from the cathode side of the cell.

1.4.5.2 Electrodes. Hydrogen bromine redox flow batteries use platinum on carbon as a catalyst. An advanced hydrogen electrode has been developed by J.A. Kosek, A.B. Laconti *et al*., which consists of binary platinum alloys. It lowers the cost by reducing the platinum loading. To improve the battery performance, heat treatment of the electrodes are also implemented.[194] Results show that a non-heat-treated platinum alloy had an improved tolerance to the presence of bromide ion as compared with platinum black.

1.4.6 Polysulfide Bromine Redox Flow Battery

The biggest advantage for the polysulfide bromine (PSB) redox flow battery is the cost. The electrolytes of PSB are plentiful and easily available at very low cost. Therefore, this system is more economical for scale-up of energy storage capacity. However, an important disadvantage of PSB is the problem of cross-contamination of the half-cell electrolytes, thus needs an electrolyte management system to keep the system working efficiently with long cycle life. Although the on-going electrolyte maintenance adds to the operating costs of such a system, it is still the cheapest and most promising

energy storage technology suitable for applications from 10 to 100 MW with duration up to 12 h.[204–206] The bromine/polysulfide redox flow battery was first patented by Remick then extensively studied by Regenesys Technology.[196] To date, the bromine/polysulfide redox flow battery has already built up a commercial-size system.[204] The system reactions are shown below:

$$3Br^- = Br_3^- + 2e^-,\ E^0 = 1.09V \quad (10)$$

$$2\ S_2^{2-} = S_4^{2-} + 2e^-,\ E^0 = -0.265V \quad (11)$$

Nickel foam as an electrocatalytic negative electrode in a polysulfide/bromine battery was studied by Zhang *et al*. To improve the battery performance, polyacrylonitrile-based carbon felt were used as the positive electrode, and cobalt-coated carbon felt as the negative electrode. The results showed some better performance in sodium polysulfide bromine battery by switching the electrode materials. An energy efficiency of 82.4% was achieved.[207]

Chapter 2

Density Measurement and Partial Molar Volume Analysis of Membranes for Polymer Electrolyte Membrane Fuel Cells

2.1 Introduction

Water management is a critical topic in polymer electrolyte membrane fuel cell. The presence of water significantly affects the proton conductivity in membrane as well as causing retarding effect for gas transport in the flow channel when present in excess. Water is frequently introduced in the feed stream into the fuel cell, and water is produced at the cathode. In addition, 3M has developed a new series of perfluorinated ionomer membranes with shorter side chains. The polymer membranes described in this study are mainly Nafion® and these perfluorosulfonic acids (PFSA) with shorter side chains than standard Nafion®. The new ionomers show a higher degree of crystallinity, higher modulus, and higher T_α at a given equivalent weight. Thus, the ionomer structure enables lower equivalent weight membranes with higher conductivity and improved mechanical properties and durability under hot, dry conditions. The corresponding perfluorosulfonimide (PFIA) and ortho bis acid (OBA) were also synthesized by 3M. The structure of these membranes are shown in Fig 2.1 (a, b, c, d). Bis perfluoroimides are stronger acids than sulfonic acids and the bis-sulfonyl imides are very chemically stable and highly acidic. These membranes also exhibit better thermal and mechanical properties and higher conductivity for use in PEMFCs.

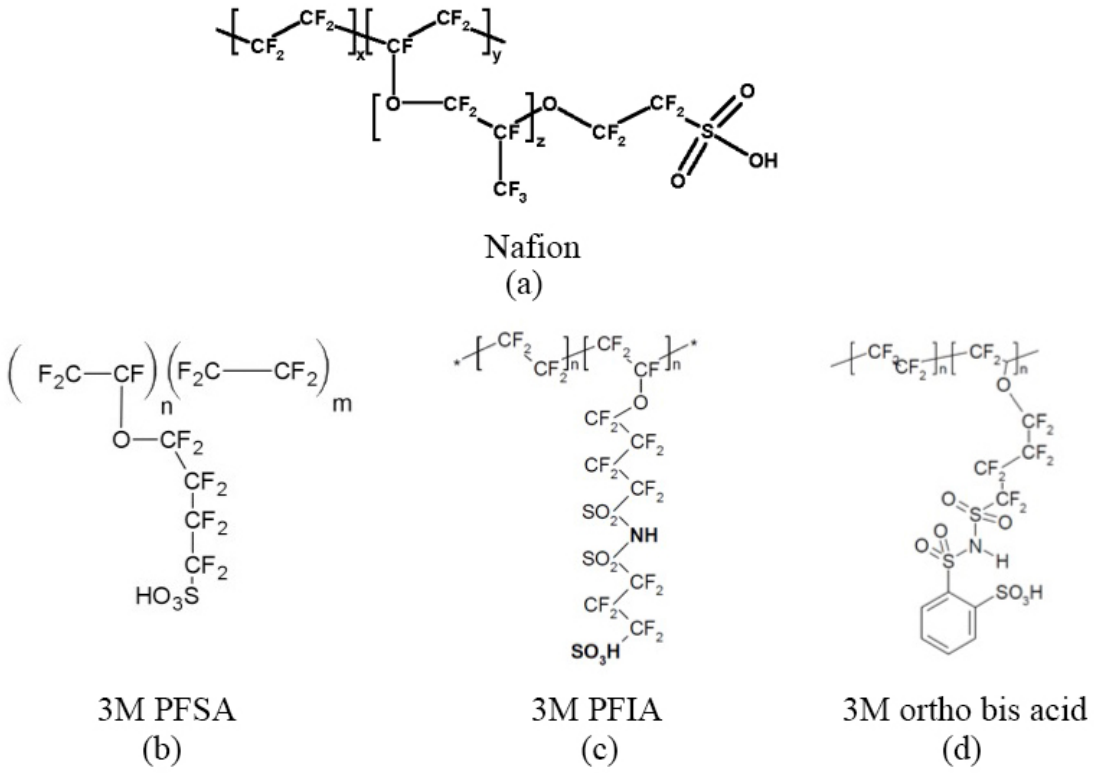


Figure 2.1 Molecular structure of Nafion and 3Mions. (a) Nafion®, (b) 3Mion perfluorosulfonic acid (PFSA), (c) 3Mion perfluorosulfonimide (PFIA), (d) 3Mion ortho bis acid (OBA)

The water content λ is considered an important parameter in evaluating membrane hydroscopic properties and is defined as the number of water molecules associated with one equivalent acid group in membrane. The water contents in different types of membranes may be different under the same hydration conditions. The membrane water uptake in vapor, even in saturated water vapor, is different from that in liquid water. Zawodzinski *et al*. reported that the water content of Nafion® varies from 2 to 15 water per acid group compared to 22 water per acid group in contact with liquid water.[131] The existence of Scroeder's paradox is discussed and experimentally affirmed by Davankov *et al*.: all polymeric networks tend to swell more strongly in any liquid than in its saturated vapor. The water contact angle is used to study the wetting properties of perfluorosulfonate acid by Zawodzinski *et al*.[208] Meanwhile the conductivity of Nafion® and water diffusion coefficient were measured under this range of water uptake. The membrane conductivity is a function of its hydration level and pore structure.[131] Experimental and modeling study by Kusoglu *et al*. shows that the proton conductivity is also depended on the cell compression, which changes the nanostructure and the morphology of the membrane.[209] Hence, the study of polymer morphology and water/membrane interaction is crucial to reveal the mechanism of proton conduction in the PEMFC.

The role of water management was discussed in Chapter 1. Here we will further discuss the swelling of membranes such as Nafion® in water. Despite the importance of the partial molar volume of the membrane, the partial molar volumes and densities of membranes at different hydration levels have not been widely measured. In this chapter, a

systematic study of densities and partial molar volumes of different membranes will be presented. We will describe the determination of some key physical properties of these materials, including water uptake by these polymers and density of the hydrated polymers, where the latter is used to analyze the partial molar volume of water and polymer segments in the membranes.

2.2. Experiment

2.2.1 Materials

Many membranes in this study were prepared by 3M and used as received. These membranes include 3M ionomer PFSAs with different equivalent weights, ortho bis acid (OBA) and perfluorosulfonimide (PFIA) membranes. The new 3M monomer for PFSA is based on electrochemical fluorination (ECF) of a hydrocarbon starting material. OBA is prepared by attaching additional protogenic groups to aromatic imides in high yield from inexpensive starting materials. PFIA is synthesized by polymerization of imide monomers with tetrafluoroethylene (TFE).

LiCl-H_2O solutions with different concentrations were prepared to control the environmental water activities. This approach is used to provide a relative humidity gradient for water uptake study.

2.2.2 Water Uptake

The membranes were pretreated by boiling in nitric acid for one hour followed by boiling in DI water for one hour. After pretreatment, membranes were dried by suspending over P_2O_5 in sealed glass vials for three days. The dry weight is measured in a sealed container on a balance. Membranes were considered completely dried when no weight change was observed in successive measurements, recorded the weight m_{dry}. The water content of a membrane was measured by suspending the completely dried membrane samples over aqueous lithium chloride solutions in sealed glass vials kept in a temperature bath at 30±1°C. After more than 5 days, equilibrium was reached where the weight of the membrane was constant, recorded the weight m_{equ}. The water uptake is calculated by equation (12).

$$\lambda = \frac{\frac{(m_{equ} - m_{dry})}{m_{dry}} \times EW}{100 \times m_{H_2O}} \tag{12}$$

Where, λ is the amount of water associated with one sulfonic site in the polymer; equivalent weights (EW) are provided by membrane suppliers; m_{dry} and m_{equ} are measured and calculated as described before

2.2.3 Gas Displacement Pycnometry

AccuPyc1340 pycnometers are used to implement gas displacement pycnometry, with helium gas. To calculate the density of membranes, we measured the exact weight

and volume of the sample. To make sure the consistency of water uptake in one sample, the samples were weighed before and after pycnometry measurement. The weight difference before and after the pycnometry measurement is less than 1%. Therefore, we assume the water uptake level is constant during this process. Samples were folded and filled into a small sample with 0.1 cm^3 capacity. The reason for using a sample cup as small as possible is to fill as much volume as possible of the sample cup to improve the accuracy of the gas displacement measurement. By pressurizing the sample compartment to two set points, we can calculate the volume of the membranes. Helium is able to fill in pores or vacancies in the polymers, which helps us to accurately measure the exact volumes of membranes with different water uptake.

2.2.4 Calorimetry

The enthalpy measurement was conducted by precision solution calorimetry using a TAM III calorimeter. The experiment was carried out by soaking membranes in water while monitoring the heat change during this process. The membranes were prepared as described before at different hydration levels and loaded into different glass sample cells. The glass cells were hit and broken in water, and the membrane sample immersed in water immediately. The enthalpy of a fully hydrated membrane was set as standard H_0 and thus each measurement represented the enthalpy change ΔH_x from that certain hydration level to fully hydrated state.

2.3 Result and Discussion

2.3.1 Water Uptake

The water uptake data has been widely used in analyzing thermodynamic interactions between water and polymers. The water uptake and transport properties of Nafion®117 at 30°C have been studied by T. Zawodzinski *et al*. The water uptakes in saturated vapor and in contact with liquid water vapor are 14 and 22, respectively. Here, we validate the data of previous research about Nafion® and measured water uptake of 3M membranes. Density measurements as a function of water content were carried out and the results were used to calculate the partial molar volume for different membranes with different water content.

Fig 2.2 shows that the water content (λ) increases with increased water activity according to a logarithmic trend. The water uptake trends of 3Mion PFSA636, 825 and 1000 show the same trend, which means the equivalent weight does not affect water content as measured by λ in same class of membrane such as 3M PFSA. This suggests that the same type of acid group has equal attraction to water molecules, independent of equivalent weight. The same trends and features are observed as for Nafion® membranes, shown in Fig 2.3.

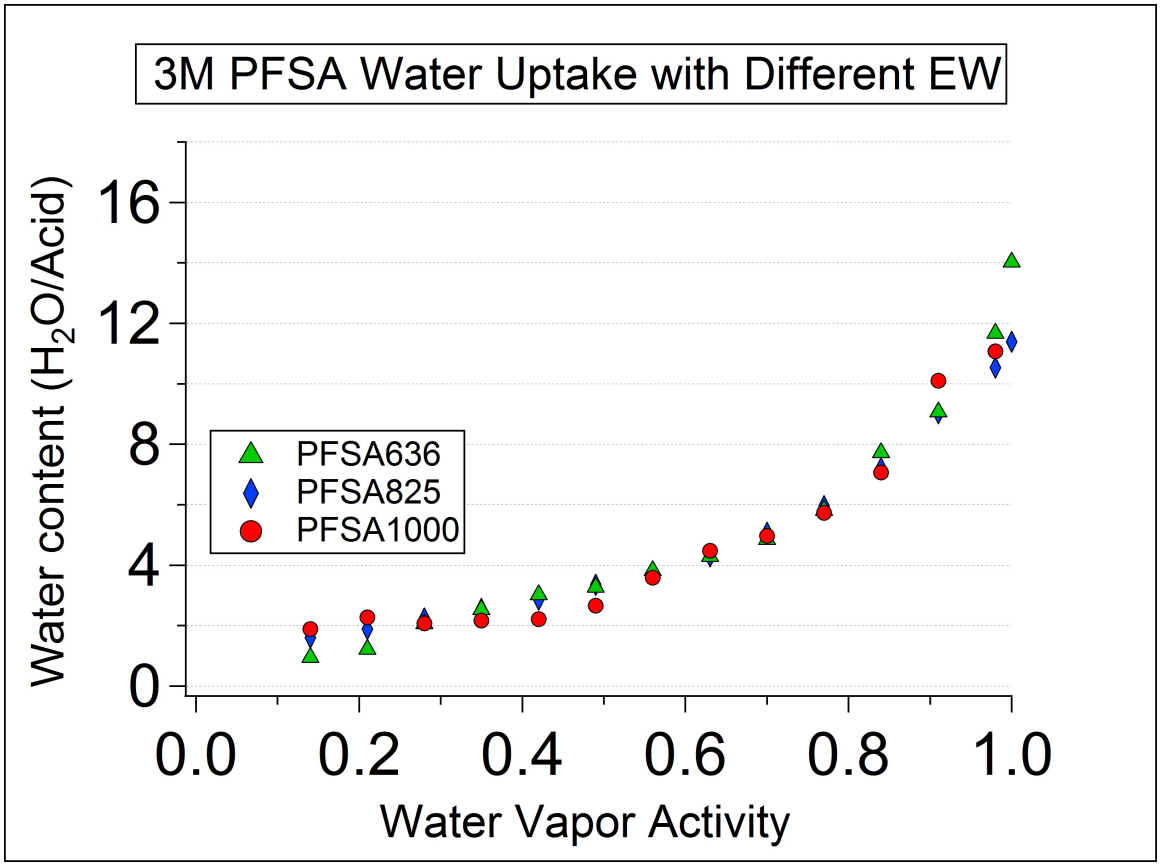


Figure 2.2 Water Content of 3M PFSA (EW636, 825 and 1000). Water uptake isopiestic curves.

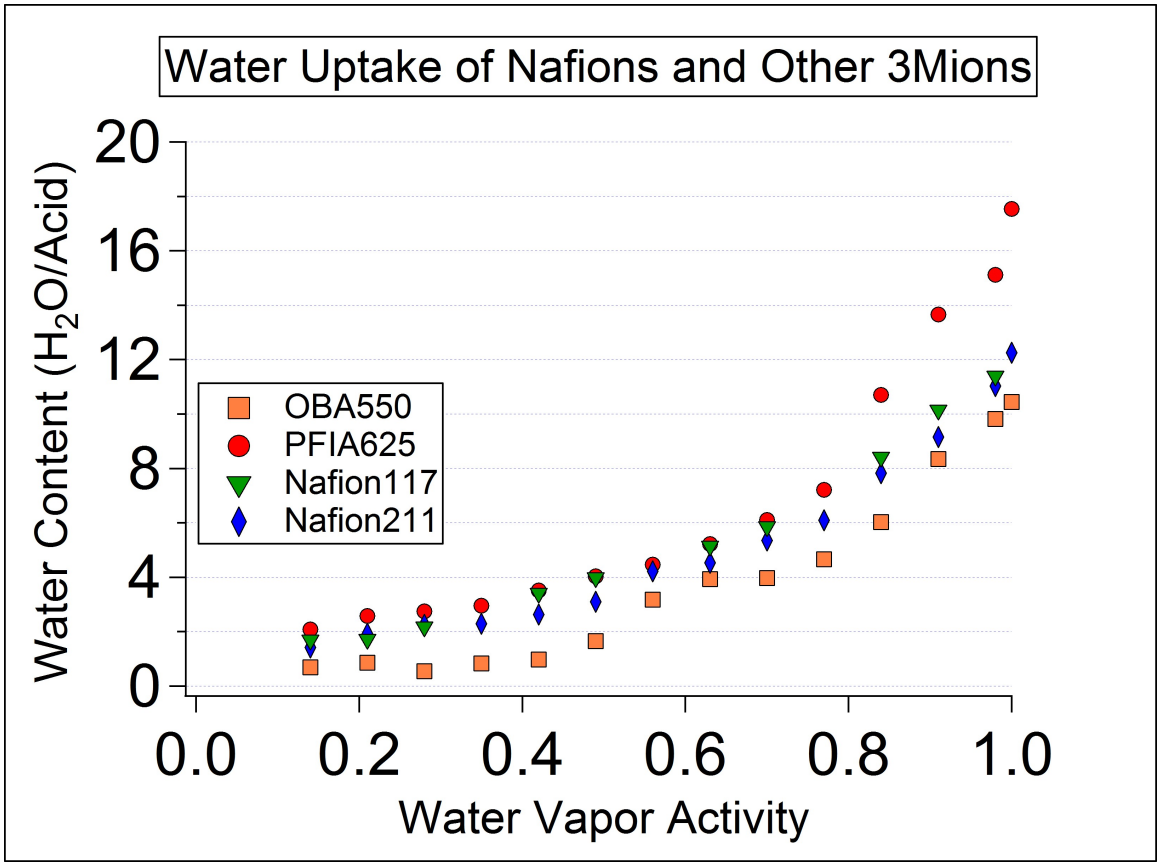


Figure 2.3 Water Uptake of OBA, PFIA, Nafion®117 and Nafion®211

Fig 2.3 shows the water uptake of other measured polymers including PFIA, OBA, Nafion®117 and Nafion®211. PFIA has similar water uptake to the 3M PFSA, while the water content of OBA is substantially lower compared to the other membranes. The OBA membrane has imide linking structure and an extra sulfonic site, attached to a phenyl ring, in the side chain, which might be expected to lead to a higher λ. However, interestingly, the material showed relatively lower water contents than the other polymers under all hydration conditions. We suspect that other aspects of polymer morphology lead to the low water uptake. More details about polymer morphology will be discussed in the partial molar volume section.

2.3.2 Enthalpy

The enthalpy measurement of Nafion®117 was carried out using precision solution calorimetry. The heat change was divided by the equivalent weight of Nafion®117 (1100) and thus normalized to enthalpy per sulfonic acid group, shown in Fig 2.4. The mixing of membrane with water is an exothermic process, represented by the negative sign of ΔH. As it was defined before, the heat change ΔH_x is from x state to fully hydrated state H_0. The enthalpy of membrane decreases logarithmically with increasing hydration level (λ) in membranes. This process is exothermic. Thus, the trend suggests that water molecule and acid group interaction releases heat, while more heat was released at low water contents than that at high water contents. In another word, at poor hydration conditions the water-polymer interactions are much stronger than at high hydration conditions. The logarithmic feature in Fig 2.4 also shows that at relatively dry

condition the heat changes rapidly, while at relatively wet condition the heat generation tends to reach zero. This suggests that either the initial water molecule interaction with the acid groups significantly hinder the following water molecule interaction during water uptake; or the initial water molecules break the bonds in between side chains, which generates significantly amount of heat. (More discussion of this behavior in the PMV section) To further investigate the energy associated with the water uptake process, the free energy is calculated from the water uptake data.

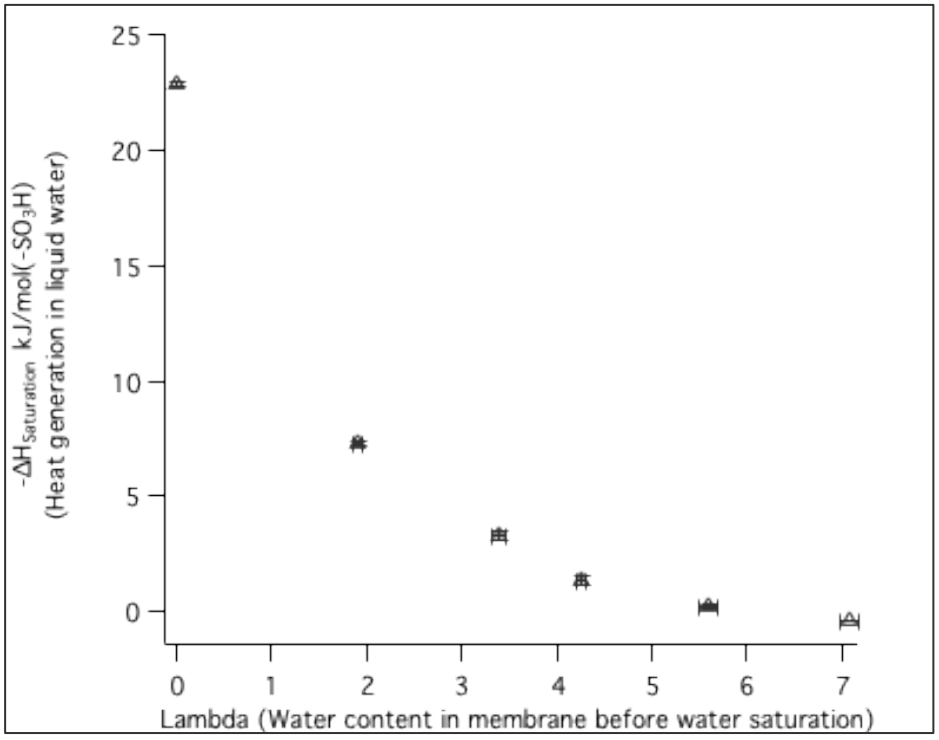


Figure 2.4 Heat Generated of Nafion®117 in Contact with Liquid Water

2.3.3 Free Energy

The water uptake data could be used to analyze the free energy change associated with the uptake process per water molecule. Based on some basic thermodynamic relationships shown in equation (13) and (14), ΔG can be expressed as in equation (15), which is defined as the free energy change of water from a certain hydration level to fully hydrated state.

$$\Delta G = \lambda(\mu_f - \mu_i) \quad (13)$$

$$\mu = \mu^o + RT\ln a_w \quad (14)$$

$$\Delta G = \Delta G^0 - \lambda RT\ln a_w \quad (15)$$

Where, λ is water content; μ is the chemical potential; R is the gas constant; T is temperature; a_w is the water activity according to the hydration level; ΔG^0 is -228.6 kJ/mol (*Handbook of Chemistry and Physics*)

In Fig 2.5, the free energy is generally divided into two parts. At $\lambda<3$ is relatively high and stays at -222kJ/mol, after $\lambda>3$ the free energy change decreases gradually. This implies that the majority of the free energy change is associated with the ionizing and dissolving of protons by water on the sulfonic acid groups as water uptake first take place in membrane. Less and less free energy is associated with water uptake process beyond $\lambda=3$. Water is weakly bound and there is a smaller driving force for additional water to absorb into the membrane. It is at these higher water contents that the membrane further expands (swells), forming the more extensive conduction networks for proton transport.

Combined with the enthalpy change shown in Fig 2.4, this suggests that the membrane water uptake is such a process: Beginning from a dry membrane, as water is introducting into the membrane, significant heat is released from bonds dissociating and proton dissolving; as more and more water molecules are absorbed into the membrane, less and less heat is generated per additional water molecule and the uptake free energy decreases as well; eventually, the membrane reaches an equilibrium such that no more heat is generated as water is taken into the membrane and a small free energy is associated with this process.

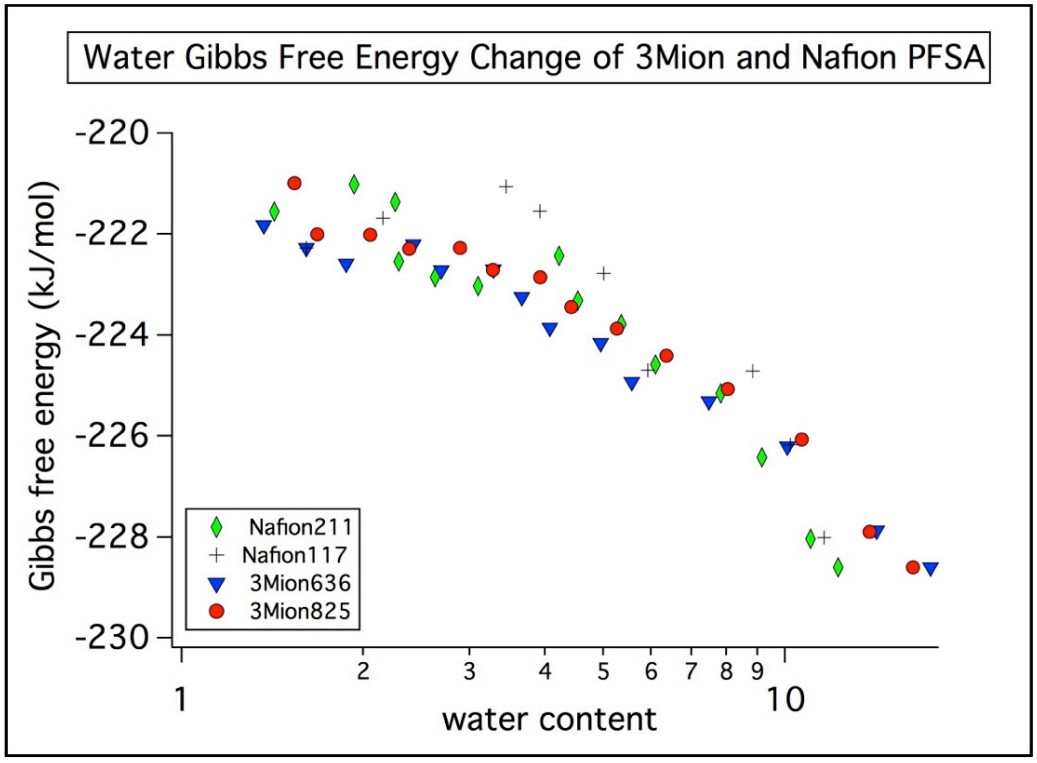


Figure 2.5 Gibbs Free Energy of Water Uptake.

2.3.4 Density

The density of membranes in Polymer Electrolyte Membrane Fuel Cells (PEMFC) is an important parameter that has not been widely measured. A knowledge of the density as function of water content serves several purposes. Density is a key parameter in the analysis of conductivity, in providing benchmarking for theoretical analyses of membrane structure and. In its own right, density can be analyzed to provide the partial molar volume of water and membrane components. The following experiments describe the experimental and mathematical methods we were using to obtain the partial molar volumes. Water uptake was controlled to measure the membrane density at different hydration level. The membranes were sealed in either glass vials or a pycnometer sample compartment. We then assume the hydration level does not change during a measuring cycle. To validate our assumption, we weighed our samples before and after the density measurement, and the water loss/gain is less than 1% which is considered negligible. Derived from the density, the partial molar volumes are analyzed, and give us more details about properties of water in membrane.

Gas displacement pycnometers use helium to pressurize the sample compartment. The pressure in the compartment obeys Boyle's Law, which was applied to calculate the volume of our membranes. Due to the small molecular size of helium, gas displacement pycnometry allows helium molecules to fill in vacancies and pores of membranes and precisely measures the volume of membranes and water in them. Membranes were equilibrated under various water activity conditions for days before density measurement.

In Fig 2.6, despite some scatter in the data, the densities of 3M PFSAs with different equivalent weights show a similar trend. The densities slightly increase as we increase water content to $\lambda=4$. This suggests either the volume of the membranes shrinks as water enters or that the water molecules pack into the membranes in such way that make the membranes denser. More analysis of this is discussed to interpret these data and to determine which mechanism is preferable in the partial molar volume section. At high water content where $\lambda>4$, the densities of 3M PFSAs decrease gradually, which means at high water content the membranes expand and densities decrease as expected for an averaging between polymer density and water density. Comparing the membrane densities of the highest water content to dry condition, 3M PFSAs densities drop about 15%. In Fig 2.7, it shows that Nafion® PFSAs (Nafion®117 and Nafion®212) exhibit similar behavior to that of 3M PFSAs. At water content where $\lambda<4$, the densities of Nafions® slightly increase and at water content $\lambda>4$, the densities start to decrease. There is a difference of 0.3 g/cm^3 in densities between Nafion®211 and Nafion®117. We assumed this difference came from the crystallinity difference due to their different casting methods. The environmental vibration and experimental error cause some acceptable scatter in the data.

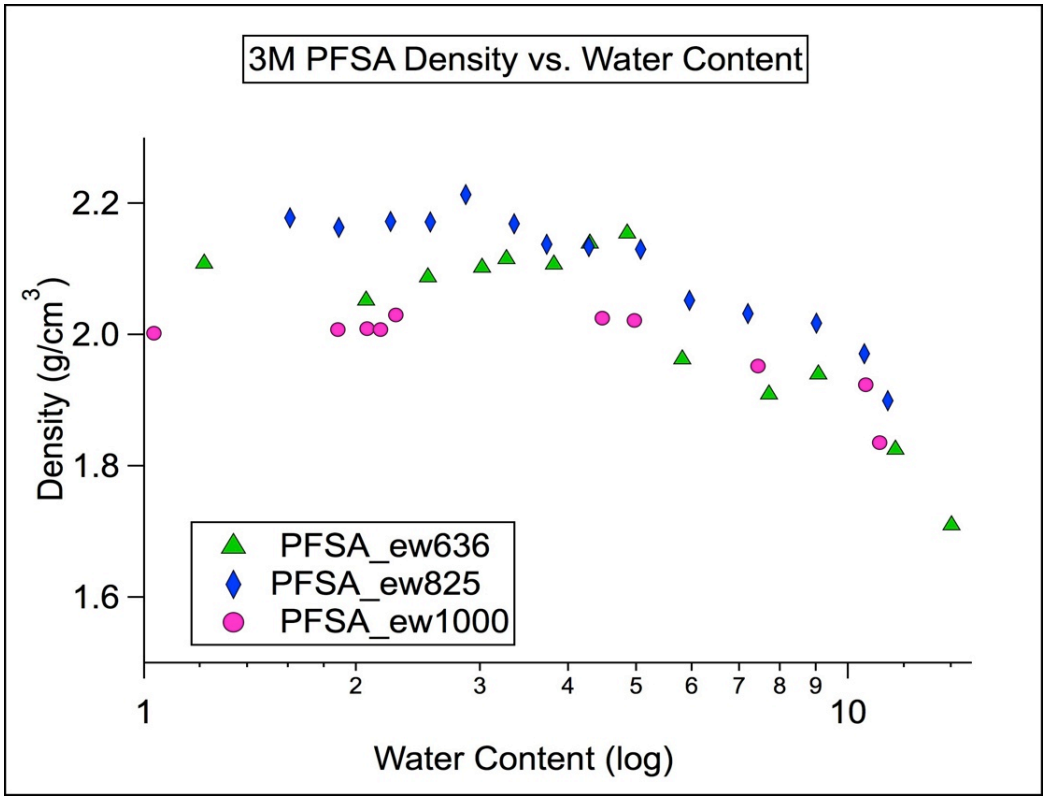


Figure 2.6 Density of 3M PFSAs with different equivalent weights.

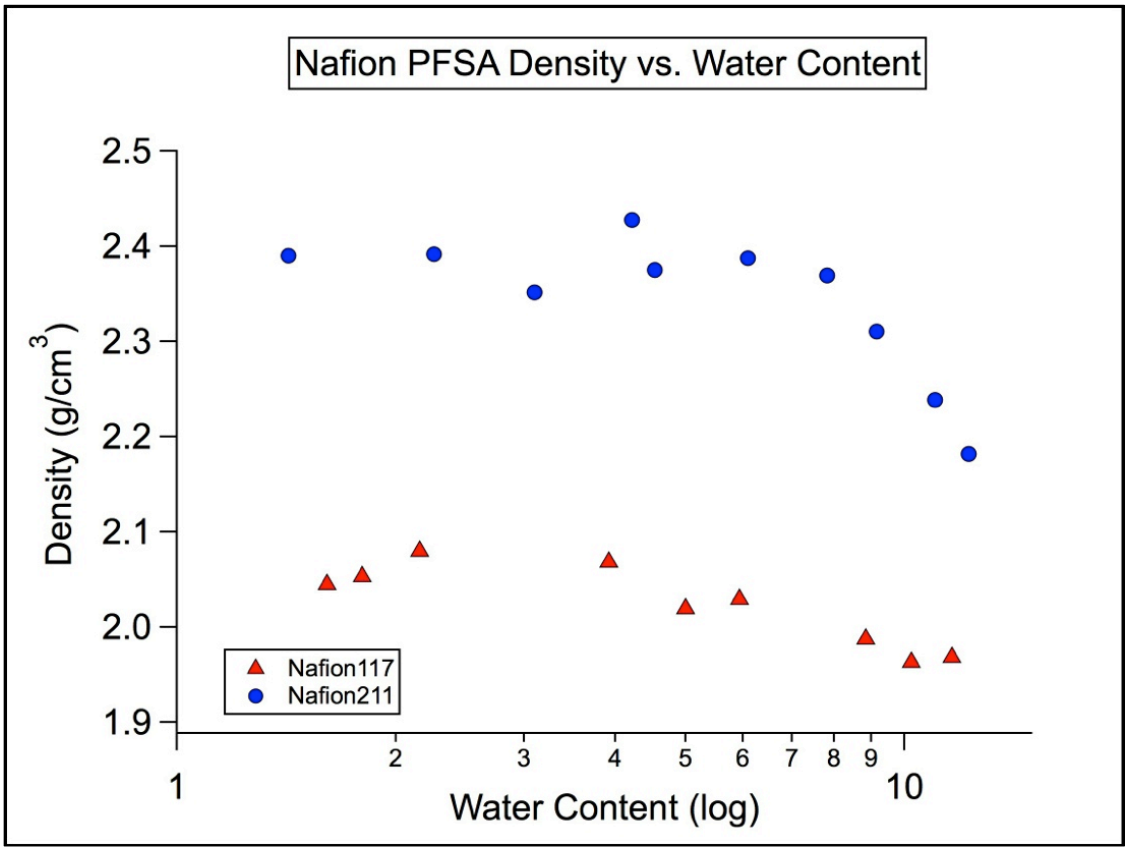


Figure 2.7 Densities of Nafions® membranes

In Fig 2.8, the 3Mion OBA and PFIA show some different trends from the PFSAs. The PFIA density simply decreases with increased water content. The reason is unclear, but it implies that all water molecules entering the polymer makes it swell in volume and decrease in density. This is closely related to the polymer structure inside the membranes. Compared to PFSAs, initially those water molecules imbibed into the PFIA did not increase the density of membrane.

However, the OBA shows a very different behavior. The water content reaches as low as $\lambda=0.5$ under our hydration conditions, which is much lower than most other types of membrane under same condition. It is the only membrane that we could obtain the water uptake data in this region. Thus, it helps us to study the water and polymer behavior at extremely low water content. Fig 2.8 shows at low water content ($\lambda <1$) the density of OBA does not change, followed by a density drop at higher water content. To further investigate the features of different types of membranes as well as the interaction between water and polymer, we use the density data to systematically calculate the partial molar volumes.

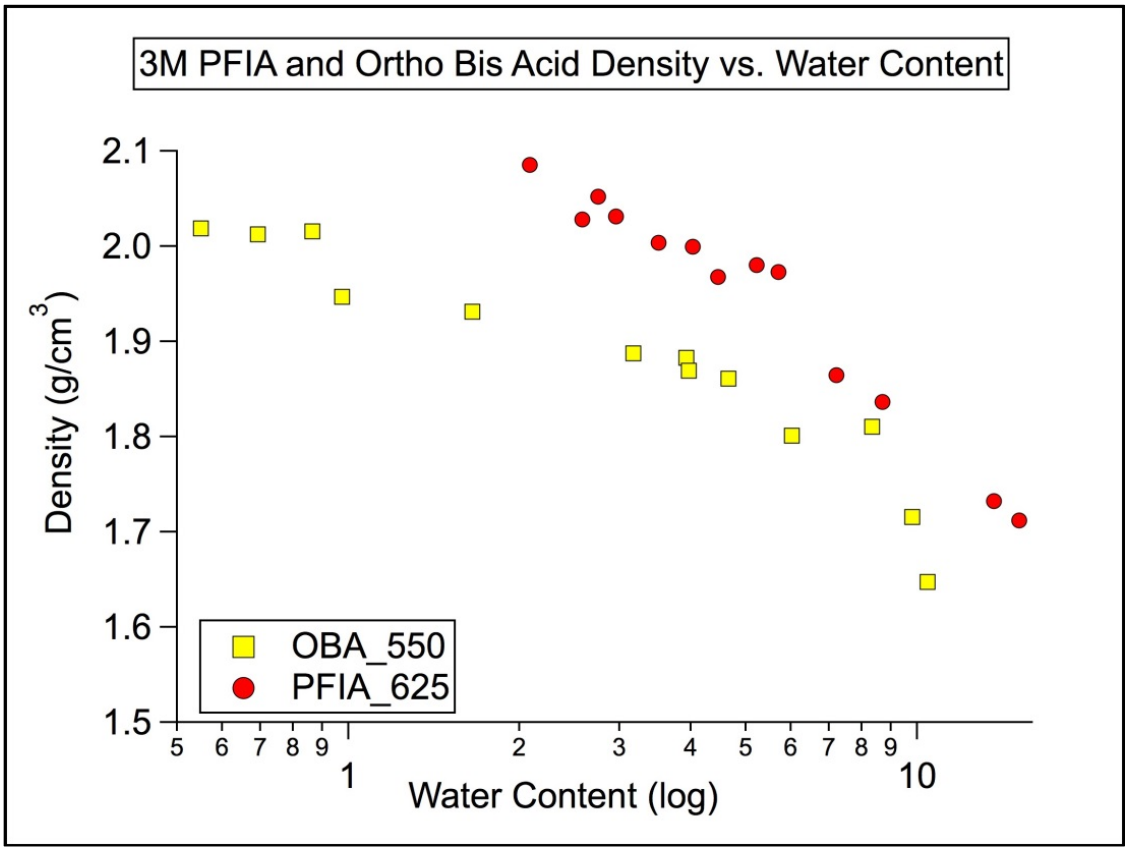


Figure 2.8 Densities of 3M PFIA and OBA.

2.3.5 Partial Molar Volume

2.3.5.1 Calculation. Partial molar volume is often applied in many areas to analyze the composition and thermodynamics in a mixture system on a per mole basis. Due to the uncertainty of the molecular weight of polymer, we first defined the per mole basis as the amount of polymer with 1 equivalent weight. Because the equivalent weight is a characteristic property, which is fixed for the same type of polymer, we are able to proceed to calculate the partial molar volume based on it. The partial molar volume of water is calculated by adding small quantities of pure water to pure polymer (dry) and measuring the volume change of the system (water and polymer combined). This procedure was achieved by implementing our water uptake experiment. After each water addition, the differential system volume change is the partial molar volume of water. Following are the detailed calculations of the partial molar volume based on pycnometry measurements.

As we mentioned before, the molar mass for each component is required for standard analysis. For most ionomers, the polymer molecular weight is distributed over a wide range and/or is simply unknown. Instead, we based our analysis on the polymer equivalent weight, thus obtaining the partial molar volume corresponding to one equivalent of polymer. We take 3M PFSA 825 as an example to illustrate the calculation of the partial molar volume for both polymer and water. For each equivalent weight of polymer 825 g/mol, λ moles of water were absorbed at each water activity according to the water uptake experiment. The calculation of theoretical volume V^* and actual volume is described in the following equations:

$$V^* = n_w V^*_{m,w} + n_p V^*_{m,p} \quad (16)$$

$$\Delta V_{MIX} = V - V^* \quad (17)$$

V^* is the theoretical system volume at constant temperature and pressure; n_w, n_p are moles of water and polymer associated with one acid site; $V^*_{m,w}$, $V^*_{m,p}$ are the molar volume of water and polymers; ΔV_{MIX} is the difference between actual volume and theoretical volume calculated as the sum of the volumes of the pure species. For one equivalent the moles of water and polymer is defined as: $n_w=\lambda$, $n_p=1$. The molar volume of water is $V^*_{m,w}=18.01$ cm^3/mol. The molar volume of polymer can be calculated as: $V^*_{m,p}$=EW/dry density of PFSA825. The dry density is obtained from pycnometry. Thus, $V^*_{m,p}=$ 380.25 cm^3/mol.

We plot $\Delta V/n_T$ vs. X_w, where n_T is the total moles of components in the system (n_w+n_p). According to the definition of partial derivative, the partial molar volume is the derivative of system volume with respect of the moles of water. The derivative is obtained from the slope of curve at each point in Fig 2.9. Thus the partial molar volume of water at a given water mole fraction X_w can be calculated from equation (16) and (17). The partial molar volume of the PFSA 825 at the same water mole fraction can then be determined for the y intercept of the tangent line at $X_w=0$, shown in Fig 2.10. Based on our measurements and experimental condition, data points where Xw<0.6 are very limited.

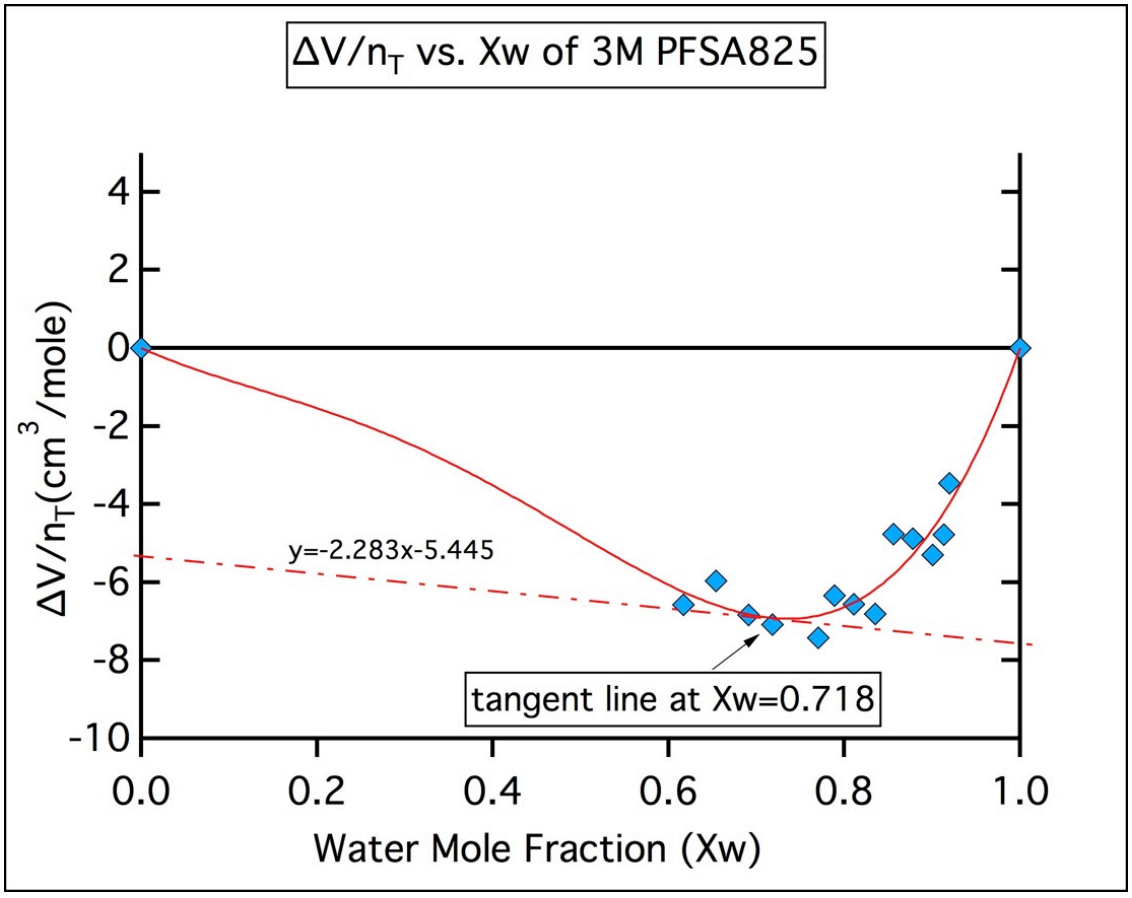


Figure 2.9 Curve Fitting of 3M PFSA825.

The Redlich-Kister equation (18) is used to fit our experimental data, with constraints that the extreme points at X_w=0 and X_w=1 yield no excess volume of mixing. And the intercepts and tangent line are found to calculate the partial molar volume from following equations:

$$V_m^E(cm^3mol^{-1}) = x_1(1-x_1)\sum_{i=0}^{k} A_i(1-2x_i)^i \tag{18}$$

$$y-y_1=m(x-x_1) \tag{19}$$

$$V_{PM,W}= \Delta V_{MIX}/n_T+V_{m,W} \tag{20}$$

Equation (19) is tangent line equation calculated from the curve fitting, from which we obtained intercept $\Delta V_{MIX}/n_T$. y_1,x_1 are the $\Delta V_{MIX}/n_T$, X_B coordinates at any specific point, m is the slope of the tangent line at (x_1,y_1). Thus the partial molar volume is calculated by equation (20).

2.3.5.2 Partial Molar Volume. The partial molar volumes for different types of membranes are shown below. Despite some scatter and discrepancies, water in different types of membrane shows similar behavior. Fig 2.10-2.12 show at low water hydration level when $\lambda<2$, the partial molar volumes of water are very small and even less than 10cm^3/mol for some cases. Meanwhile at $\lambda>2$ the partial molar volumes of water increase gradually and eventually reach steady plateaus approximately 18 cm^3/mol at $\lambda>6$. This behavior suggests that when $\lambda<2$ water somehow packs into the polymer in another form and this part of added water leads to a much smaller total volume increment than

18cm^3/mol observed when water is in form of free liquid water. As we increase water uptake, at $\lambda>6$, the water partial molar volumes stabilize at a plateau of 18cm^3/mol. Given that 18 cm^3/mol is the molar volume of pure liquid water, it suggests that at $\lambda>6$ the water absorbed into the membrane tends to behave like free liquid water. Hereby we assume the possibility of composition regimes in corresponding to three environments for water in the membrane: $\lambda<2$, $\lambda>6$, and the composition range in between these two extremes, which corresponds with observations by Kim *et al*. using DSC to characterize these three states. According to the simulation of Hwang *et al*., they showed the two different states of water in small domains and large domains, respectively. The smaller domains readily fill water and form network pathways with the strong overlapping surface forces to retard other water molecules transport. The larger domains contain more free water, which benefits both water uptake and proton transport properties. From the perspective of our density measurement, the membrane density drops as the water partial molar volume approaches 18cm^3/mol, i.e. the membrane expands and creates more large domains that allows water absorbed in as free water molecules. Thus, at $\lambda>6$, the membranes are fully extended with channels or vacancies for free water to fill in. From $\lambda=2$ to 6, the water molecules tend to pack into small domains and do not affect the total volume as much.

Fig 2.10-2.12 also show the partial molar volumes from the perspective of polymers. The partial molar volumes of polymers behave in a complementary way to the trend for water, which agrees with the Gibbs-Duhem relationship. Similarly, although the actual morphology and structures of the polymers are unclear, we conjecture three forms of polymer existing with water uptake: $\lambda<2$, $\lambda>6$ and λ in between these two extremes. At

λ<2 polymers appear to have a larger partial molar volume, while at λ>6 they reach plateaus with lower partial molar volume.

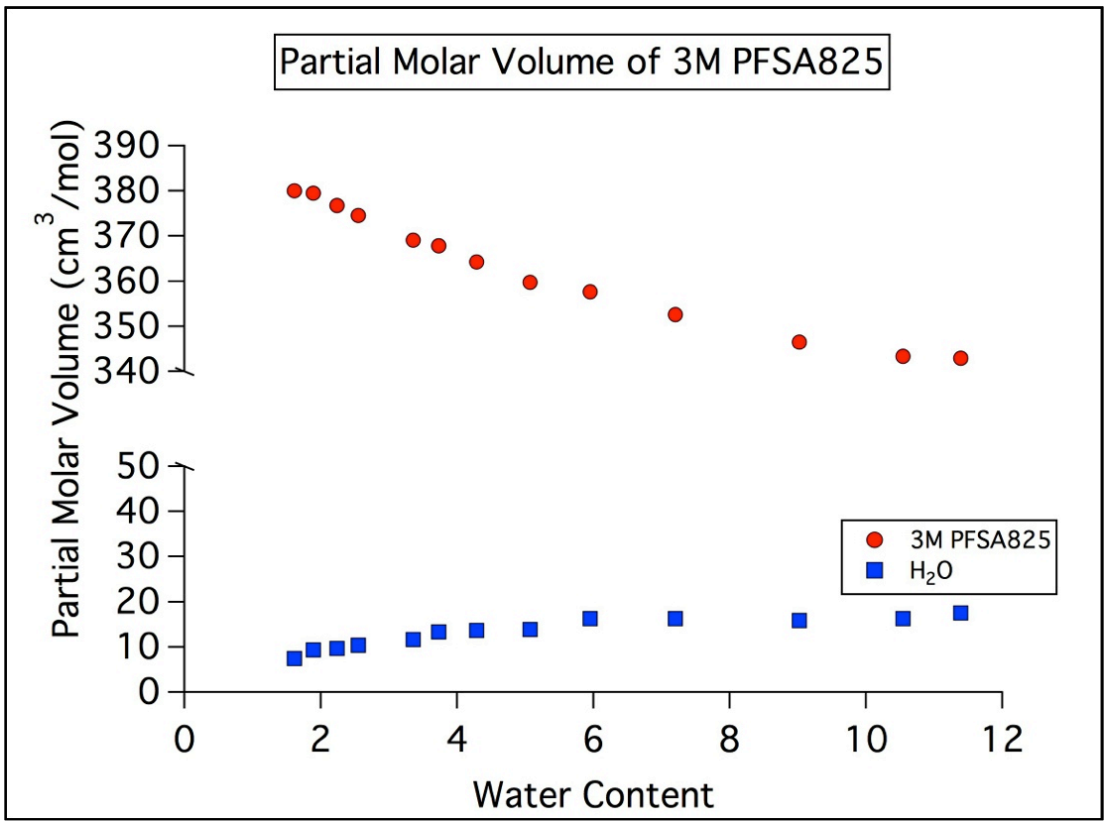


Figure 2.10 Partial molar volume of 3M PFSA825.

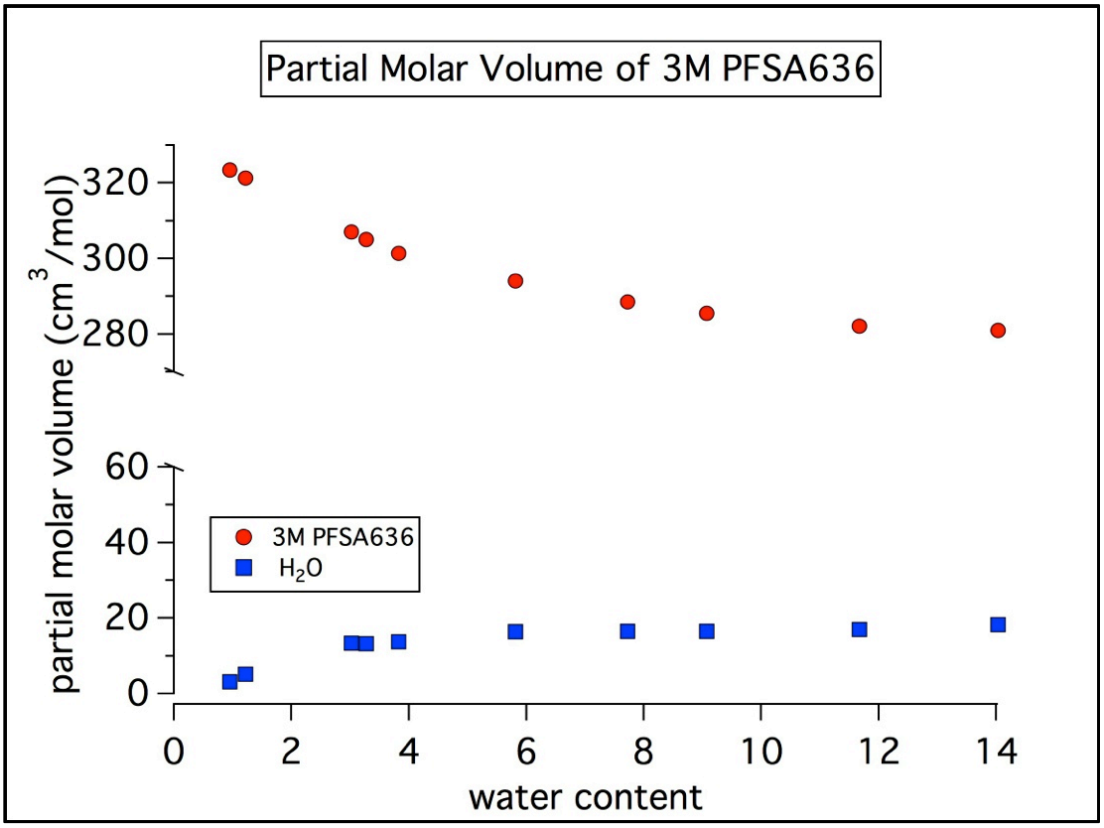


Figure 2.11 Partial molar volume of 3M PFSA 636

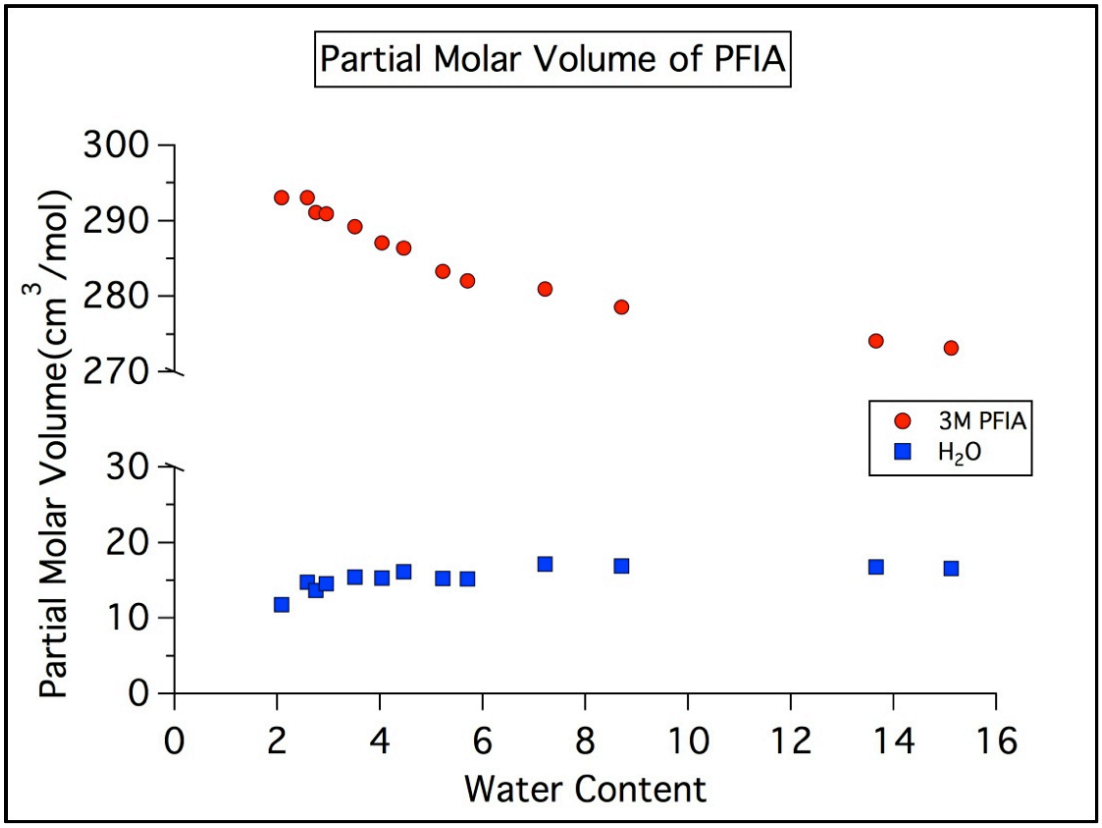


Figure 2.12 Partial Molar Volume of 3M PFIA

However, the partial molar volumes of OBA and Nafion®211 indicate a possibility of another state of water or uptake mechanism at even lower water content. In Fig 2.13-2.14, Nafion®211 and OBA show very high partial molar volumes of water at extremely dry condition, and they decrease as more water is taken up. At higher water content, they increase gradually as other membranes. Noticed that the initial water partial molar volume of OBA is even higher than $18cm^3/mol$. In another words, one mole of water increment leads to a system increment more than $18cm^3$. This suggests that a highly strong interaction between water and polymer at extremely dry conditions, which is also presented as a major heat generation from the calorimetry measurement. Under these extremely dry conditions small amount of water absorbed into the membrane can dramatically increase the system volume. For these cases, we presume that the polymer chains are tightly packed when dry, driven for example by H-bonding. The water uptake breaks up the H-bonding and "uncoils" the polymer; for this, one would observe an apparent increase in polymer partial molar volume and a high water partial molar volume. Once the polymer chains are fully extended i.e when more water molecules are imbibed by the polymer, the polymer-polymer swelling proceeds normally, with a density drop.

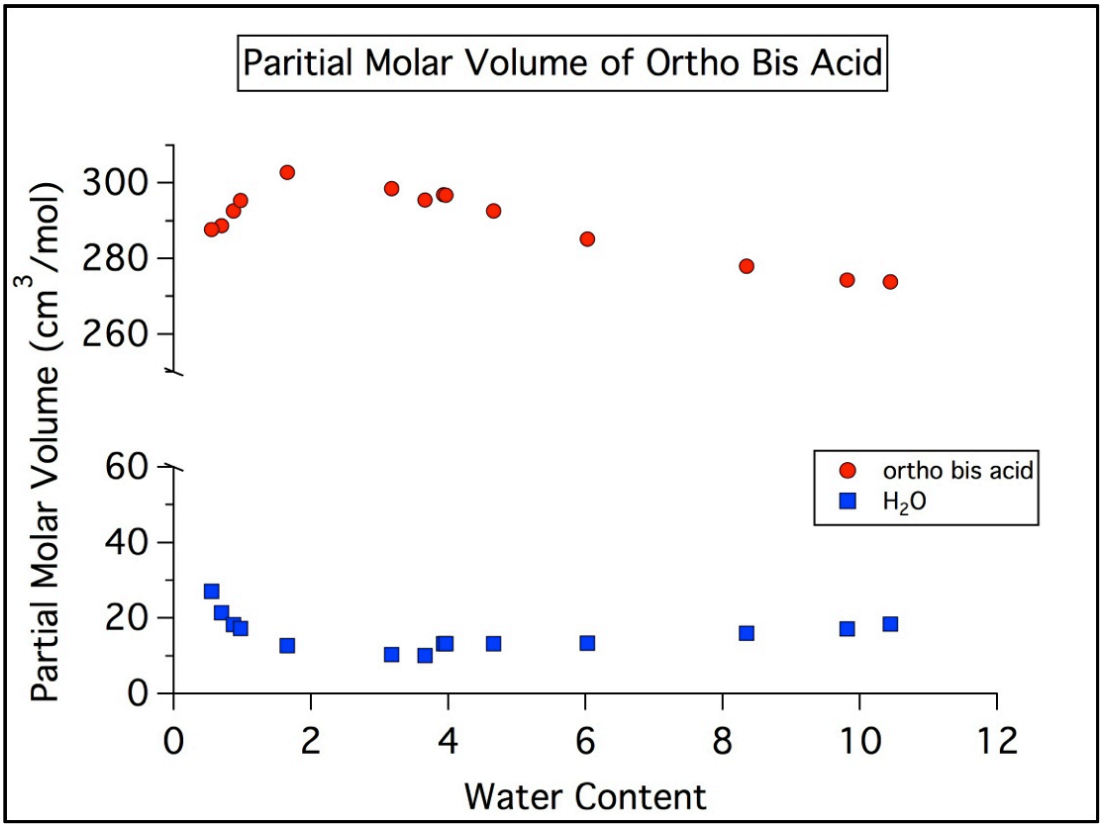


Figure 2.13 Partial Molar Volume of OBA.

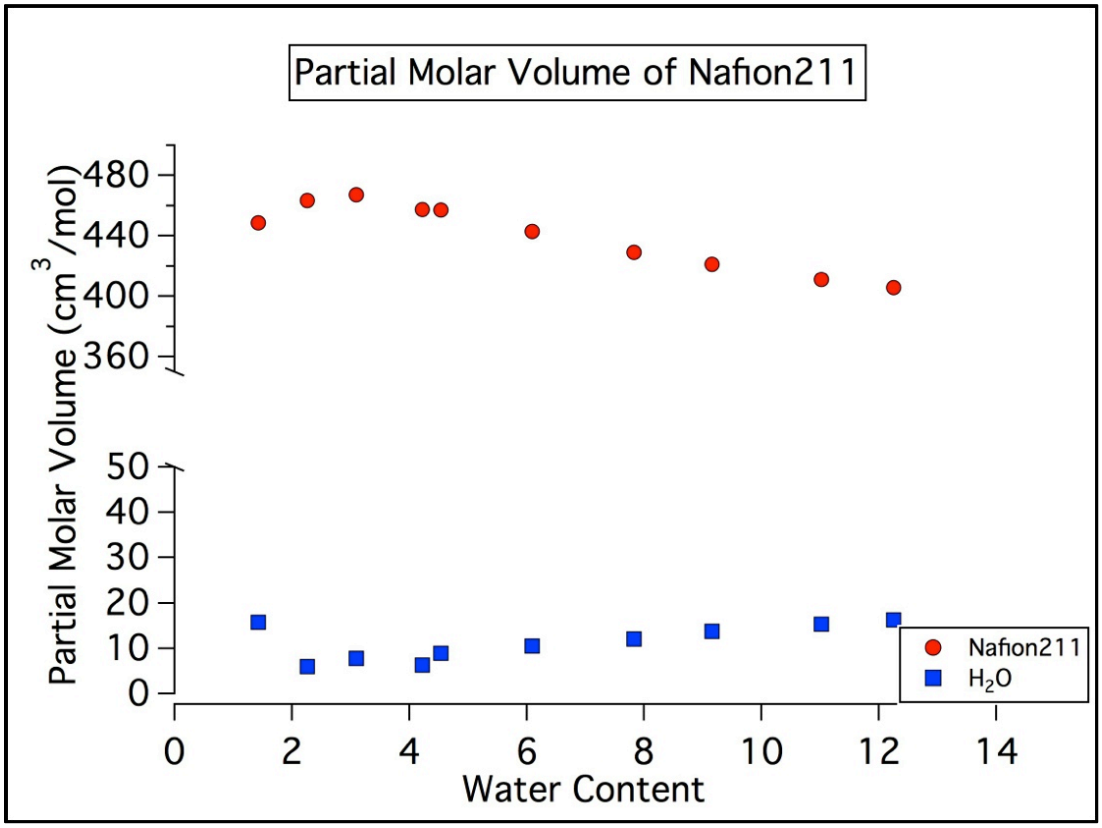


Figure 2.14 Partial Molar Volume of Nafion®211

3.4. Conclusion

Densities of different types of membranes used in PEM fuel cell were measured. We compared the water uptake, density and partial molar volume of several proton-conducting polymers used in polymer electrolyte membrane fuel cells. The water uptake experiment validates the previous studies: strong interactions exist between water protons and sulfonates at low water content, gradually giving way to weaker interactions between water and the membrane at higher water content. The membrane water uptake goes through such processes: at the beginning, water first enters into the membrane, significant heat is released from bonds dissociating and protons being hydrated; as more and more water molecules are absorbed in the membrane, less and less heat is generated and the free energy decreases as well; eventually, the membrane could reach an equilibrium state in which no more heat is generated as water goes into the membrane and little free energy is associated with this process, thus water transport in the membrane freely. A new concept is defined as partial molar volume of the polymer segment corresponding to one equivalent to interpret water and polymer interaction. We successfully deduced a series of equations to express the partial molar volume for both water and polymer. For the first time they were used to analyze the states of water in the membranes. We inferred three states of water associated with specific water contents in accord the previous differential scanning calorimetry studies. Generally, the water presents three forms in the membrane: at $\lambda<2$ water packs into polymer in this form that the added water leads to a much smaller total volume increment than liquid water; at $\lambda>6$ water presents the characteristics of free liquid water; and there is water in between these two states with loose bounded water

from λ=2 to 6. The study of partial molar volumes of 3Mion OBA and Nafion®211 shows the possibility of another uptake mechanism. In this case, at extremely low water content, water molecules interact with the polymer and exhibit a large partial molar volume. We presume that the water uptake breaks up the H-bonding and "uncoils" the polymer to apparently increase the system volume. From a broad perspective, with pycnometry measurement, the partial molar volumes could be used to conjecture possible states of any other components in the membranes.

Chapter 3

Performance Study of Hydrogen Bromine Redox Flow Batteries

3.1. Introduction

The hydrogen-bromine redox flow battery system is considered to be a good candidate for large-scale energy storage because of its inexpensive reagents, low kinetic loss and low self-discharge rate. In this paper, we studied the cell performance by analyzing the area specific resistance (ASR) under different experimental conditions. A dynamic hydrogen electrode (DHE) was assembled in the cell to separate the membrane as well as the electrodes on both sides to study and elucidate bromide/bromine electrochemical performance independently. Our work indicates that the ASR from the proton exchange membrane is the main loss channel for hydrogen-bromine redox flow batteries. The impact of performance and ASR were studied by varying experimental temperature, thickness of the carbon electrodes and acid concentration in the membrane. Ex-situ study of acid/water uptake and transport of HBr into the membrane shows that acid concentration has a significant impact on the proton conductivity in membranes, and suggests that 2 mol/L of hydrobromic acid is the optimal concentration for maximal membrane conductivity.

Hydrogen bromine redox flow batteries meet many of the key requirements for a large scale energy storage system. It has a high electric to electric efficiency and inexpensive reactants compared to many other redox flow batteries. The general cell structure of hydrogen bromine redox flow batteries is similar to that of traditional

hydrogen oxygen PEM fuel cells. Yeo *et al* have used experimentally and theoretically approaches to determine the feasibility of a hydrogen-bromine cell for energy storage applications.[210–212] A flow-through electrode was used in their flow battery. Membrane HBr acid uptake and conductivity were measured under various HBr concentrations. Peled *et al*. assembled and tested a hydrogen bromine fuel cell with a flow-by electrode with relative high platinum loading of 1.5mg/cm^2 platinum loading. The maximum power density they reported was found to be 1.5W/cm^2 under varying experimental conditions. The differences between flow-by and flow-through modes were compared, using a similar experimental setup by Cho *et al*.[213] Meanwhile, the cell was modified by removing the platinum from the positive electrode. The performance showed similar power densities of 1.4W/cm^2 compared to previous work. Commercial Nafion®212 MEA was used in this study. The hydrogen-bromine redox couple showed less kinetic loss than hydrogen-oxygen during charge and discharge polarization curves.

Platinum was adapted from traditional fuel cells to use in the hydrogen bromine redox system. RDE experiments are commonly used to study the kinetics of hydrogen/bromine on platinum. Studies show that the presence of Br- weakens the Pt-H bond in the oxidation reaction of hydrogen, which leads to a lower limiting current in HBr system. The bromine kinetics on the positive electrode is more complicated. The Br- ion on the Pt surface is chemically adsorbed in a partially charge transferred state while competing with OH and O generation. This suggests that Br^- chemisorption is sufficiently strong to block anodic oxide film formation to a large extent. Cyclic voltammetry studies also show that the poisoning effect of bromine on platinum is irreversible even at low Br^-

concentration.[198] Heat-treated platinum alloy electrodes were prepared and showed improved resistance to bromide ion corrosion. The exchange current of the bromine/bromide reaction on Pt is calculated as a quarter of that of the hydrogen reaction. However it is feasible to replace Pt with carbon electrodes on the positive electrode.

A key component in hydrogen bromine redox flow batteries is the membrane. Basic requirements for the membranes include a high proton conductivity to minimize the cell resistance and adequate chemical barrier properties combined with good mechanical and chemical stability to maximize the lifetime of the system. The bromine/bromide transport and stability in the ion exchange membrane has been studied.[199] Low cost nanoporous proton-conducting membranes were prepared and tested in hydrogen bromine batteries.[203] To investigate the cell resistance associated with the membrane, here we demonstrate several methods including ex-situ measurement of acid/water uptake membrane conductivity, in-situ measurement of experimental condition using charge and discharge polarization curves and electrochemical impedance spectroscopy. A dynamic hydrogen electrode (DHE) was installed in the battery. Area specific resistance (ASR), measured with the assistance of a DHE electrode, will be presented in this chapter.

3.2. Experiment

3.2.1 Cell Configuration

The single cell is adapted from 5 cm^2 active area DMFC hardware with flow channels drilled through the metal endplates (Fuel Cell Technologies, Inc.). The cell

hardware includes two aluminum end plates, gold-plated current collectors, and sealed graphite plates engraved with a single-serpentine flow channel. Membranes used in this study include Nafion®117, 212, 211. Carbon paper (SGL Technologies 10AA) was used on positive electrode. TGP-H90 Teflon treated carbon paper (280um) was applied to negative electrode. A commercial MEA (SGL Technologies) with Nafion®212 and 0.4 mg/cm^2 Pt loading on both sides of the membrane was used for initial experimental setup. A "half MEA" was prepared for the remaining experiments with the negative electrode hot-pressed with platinum/carbon mixture. The Pt/C powder has 30% Pt on carbon in weight percentage, and the Nafion solution is measured to achieve a 5:2 weight ratio of catalyst to Nafion. Thus, the Pt loading can be calculated from the experimental procedure. In general, our experiment uses 7mg ink per MEA, which provides a $0.3mg/cm^2$ Pt loading. We adapted a "zero-gap" design developed by Aaron *et al* [214]. This structure means that the membrane, electrodes, and current collectors were in direct contact. This is proven to minimize the ionic and contact resistances between the membrane and electrode. A temperature controller was used to control the cell temperature.

A series of concentrations of HBr acid and Br_2 was prepared. PTFE tubing and pump were used. The battery was setup in a fume hood. The flow rate was controlled from 10 mL/min to 50 mL/min. Single pass mode was used on hydrogen electrode, which means the hydrogen passed through the electrode without recycling it. The hydrogen was humidified through a humidity bottle heated by a hot-plate with temperature controlled according to different experimental conditions.

An HCP-803 potentiostat with an 80A booster and a VMP3 potentiostat with a 20A booster channel (Bio-Logic Co.) were used for electrochemical measurements including chronoamperometry (CA), open circuit voltage (OCV), and potentiostatic electrochemistry impedance spectrometry (PEIS).

3.2.2 Acid Uptake and Conductivity

The pretreated membranes were cut into 1x6cm strips and were immersed in HBr over the full concentration range from 0M-8.7M. After the membranes reached equilibrium in 30 minutes, the membrane surface was wiped by Kim-wipes to remove any droplets. The weight of the sample was recorded instantly as m_t which includes the weight of the membrane m_m, the weight of the water uptake m_w and the weight of acid uptake m_a as in equation (21).

$$m_t = m_m + m_w + m_a \tag{21}$$

The acid uptake was obtained by titration. The dry membrane weight was measured after dehydration in a vacuum oven. The weight of the water uptake was calculated by equation (1). A DL15 titrator (Mettler Toledo) was used to titrate the acid in membranes. Each membrane was boiled into 100ml DI water at 100 °C for 1 hour. HBr was leached from the membrane to the DI water. The membrane was then taken out and kept in a small vial. The boiled DI water was kept and titrated by NaOH with DL15 titrator. The HBr acid taken up by the membrane, m_a, was calculated from the amount of

NaOH required to neutralize the acid. Following this, the membrane was dried in a vacuum oven at 90°C for 4 hours and weighed as m_m. The water uptake m_w was calculated by equation (21).

A four-point conductivity cell was used for conductivity measurement. The membrane was cut into 1x6 cm strips. Some modification was made to the conductivity cell to improve the stability of results, including adding gaskets to the cell and sealing the windows with Kapton®. Equation (22) shows the calculation of conductivity with high frequency resistance of membrane:

$$\sigma = \frac{1}{\delta \times w \times \Omega} \tag{22}$$

σ represents the conductivity of the membrane; Ω is the high frequency resistance; δ is the thickness of the membrane; and w is the width of the membrane. The thickness and width of the membrane were measured with a caliper. The high frequency resistance (HFR) is measured with a VMP3 Multichannel Potentiostat (Bio-Logic) in an environmental chamber (WATLOW) at fixed temperature

3.2.3 Dynamic Hydrogen Electrode

A DHE electrode was inserted in the cell to study positive and negative electrodes separately. The method was adapted from all-vanadium batteries.[215] Fig 3.1 shows the configuration of a DHE reference electrode. This device utilizes two platinum wires sandwiched between two membranes. A 9V battery and a 15 MΩ resister were connected

into the circuit. This circuit provides a small current which forms a thin layer of hydrogen bubbles on the platinum surface and establishes a potential between the platinum wire and water between the membranes to serve as an in-situ reference electrode. A DHE with single membrane was also tested in our cell. The structure is very similar to that of the two-membrane setup. Instead of sandwiching the Pt wires in between two membranes, we put the Pt wires on each side of the membrane.

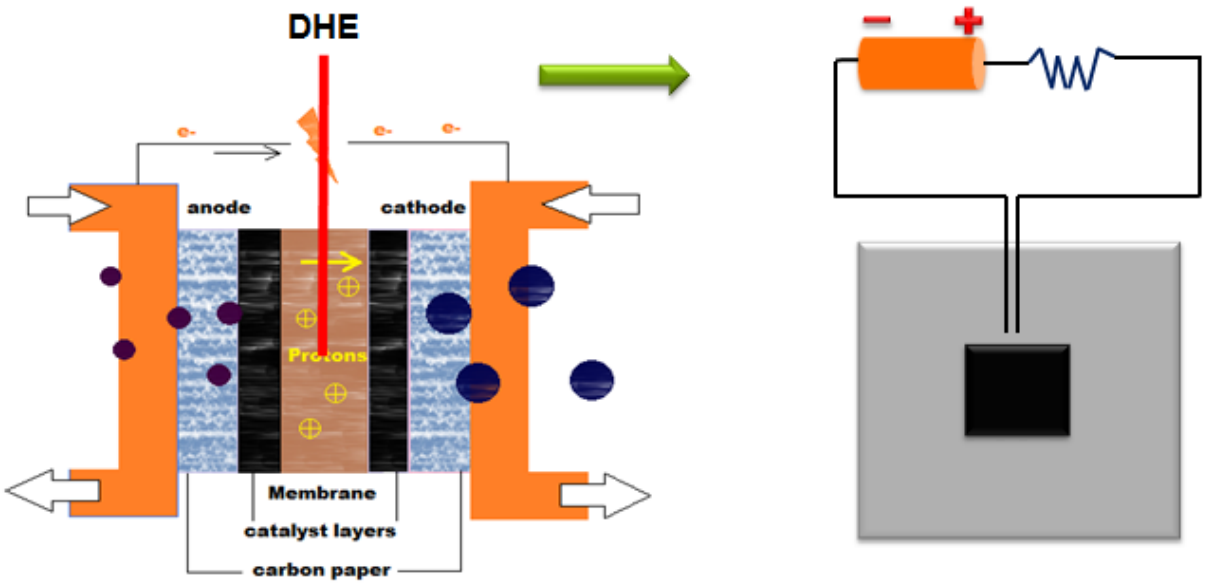


Figure 3.1 Schematic of a DHE in the Hydrogen Bromine Redox Flow Battery

3.3. Results and Discussion

3.3.1 Acid/Water Uptake and Conductivity Measurement

To study the membrane resistance and its effect on cell performance, we measured the water and HBr acid uptake in *ex-situ* experiments. Previous studies with membranes of the same equivalent weight shows a very similar trend in H_2SO_4.[216] Therefore, we use Nafion®117 as an example to demonstrate the acid/water uptake and conductivity measurement in the hydrogen bromine system. Nafion®117 membranes were equilibrated in HBr before being boiled in DI water. The amount of acid was measured by titrating the residual acid in DI water. The boiled Nafion®117 was dried to measure the dry weight. Water uptake was calculated by subtracting the weight of acid and dry Nafion®117 from the equilibrated weight. Fig 3.2 shows the water and acid uptake of Nafion®117. At low acid content, the additional acid has a significant effect on the water uptake. The membrane water content is $\lambda=17$ compared to $\lambda=20$ in pure water. However a plateau is observed at relatively low acid concentration up to 2M HBr. On the other hand, the acid uptake at room temperature appears to be linear; the acid molality in the membrane is roughly 2/3 of the acid molality in bulk solution. The acid content is calculated and plotted water in Fig 3.2. The acid content is expressed as the average number of HBr per sulfonate group. The relationship between water and acid uptake within the membrane is shown in Fig 3.3. The acid contents are calculated based on one equivalent weight, analogized from the calculation of water content λ.

The proton conductivity of Nafion®117 equilibrated in HBr is shown in Fig 3.4. The conductivity increases from 0.08-0.12 S/cm at low HBr concentration from 0-2 M, and decreases gradually with increasing HBr concentration from 2-9 M. This conductivity behavior can be explained by the water/HBr uptake data shown in Fig 3.2. At low acid concentration the water content in membrane is relatively stable and additional protons introduced into the polymer electrolyte can increase the proton conductivity. In contrast, at high acid concentration, the low water activity leads to a tremendous loss of water and proton mobility. Therefore, the conductivity presents a peak in Fig 3.4. Based on our results, the optimal HBr concentration condition is 2M.

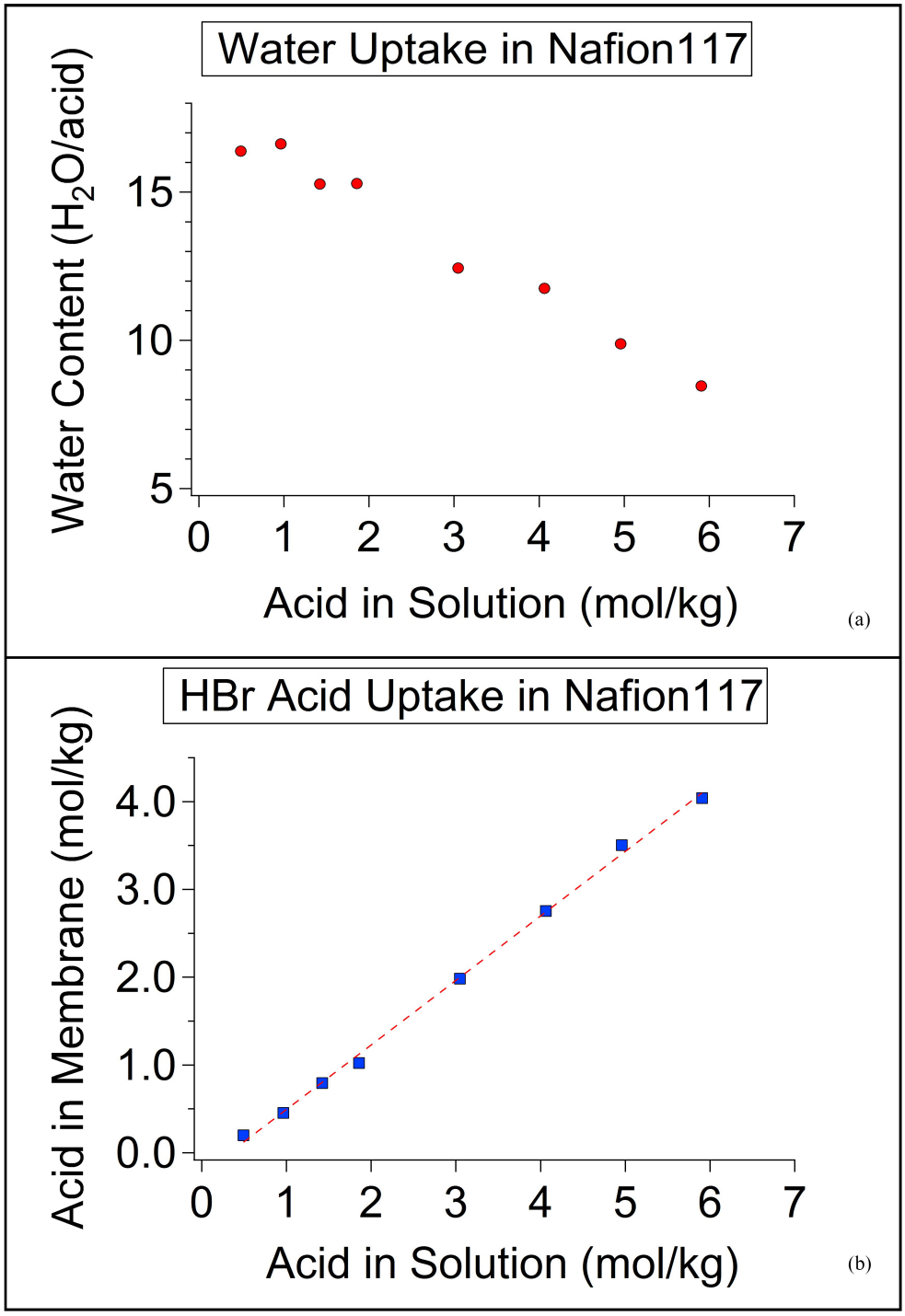


Figure 3.2 Water and Acid Content in Nafion®117 in HBr Aqueous Solution. (a) Water content vs. acid molality in bulk HBr solution (b) Acid molality in the membrane vs. acid molality in bulk HBr solution

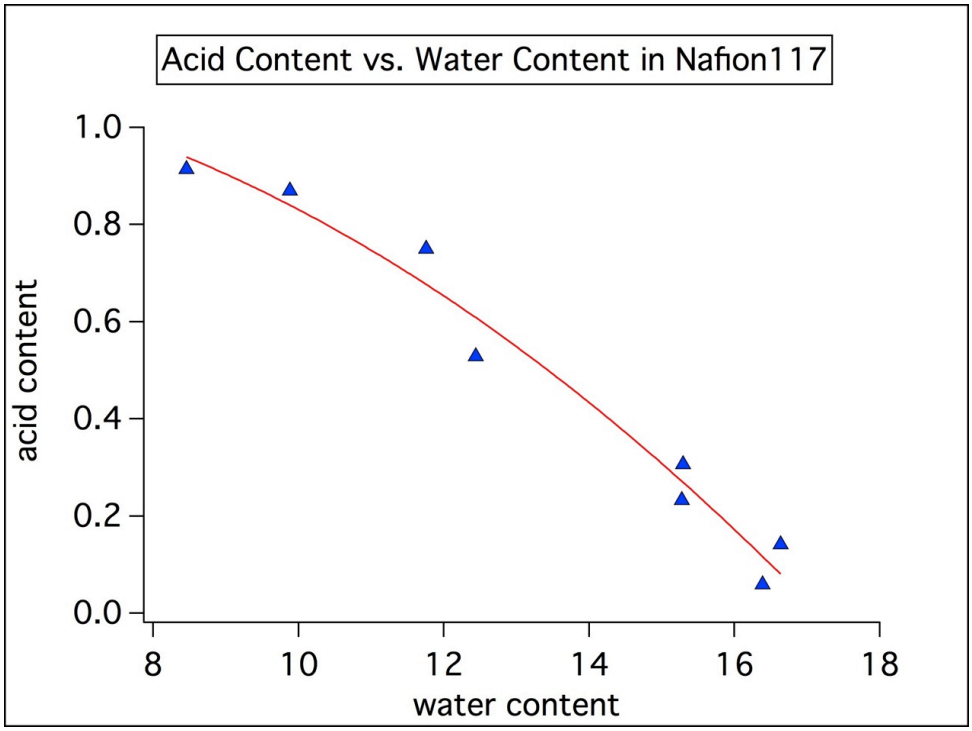


Figure 3.3 Acid Content vs. water content in the membrane

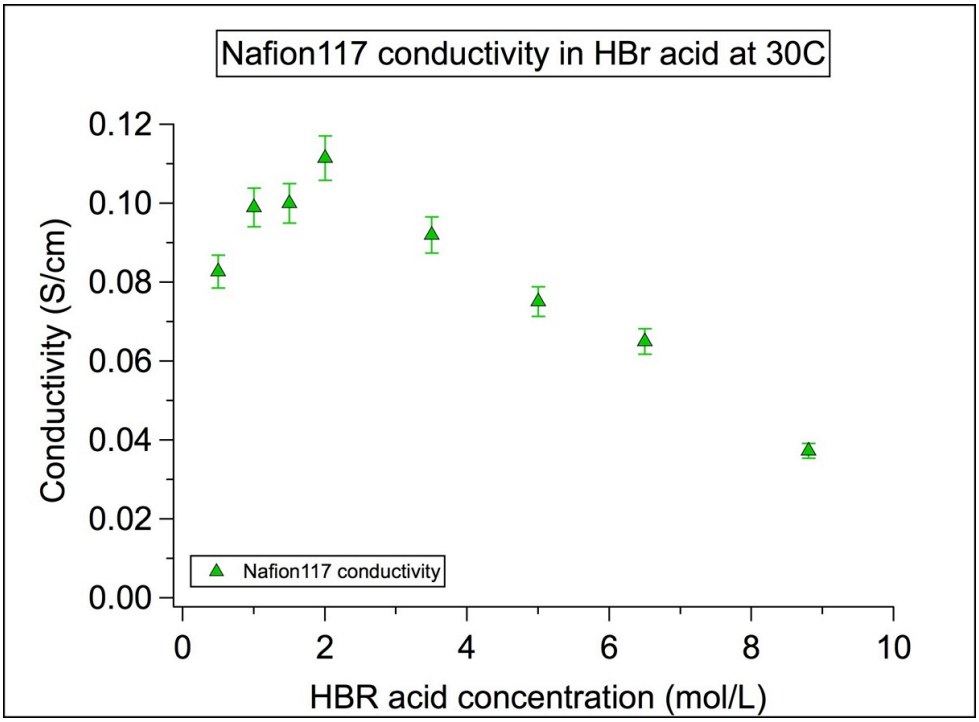


Figure 3.4 Nafion117 Conductivity in HBr Acid.Proton conductivity vs. HBr concentration in Nafion®117

3.3.2 Cell Performance

Different states of charge can be calculated from fully charged state (100% SoC). The standard potential of 1.087V was achieved with a state of charge of 67%. The analysis of polarization curves was emphasized to evaluate redox flow batteries by Aaron *et al*.[214] Here, a similar method was carried out to evaluate sources of losses from polarization curves at steady state. Each point was equilibrated by using a 30s to 90s step. The cell impedance was monitored throughout the polarization curves. We used polarization curves to frame our analysis of the performance of the hydrogen bromine redox flow batteries, as they help determine which processes dominate the overpotential at a particular current. Initially, we used a commercial MEA (Ion Power Co.) with a Nafion®212 membrane and 0.4 mg/cm^2 platinum loading on each electrode. On the positive electrode, a relatively low concentration of 0.3 M Br_2 in 1M HBr was used. The polarization curve for this MEA is shown in Fig 3.5. The linear region of polarization curve indicates the ohmic loss region. The beginning of the polarization curve shows that the kinetic loss of the experiment is small and the main part of this polarization curve stays in the linear ohmic loss region. The discharge limiting current density of 800 mA/cm^2 is generally believed due to the mass transfer. An iR-corrected polarization curve is plotted on top of the original polarization curve. The measured impedance is approximately 0.16 ohms cm^2 and slightly increases. Notice that the ohmic loss region in the polarization curve is only partially eliminated after IR correction. This implies the existance of extra ohmic resistance which is not corrected by the ASR. This might be due

to an ionic transport resistance within the electrode. More impedance experiments will be performed to further explain this effect.

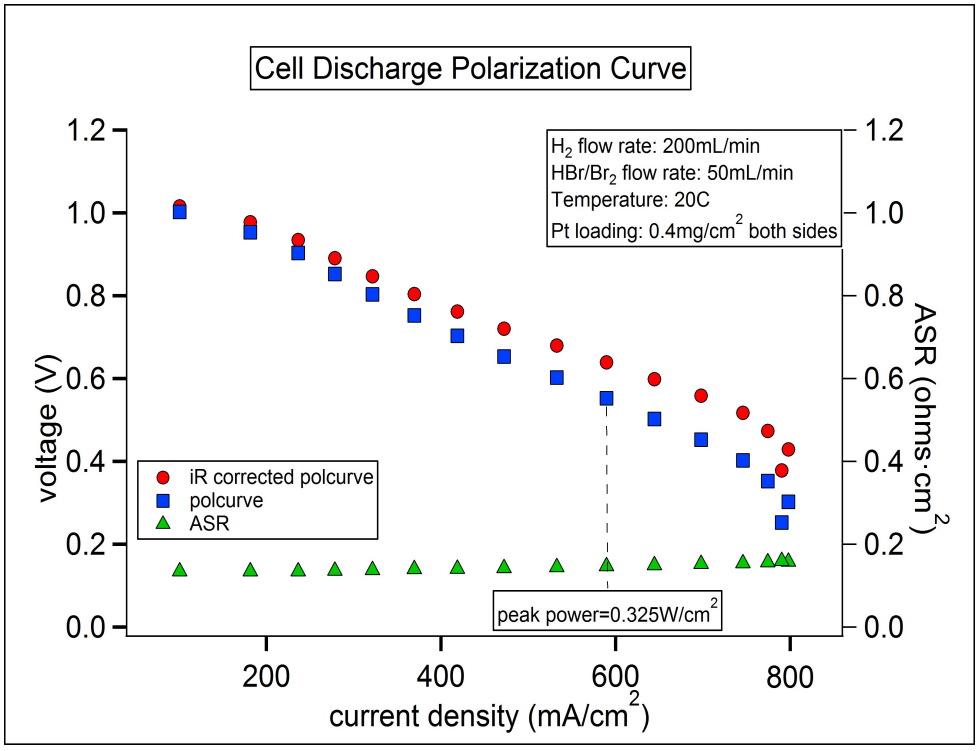


Figure 3.5 Commercial MEA Discharging Polarization CurveDischarge polarization curves with IR corrected data with a commerical MEA. Peak power density is 325 mW/cm^2 at current density 590 mA/cm^2.

As mentioned in Chapter 1, the poisoning effect of HBr and Br_2 on platinum was shown with cyclic voltammetry.[198] To improve the battery durability and performance, the removal of Pt from the cathode is needed. As reported in literatures, pure carbon paper electrode is feasible to conduct the redox reaction on the positive electrode without platinum coating.[213] A "half MEA" was prepared by hot-pressing Pt on negative side of Nafion®212. Pt loading was 0.3mg/cm^2 The positive electrolyte concentration was increased from 0.3M to 0.6M Br_2 in 1M HBr. The discharge polarization curve is shown in 3.6. It appears that the home-made half MEA could achieve a similar performance to the commercial MEA. Increasing electrolyte concentration could benefit the performance. However, the ASR of the half MEA cell is twice of the commercial MEA. The following experiments were all carried out with the same type of home-made half MEAs. ASR measurements in the following experiments confirm that the ASR of a half MEA is twice of a commercial full MEA. We conjecture that the extra resistance comes from the contact resistance between membrane and carbon paper without platinum on positive electrode.

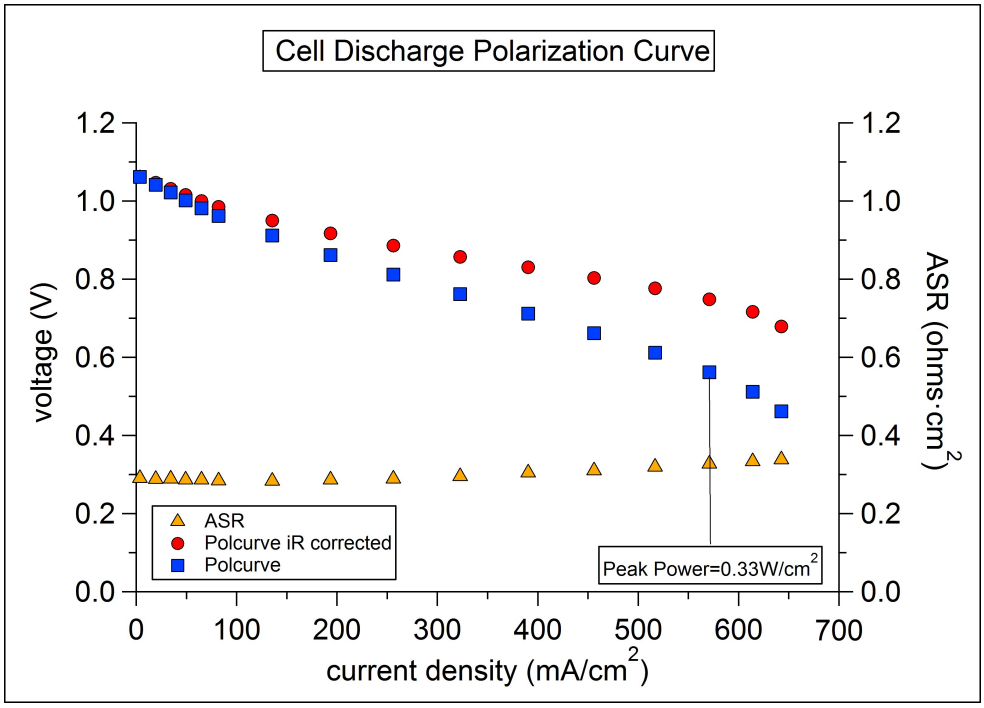


Figure 3.6 Discharging Polarization Curve with Increased Concentration

A temperature controller was applied to the system to investigate the temperature depandance. Cell polarization curves and ASRs at different temperatures are shown in Fig 3.7 (a,b). 0.9M Br in 1M HBr was used on positive electrode. A "half MEA" with Nafion®212 was assembled in the cell. One layer of carbon paper (SGL 10AA) electrode was applied on each side. When the temperature was increased from 20°C to 40°C, cell peak power density increased from 0.3 mW/cm^2 to 0.5 mW/cm^2. In Fig 3.7 (b), it shows that the IR corrected polarization curves do not overlap each other, which means that the improvement of performance is not just from an improvement in the ASR.

Fig 3.7 (a) shows that the ASR decreases from 0.25-0.2 $ohms \cdot cm^2$ with respect to increasing temperature. This suggests that the increasing temperature benefits the proton mobility in the membrane and improves the conductivity. Although the kinetic losses in the hydrogen bromine redox flow batteries are relatively small, here, an improvement in the kinetic region can still be observed. The increments in kinetic region indicate at elevated temperatures the activation energy can be lowered. In addition, in the mass transport region of the polarization curves, it shows that higher temperature can extend the mass transport limits, which can be explained as higher temperatures improves the ionic transport in the electrode. Hence, incrasing the temperature can improve the cell performance in all kinetic, ohmic and mass transport regions. However the uncompensated losses from the iR corrected polarization curves indicate that the possibility of other types of ohmic loss in that region.

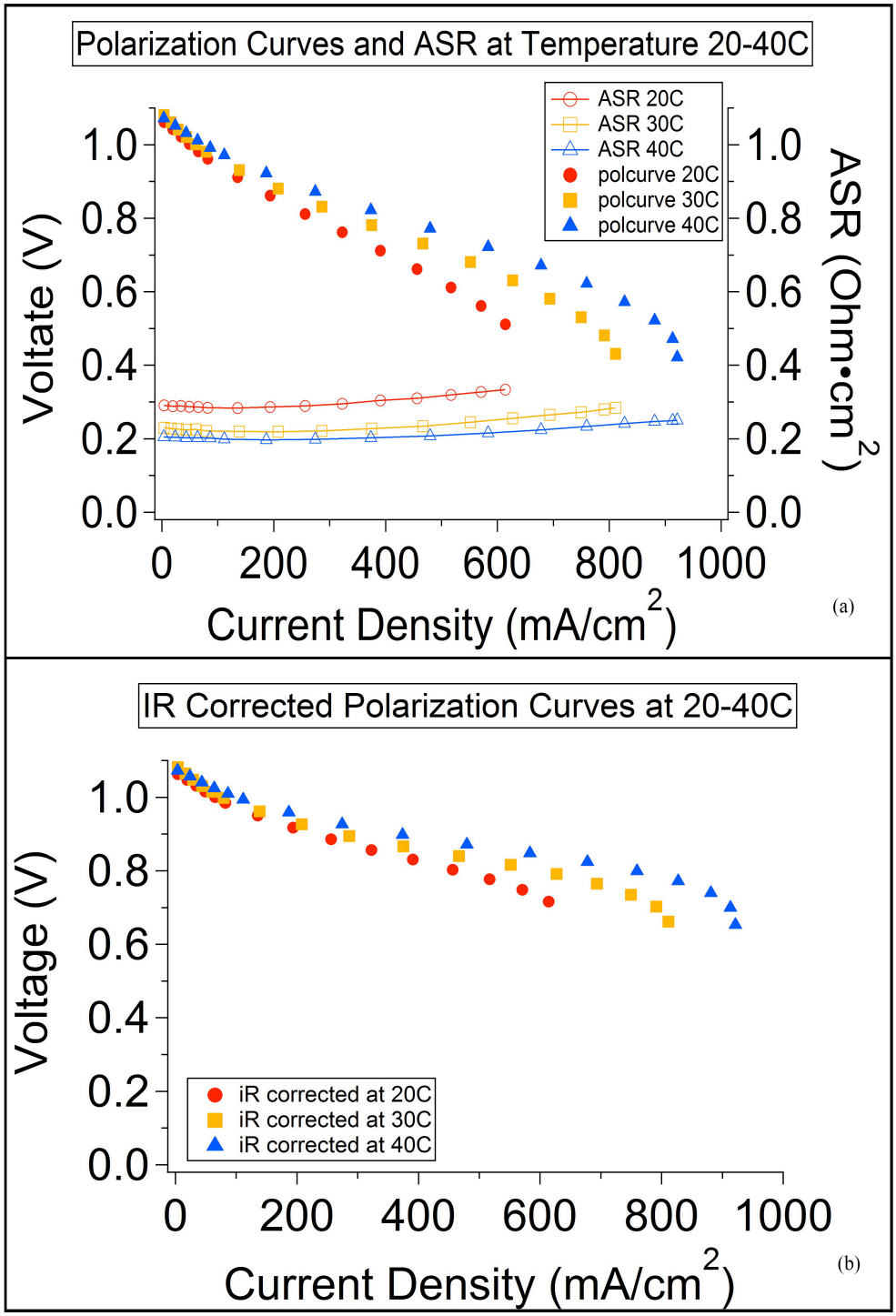


Figure 3.7 Temperature Dependence of Cell Performance.

Previous work on carbon electrodes in all-vanadium redox flow batteries showed that the cell performance could be improved by stacking carbon paper on the positive electrode.[217] This practice introduces a trade-off between cell kinetics and mass transport limitations arising from increasing the carbon paper electrode thickness. Fig 3.8 shows that stacking layers of carbon paper dramatically increased the ASR, from 0.2 to 0.5 ohms•cm^2. This leads to a decrease in peak power density from 0.5W/cm^2 to 0.25W/cm^2. However, cell performance is not solely determined by the ASR. Other aspects such as chemical kinetics and mass transport also impact the cell. The iR-corrected polarization curves show that the cell with 2 and 3 layers of carbon paper reaches a limiting current density at much lower current density due to a presumed mass transport issue. Conversely, these cells appear to have enhanced kinetics. It is possible that more carbon paper provides a large surface area to promote the reaction. Therefore, apart from the influence of temperature, a trade-off needs to be considered to manipulate carbon paper electrodes. Noticed, the performance with 2 layers of carbon paper is better than that with 3 layers of carbon paper, even in the kinetic region. The reason is that although the kinetics is related to the electrochemical surface area (ECSA), it is rather determined by the activation energy of the reaction on the electrode. Stacking carbon paper can increase the ECSA, but not effectively lower the reaction activation energy. Results show that a cell with 2 layers of carbon paper as the positive electrode is preferable, although we do notice an increased ASR. Limitations due to mass transport can be solved using higher flow rates or higher temperatures.

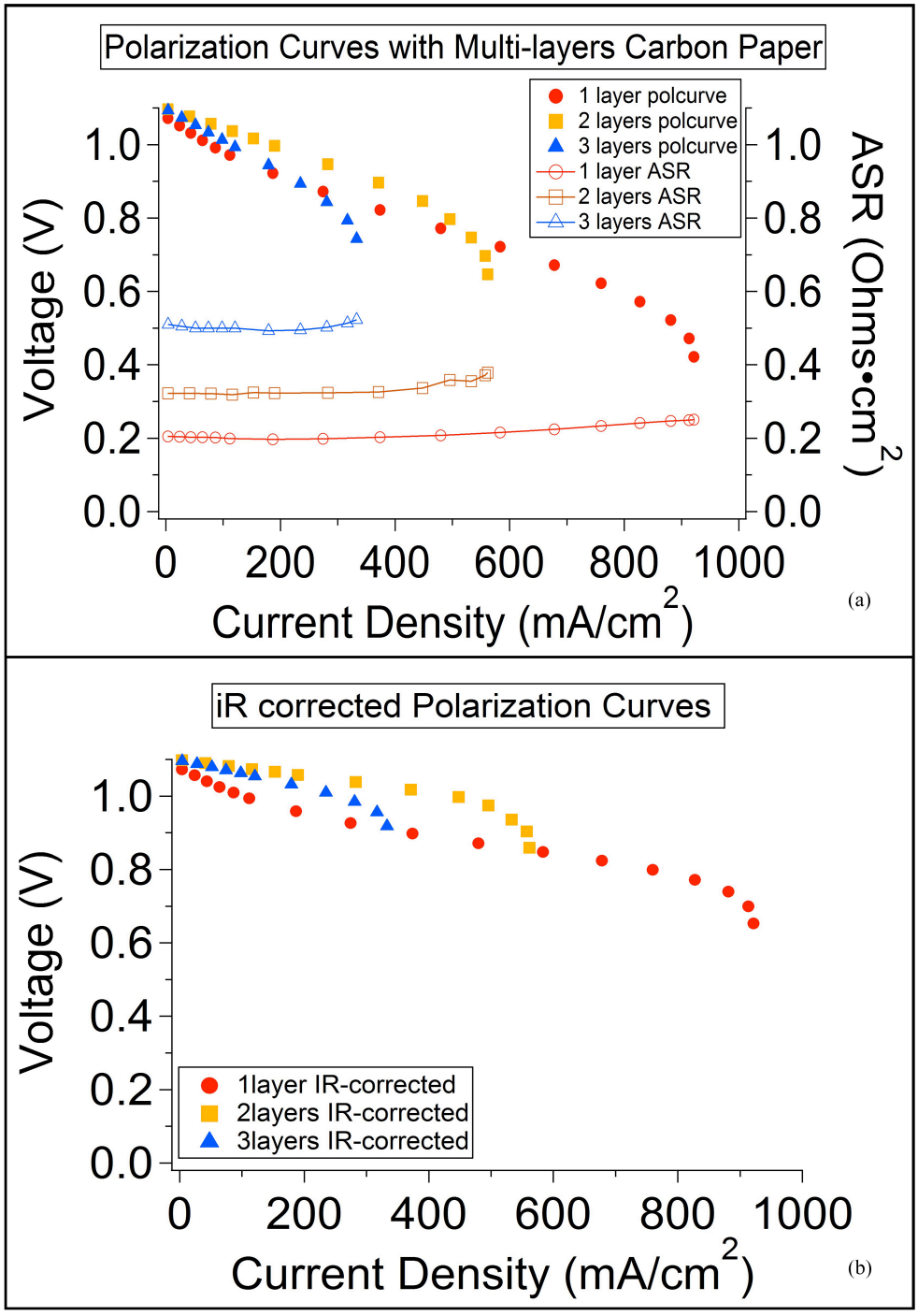


Figure 3.8 Polarization Curves with More Carbon Paper Layers.

Furthermore, alternative membrane was used in the hydrogen redox flow battery. Here, we used 3M ionomer (3Mion) perfluorosulfonate acid (PFSA) EW825. Platinum was hot-pressed on both sides of the membrane, and the cell configuration was the same as described before. The discharge polarization curve at 30 °C is shown in Fig 3.9 (a). The cell ASR is about 0.07 ohms•cm^2. This minor ASR can be a result from its thinner thickness (25 μm) compared to Nafion®212 (50 μm) and Nafion®117 (180 μm). Fig 3.9 (b) shows the discharge polarization curve at 50 °C. The kinetic and ohmic losses were improved slightly, and the mass transport was improved appreciably. The power density achieved 880 mW/cm^2 at 50 °C. However, no data from 3Mion PFSA EW825 with Pt only on one side is available at current stage. A small "hook" feature at the end of the polarization curve at 30 °C is observe, and this feature is not observed in the polarization curve at 50 °C. This feature will be elaborated in the following chapters. In general, the 3Mion shows a better performance compared with Nafion®212, however experiments using 3Mion with Pt only on negative electrode is required to further prove it.

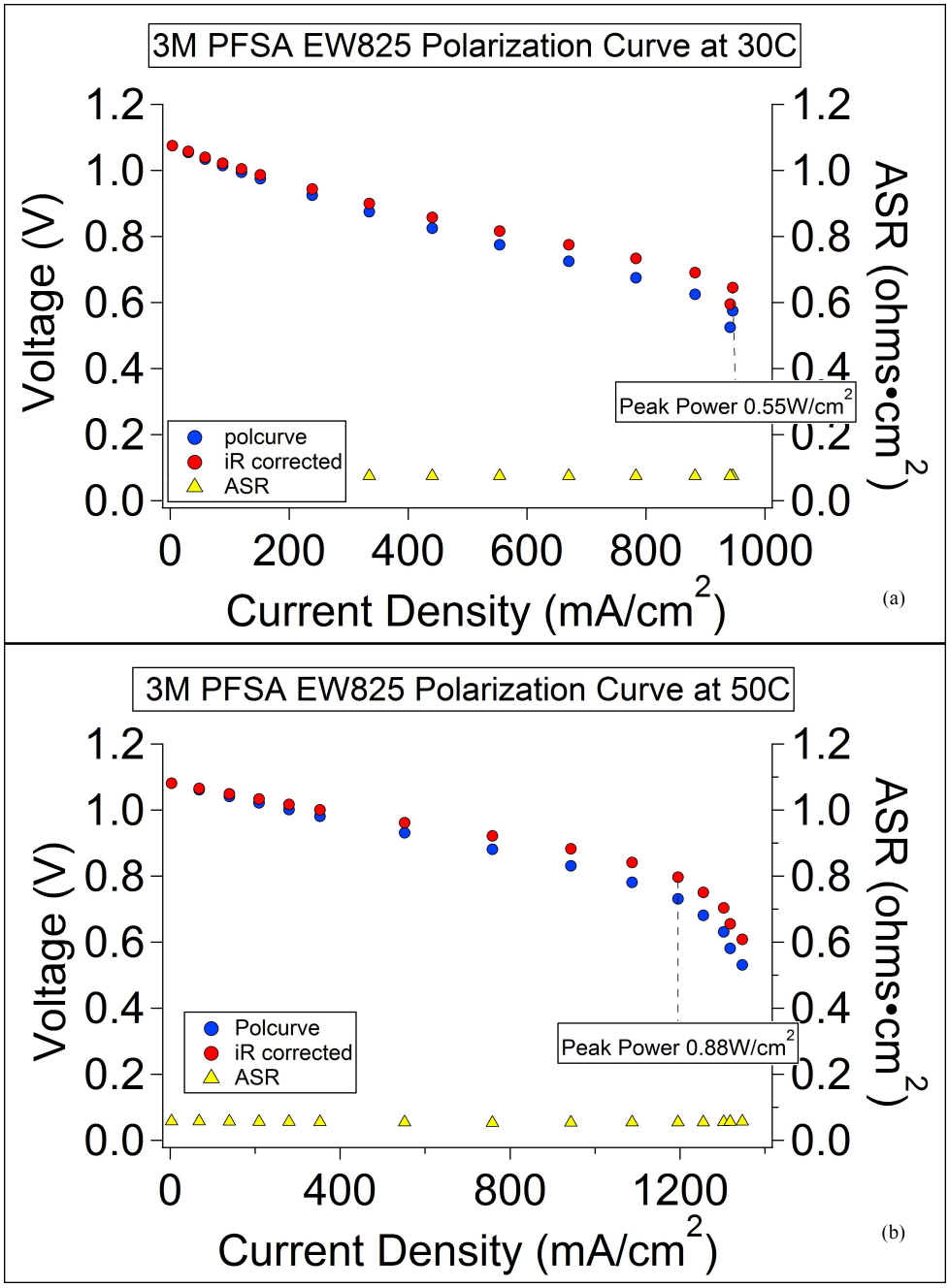


Figure 3.9 Polarization Curves with 3M PFSA (a) at 30 C; (b) at 50 C

A DHE reference electrode was assembled in the flow battery as described before. To minimize the possible poisoning effects, the DHE was assembled a few millimeters away from the active area and on the opposite side of the heat controller. The potential of the DHE was measured and calibrated with respect to the hydrogen electrode. A potential of 0V was determined, and this was held steadily which validated the feasibility of the DHE. The DHE was connected to a standard three-electrode potentiostat as the reference electrode. Modest charge and discharge cycling was carried out with current density from 0 to 250 mA/cm^2.

Fig 3.10 (a) shows the over potential vs. current density during charge and discharge on both electrodes. First, only minor kinetic losses are observed in charge and discharge polarization curves, which suggests the charging kinetics is also very fast. The polarization curves reach the linear ohmic loss region from the beginning for both electrodes. Meanwhile the overpotential of the whole cell comes from both negative and positive electrodes, with positive electrode slightly larger than negative electrode. Fig 3.10 (b) shows the iR-corrected over potential vs. current density during charge and discharge on both electrodes. Most of the overpotential was eliminated suggesting that membrane ASR dominates cell losses at modest charging and discharging current density. However, we can still observe a slope in the IR corrected data, which means there will still be a substantial ohmic loss at higher current density.

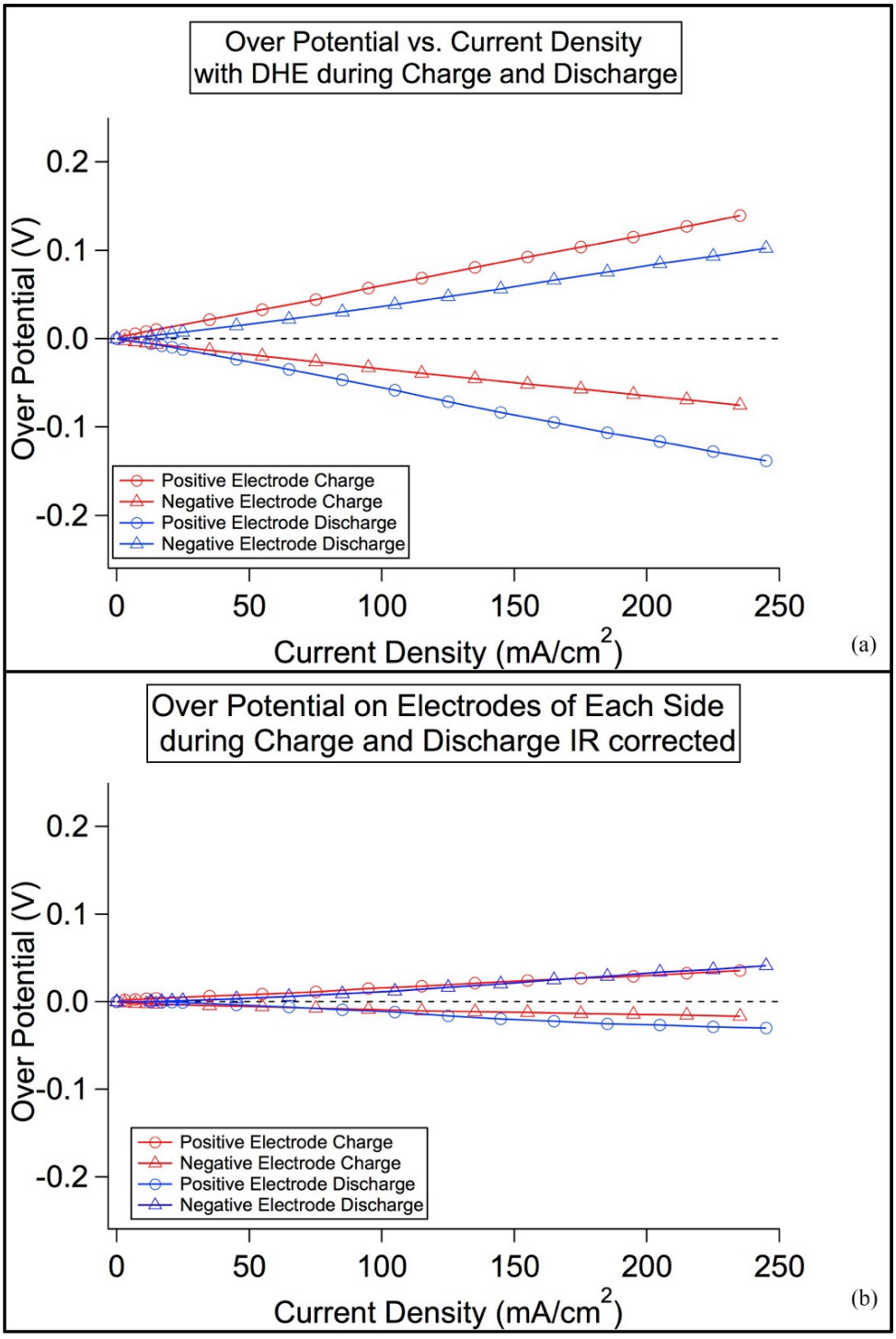


Figure 3.10 Discharge and Charge Polarization Curve with DHE.

3.4 Conclusion

Ex-situ studies of acid/water uptake and transport of HBr into the membrane show that the bulk acid concentration has a significant impact on membrane water/acid uptake, The proton conductivity measurement suggests that 2M hydrobromic acid is the optimal concentration. Polarization curve study shows that electrolyte concentration, cell temperature, electrode thickness, and types of membrane can affect the cell performance. Increasing the electrolyte concentration can improve the cell performance. Increasing the cell temperature can lower the kinetic and ASR losses and improve the cell performance in the hydrogen bromine redox flow battery. Stacking carbon paper can control the electrode thickness. However, increasing electrode thickness is a trade-off between the kinetics and the mass transport. The optimal thickness of electrode is 2 layers of carbon paper. The area specific resistance (ASR) has a significant impact on the performance of the hydrogen bromine redox flow battery during charge and discharge, especially at modest current density. A DHE reference electrode was assembled to independently study two electrodes and elucidate bromide/bromine electrochemical performance. It shows that negative and positive electrodes contribute comparable overpotentials to the whole cell, though the positive electrode added slightly more overpotential than the negative electrode.

Chapter 4

Kinetic Study of the Hydrogen Bromine Rodox Batteries

4.1 Introduction

In the preceding chapter we discussed the performance of the hydrogen bromine redox flow battery and introduced a dynamic hydrogen electrode (DHE) as a reference electrode in hydrogen bromine redox flow batteries. In this chapter, a more thorough study of the losses and issues we encountered in performance study will be discussed.

A variety of processes can contribute to performance limitations in RFBs. At the cell level, reaction kinetics, ionic transport through electrodes and the separator, electronic contact resistance, and mass transport resistance on electrodes are all expected to reduce the power available from a RFB. Polarization curve analysis has been used to aid in separating the above contributions to overpotential at varying operating currents.[214] It is quite important to assess the relative magnitude of these losses, particularly in the low current regime of high conversion efficiency. Generally, this region is kinetic limited. However, in the case of hydrogen bromine redox flow batteries, the kinetic loss is minimal as we discovered in the previous chapter. Nonetheless, it is important to explore these kinetic aspects as we begin to seek a non-precious catalyst that is not affected by bromine or bromide for the hydrogen electrode.

Inserting a reference electrode into the single cell allows electrode kinetics measurements to be performed in-situ by separating individual electrode contributions to the observed loss after iR correction. Here we report our implementation of a dynamic

hydrogen electrode (DHE) as a reference electrode for a study focused on the low-current region of the polarization curve to probe the kinetics of the positive and negative electrodes, respectively.

4.2 Experiment

4.2.1 Materials and Cell Configuration

0.6M Br_2 in 1M HBr was used as electrolyte on positive electrode. Humidified hydrogen was constantly flowing at the rate of 100 ml/min with temperatures controlled according to the cell operating temperatures. Battery testing was conducted using a 5 cm^2 single cell (Fuel Cell Technologies). The cell hardware consisted of aluminum end plates, gold-plated current collectors, and graphite blocks with a single serpentine flow field for electrolyte distribution. SGL 10AA carbon paper (400 μm) is used on the positive electrode and Toray PTFE-coated carbon paper (280 μm) is used on the negative electrode. Pt on carbon catalyst was hot-pressed on the negative electrode. To simulate a half MEA with Nafion®117 and DHE reference electrode, we sandwiched two Pt wires in between two pieces of Nafion®212. The membrane on the positive electrode was hot pressed with 6mg/cm^2 Pt (same procedures as described in last chapter). PTFE-coated fiberglass sheet (Fuel Cell Technologies) served as the incompressible cell gasket. The thickness of the gasket was chosen to fit 20% compression of the carbon paper.

4.2.2 Polarization Curves

Potentiostatic polarization curves were performed at a moderate charge/discharge current density, approximately from 0 to 400 mA/cm^2. To maintain the SoC, we applied alternating polarity overpotential on each electrode.[215] Each voltage step lasts for 30 s to reach the current steady state. The overpotential was controlled with respect to the stable open circuit potential prior to the beginning of the experiment. We obtained the same OCV before and after the experiment, which suggests that essentially the same SoC was sustained throughout the experiment. The current was sampled during the final 50% of each time step to exclude capacitive charging currents. The high frequency resistance (HFR) was measured using AC impedance at each potential step. The area specific resistance (ASR) on the positive side was 0.44 ohms•cm^2 and 0.25 ohms•cm^2 on the negative side. The whole cell ASR, measured from the positive to the negative electrode, was 0.7 ohms•cm^2, which also is the sum of each electrode resistance. These experiments were conducted under room temperature (about 20 °C, measured with a thermometer).

4.2.3 State of Charge

To study the battery state of charge (SoC), the hydrogen bromine redox flow battery was continuously discharged for 100 times; each time was a full discharge polarization curve. Thus, a series of discharge polarization curves were obtained at different SoC, and the SoC was calculated from the charge transferred during each polarization curve. First, the battery was charged at 1.2 V till fully charged. Each potential step was 20 sec, where the results showed that a steady state current was

reached. Therefore, the first polarization curve was started from 100% SoC, followed decreasing SoC each cycle. The high frequency resistance was monitored during the measurement to iR-corrected the results. VMP3 potentiostat with 20A booster channel were used.

4.2.4 Electrochemical Impedance Spectroscopy

Electrochemical measurements were performed using a VMP3 potentiostat with 20A booster channel (Bio-Logic Co.). Electrochemical impedance spectroscopy (EIS) was used to characterize the individual responses of the positive and the negative electrode to polarization. The electrode of interest was polarized for 1 minute to reach a steady state current. The DHE reference electrode response of the positive and the negative added up to the whole cell response, indicating the DHE reference electrode did not interfere with the impedance measurement.

4.3 Results and Discussion

4.3.1 Tafel Plot and Kinetics

The Tafel equation is an equation in electrochemical kinetics relating the rate of an electrochemical reaction to the overpotential. When an electrochemical reaction occurs in two "half reactions" on separate electrodes, the Tafel equation is applied to each electrode separately. The insertion of the DHE reference electrode allows us to separately study the properties of each electrode on a Tafel plot. The Tafel equation is applicable to

the region where the values of polarization are high. At low values of polarization, the dependence of current on polarization is usually linear instead of logarithmic:

$$i = i_0 \frac{nF}{RT} \Delta E \tag{25}$$

This linear region is called "polarization resistance" due to its formal similarity to Ohm's law. The exchange current is the current at equilibrium, i.e. the rate at which oxidized and reduced species transfer electrons with the electrode. In other words, the exchange current density is the flux of reaction at the reversible potential (when the overpotential is zero by definition). At the reversible potential, the reaction is in equilibrium meaning that the forward and reverse reactions progress at the same rates. This rate is the exchange current density. The Tafel slope or polarization resistance is measured experimentally allowing the exchange current density to be obtained from it. The exchange current density, j_0, is of particular interest since a higher j_0 indicates faster kinetics.

To eliminate the possible discrepancies from iR loss, the iR free Tafel plot is shown in Fig 4.1 plotted as overpotential versus log current density. The linear feature is observed at relatively high overpotenial above 20mV. The charge and discharge curves for both positive and negative electrodes are available. The Tafel slopes of each curve are obtained from linear fitting of the Tafel region. Using the equations below-which explicitly indicate the Tafel slopes, we can easily calculate the exchange currents for each

electrode except for the hydrogen electrode charging process, which we will discuss later in this chapter.

H-discharge: y=-0.19235+0.097741x;

Br-discharge: y=0.073314-0.04329x;

Br-charge: y=-0.12838+0.069083;

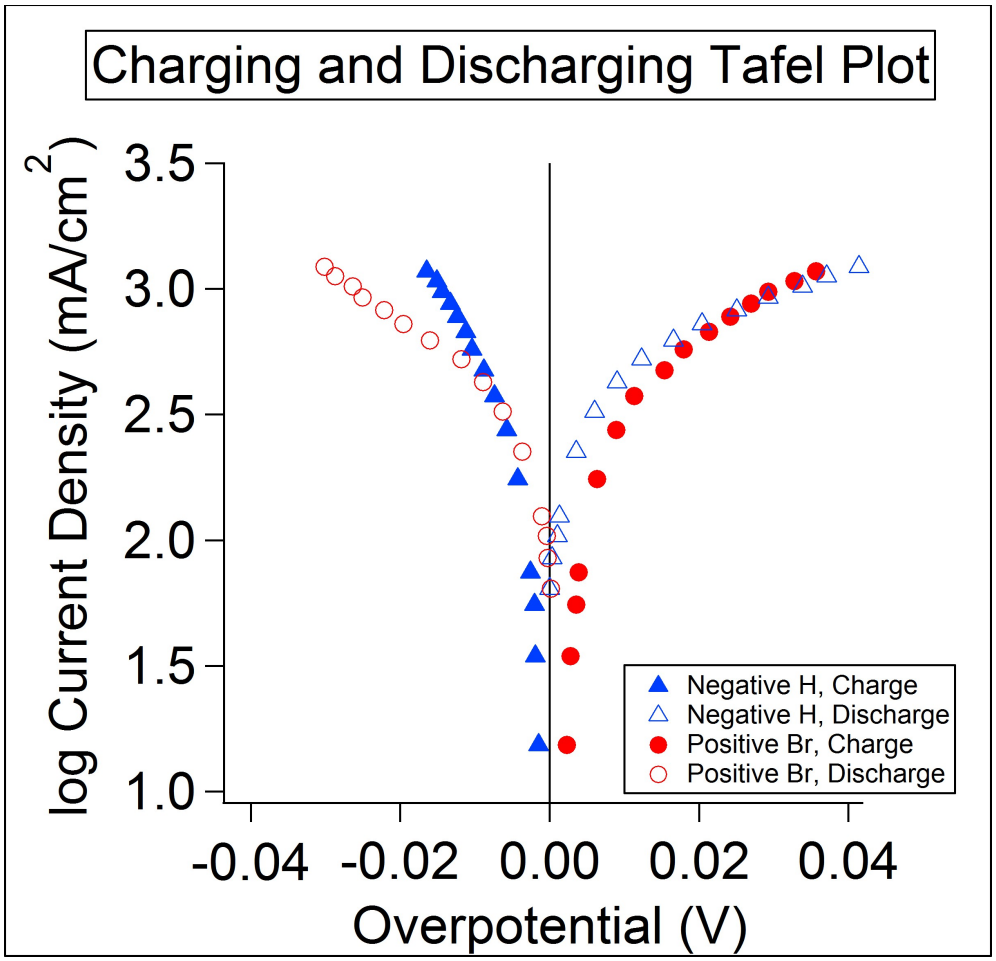


Figure 4.1 Charge and Discharge Tafel Plot for H/Br System. log i vs. over potential, iR free Tafel plot of Br on 10AA carbon paper positive electrode and H on Pt negative electrode, respectively.

The calculated bromine and hydrogen electrode exchange current data is shown in the Table 1. The Br electrode exchange current density was normalized with geometric area (5cm^2) of the cell and BET surface area. However, according to our ink preparation procedure, the Pt was covered by Nafion® ionomer. The BET measurement on the hydrogen electrode is affected by this. Thus, the hydrogen electrode was normalized with geometric area (5cm^2) of the cell and the electrochemical surface area (ECSA). This measurement was conducted in a newly assembled cell to avoid ECSA loss due to the bromine contamination. Table 1 shows the exchange current density of both electrodes. Both charge and discharge exchange current densities are listed in the table. The SoC was controlled at 70% and the cell temperature was 20 °C. We noticed that the positive electrode and negative electrode have the same magnitude of exchange current densities during both charge and discharge. It shows that under both charge and discharge circumstances, bromine on carbon paper exchange current density is approximately 60% that of H_2 on Pt. This fast kinetics allows us to remove the Pt on bromine side of the battery. Therefore, this result is consistent with the minor kinetic losses we observed in the polarization curves.

The hydrogen electrode charging process did not exhibit a linear feature in the Tafel plot. We assumed that the hydrogen negative electrode is not polarized sufficiently to reach the linear Tafel region. As we mentioned previously, at low values of polarization, the dependence of current on polarization is usually linear instead of logarithmic. Under this circumstance, we estimate the exchange current j_0 from the linearized Butler-Volmer expression, shown in equation (25). Fig 4.2 shows a plot of

overpotential against current density to yield a slope directly proportional to j_0 at minimal overpotential. A linear fitting of the curve is applied to calculate j_0. In equation (25), n=2; F is the Faraday constant; R is the gas constant; T is 20°C. Thus, j_0 could be easily calculated according to equation (25).

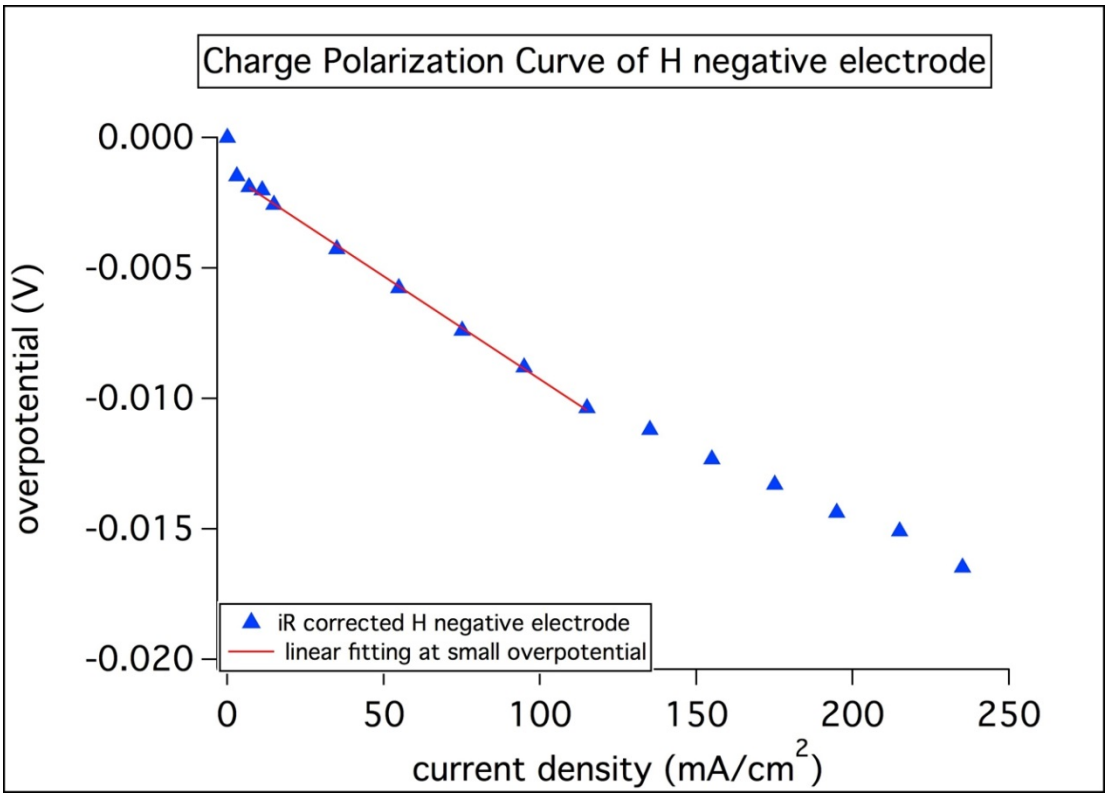


Figure 4.2 Curve Fitting with 1st order Butler-Volmer Equation.

Table 1 Exchange Current of H_2 on Pt and Bromine on Carbon Paper

	Tafel Slope	j_0, mA/cm^2 (geometric normalized)	j_0, mA/cm^2 (BET/ECSA normalized)
H-dicharge	98 mV/decade	92.9	0.546
H-charge	35 mV/decade	129.54	0.788
Br-discharge	43 mV/decade	49.43	0.291
Br-charge	69mV/decade	72.11	0.424

4.3.2 State of Charge

Measurements were performed at room temperature (20°C) monitored by thermocouple. The electrolyte SoC was calculated from the amount of charge of electron transfer, using the following equation:

$$SOC = \frac{2[Br_2]}{[HBr] + 2[Br_2]} \tag{23}$$

$$Q = nNF \tag{24}$$

Where, n=2, Q is the electron charge transferred, F is the Faraday constant, N is the moles of Br_2 reacted. Calculated results showed that the SoC changed less than 1%, and we assume the SoC remained stable during one cycle. A constant flow rate of 40 mL/min was maintained on the bromine positive electrode with a peristaltic pump (Cole-Palmer). To illustrate the ratio of the practical flow rate to the actual electrolyte-consumption rate, the stoichiometric flow rate is calculated by equation (24). The charge Q was obtained by integrating current over time, thus the moles of electrolyte consumed could be calculated. Compared to the operating flow rate the, the stoichiometric flow rate is approximately 50, which means the cell operating flow rate is 50 times as much as the actual electrolyte-consuming rate on the electrodes. Hydrogen flow was controlled at 100mL/min constantly to keep H negative electrode at hydrogen potential.

Fig 4.3 shows a polarization curve for a hydrogen bromine redox flow battery. Similar to the polarization curves for vanadium redox flow batteries reported by Aaron *et al.*[218], the polarization curve of hydrogen bromine redox flow battery consists of two

parts: a linear ohmic loss region and a mass transport limiting region. However, instead of reaching a limiting current at high over potential, the polarization curve presents a "hook". This feature is different from a typical mass transport limit where the voltage decreases monotonically or straight down at the limiting current. A similar feature was also observed in the vanadium flow batteries tested in our lab. With all-vanadium redox flow batteries, the SoC was calculated as described before. Results show that during extended discharge the SoC of all-vanadium battery decreases tremendously and the reason for the "hook" is the electrolyte (V^{2+}/V^{3+} or V^{4+}/V^{5+}) deficiency. For a single measurement, the problem could be solved by using a single pass flow mode to maintain the electrolyte concentration i.e. the SoC. For cycling the battery, some alternative charging or discharging procedures could be used to maintain the electrolyte concentration i.e. SoC. In sum, for vanadium redox flow battery, the mass transport limitation "hook" was eliminated by maintaining the SoC of anolyte and catholyte.

A similar approach was applied to investigate this issue in the hydrogen bromine redox flow battery. We implemented a study of cell discharge features with SoC dependence. By continuously discharging the battery with chronoamperomety, we obtain a series of discharge polarization curves at different SoCs. To ensure the discharge current reaches steady state, each step was applied for 30 s. As described before, each a series of full discharge polarization curves were carried out, and this procedure ran up to a hundred times. The OCV was measured before and after each discharge polarization curve. The calculation shows that the SoC changes less than 1% within one full discharge measurement. As we monitoring the SoC over 100 cycles, it changes from 100% to 85%.

Thus, the relative SoC and OCV changes are 15% and 10%, respectively. Fig 4.4 shows the state of charge and OCV change during cycling. This experiment indicates that, unlike vanadium redox flow batteries, the electrolyte deficiency is not the reason for the anomalous features in hydrogen bromine redox flow battery polarization curve during the measurement.

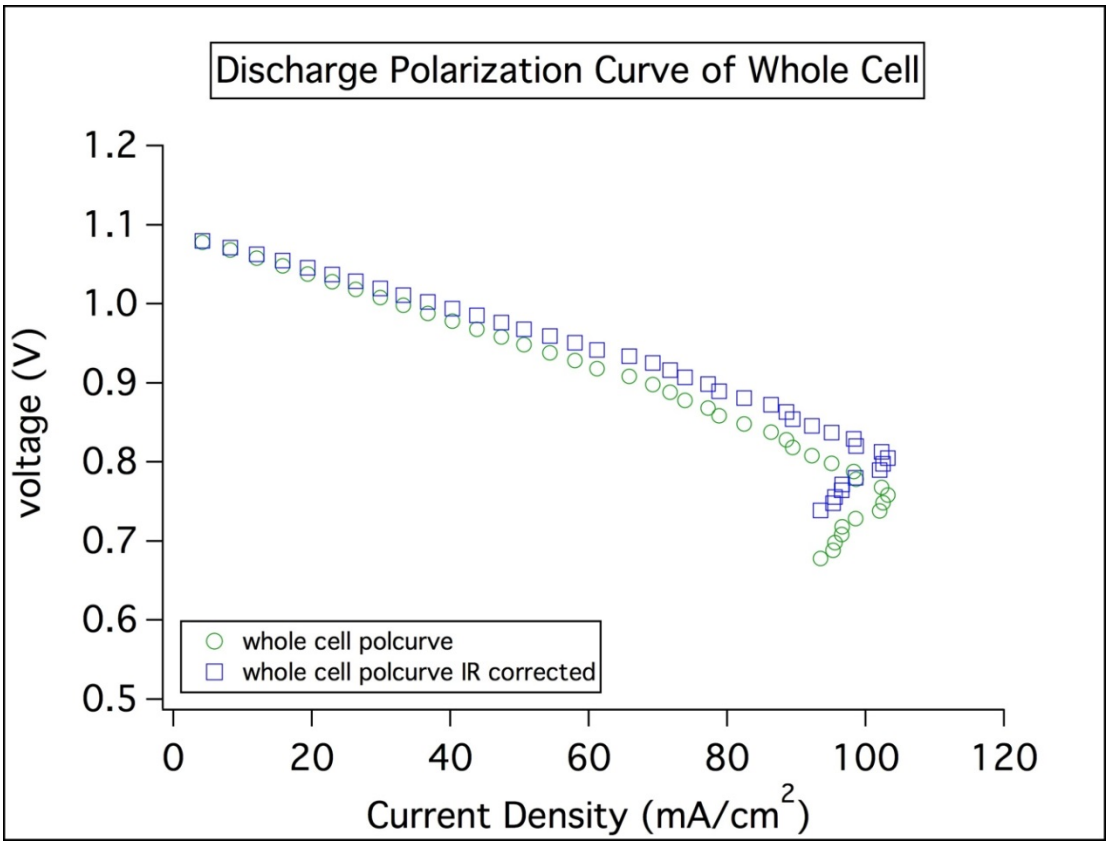


Figure 4.3 Discharging Polarization Curve of the Whole Cell.The discharge polarization curve with and without iR-correction.

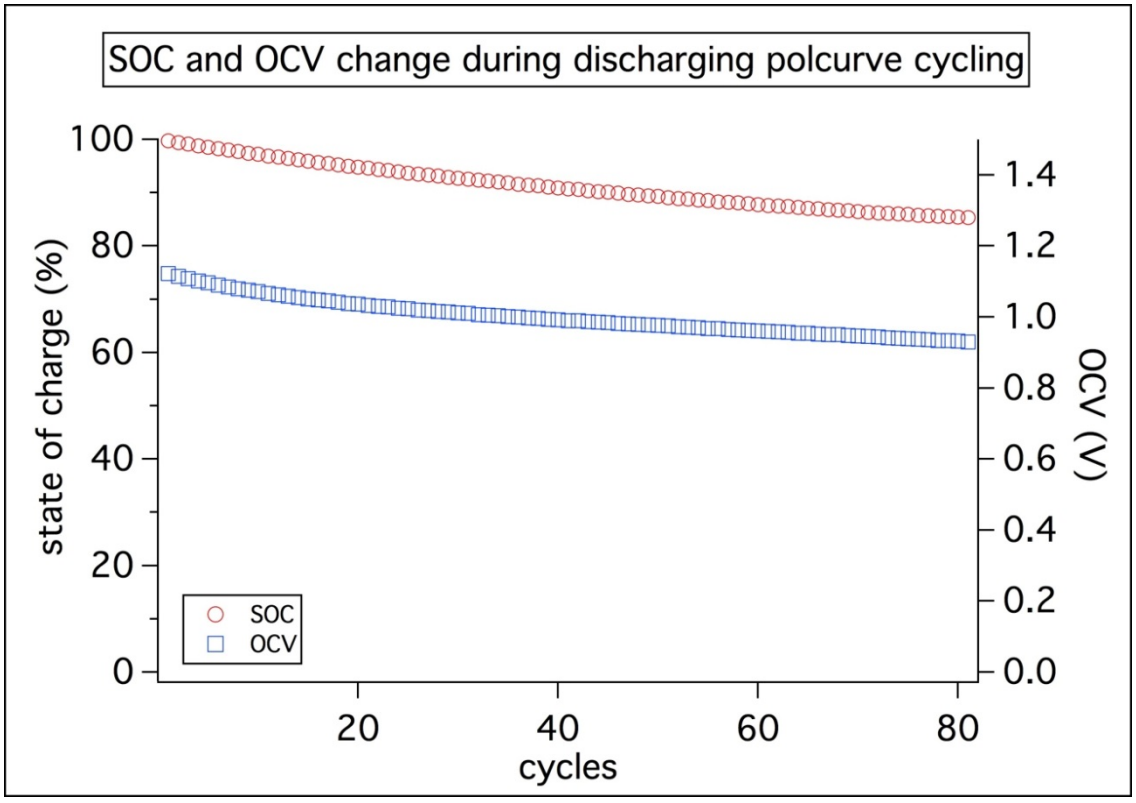


Figure 4.4 SoC and OCV Change during Discharging Cycling.

Interestingly, shown in Fig 4.5, only the polarization curves at relatively high SoC exhibit the current turnover point. We also record the turnover potential in for each discharging polarization curve in Table 2. It shows that, at high SoC, the turnover point started to appear even at small overoptentials. As we deplete the electrolytes, i.e. at low SoC, the turnover potential started to appear at higher overpotentials, i.e. the electrodes could get more polarized. The "hook" in the mass transport region became smaller and smaller and eventually disappeared. At 85% Soc, the potential of the discharge polarization curve could go down to 0.6V without observing the "hook". The power density of the cell is shown as in Fig 4.6. Although the power density appears the same "hook" feature, the higher SoC tends to lead to a better performance.

The overpotential at the turnover point was calculated by subtracting the turnover potential from the relevant OCV. Results are plotted in Fig 4.7. It appears that the overpotential at the turnover point maintains at the same level during the course of discharging, i.e. at all SoCs. In another word, at approximately 0.37V overpotential, the current density of the cell starts to decrease significantly at any SoC. This phenomenon might suggest that at high Br_2 concentration: (1) the Br_2 has slower mass transport in carbon paper electrode, leading to a local electrolyte deficiency; or (2) Br_2 could be adsorbed on the carbon electrode and block further reactions; or (3) the crossover of Br_2/Br^- to the H/Pt electrode and block the main active sites on Pt; or (4) bromine could be stagnated in polymer electrolyte channels and compromise the cell performance; or (5) at 0.37 V, the bromide adsorption on Pt occurs, and therefore blocks the active sites for the hydrogen adsorption.

The ASR should be significantly increased if the bromine is stagnated in the polymer and hinder the proton transport. From the polarization curves and ASR measurements in previous chapter, we showed that the ASR (with slightly increase) was generally consistent during the discharge polarization curve. This suggests that the hypothesis (4) is not the reason for the "hook" feature, however possibly results in the slight increment in the ASR.

Fig 4.7 shows that the hook happens at the same overpotential with different SoC. This suggests the possibility of side reactions at certain potentials. The standard reaction potentials of bromide related reactions are shown below:

$Br_2(l) + 2e^- = 2Br^-$ $E_0 = 1.066V$ (Br_2 is not in aqueous) (25)

$BrO^- + H_2O + 2e^- = Br^- + 2OH^-$ $E_0 = 0.761V$ (26)

$BrO_3^- + 3H_2O + 6e^- = Br^- + 6OH^-$ $E_0 = 0.61V$ (27)

The turnover potential in cycling is between 0.8V and 0.6V. Thus the formation of BrO^- and BrO_3^- could occur at higher potential. Presumably, the BrO^- and BrO_3^- could cross the membrane and accumulate at the Pt surface on negative electrode. Therefore reaction (26) or (27) happens at 0.76 V or 0.61 V and produces Br^-, which could highly affect the surface area of Pt and harm the negative electrode performance. Furthermore, an *in-situ* cyclic voltammetry for hydrogen on Pt was measured in present of bromide solution on the positive electrode. Fig 4.8 shows that the hydrogen adsorption peaks are diminished severely, and the hydrogen redox reaction was significantly hindered. A few

peaks are observed while scanning from 0.7 to 0.6 V. This may be a sign for the side reaction of BrO^- and BrO_3^-. A thorough investigation of the other hypotheses will be discussed in Chapter 5.

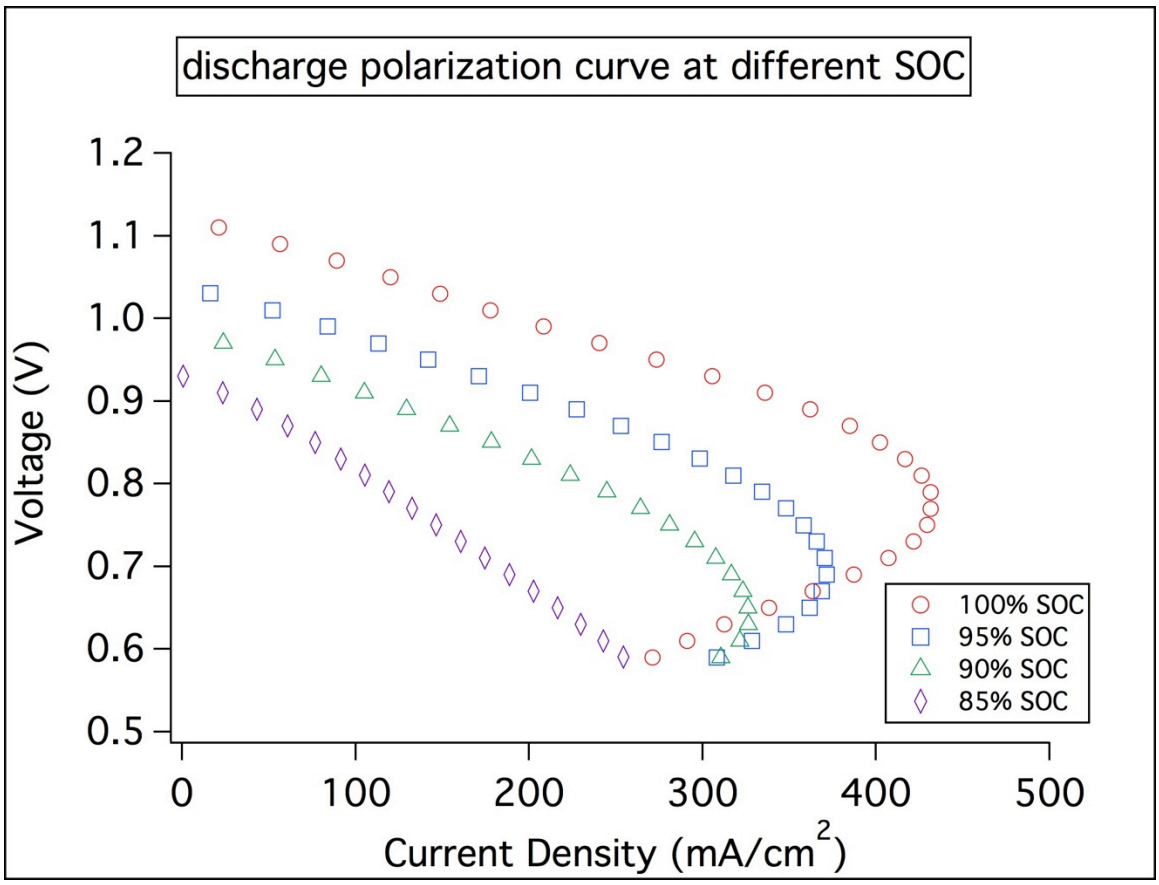


Figure 4.5 Discharge Polarization Curve at Different SoC.It shows some typical hydrogen bromine redox flow battery polarization curves.

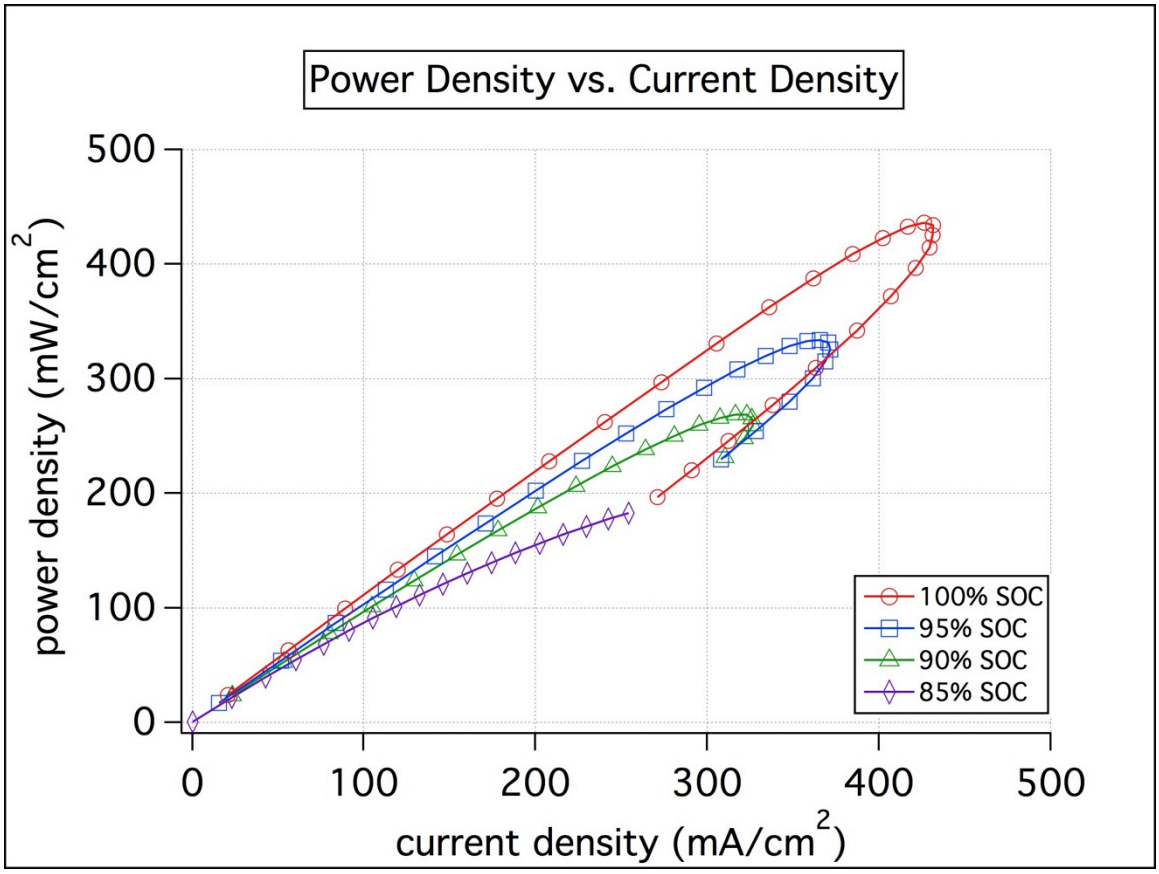


Figure 4.6 Power Density at Different SoC.Due to the turnover current density the power density appears the same feature with a turnover potential.

Table 2 State of Charge and Turnover Potential during Cycling

Cycle #	SoC	Turnover potential
1	99.7%	0.75
2	99.4%	0.77
3	99.1%	0.77
4	98.8%	0.75
5	98.5%	0.75
6	98.3%	0.75
7	98.0%	0.73
8	97.7%	0.73
9	97.4%	0.73
10	97.2%	0.73
11	96.9%	0.73
12	96.7%	0.71
13	96.4%	0.71
14	96.2%	0.71
15	95.9%	0.69
16	95.7%	0.69
17	95.5%	0.69
18	95.2%	0.69
19	95.0%	0.69

Table 2 (continued)

Cycle #	SoC	Turnover potential
20	94.8%	0.69
21	94.6%	0.69
22	94.4%	0.69
23	94.2%	0.67
24	93.9%	0.67
25	93.7%	0.67
26	93.5%	0.67
27	93.3%	0.67
28	93.1%	0.67
29	92.9%	0.67
30	92.7%	0.67
31	92.5%	0.65
32	92.4%	0.65
33	92.2%	0.65
34	92.0%	0.65
35	91.8%	0.65
36	91.6%	0.65
37	91.4%	0.65
38	91.3%	0.65
39	91.1%	0.65

Table 2 (continued)

Cycle #	SoC	Turnover potential
40	90.9%	0.63
41	90.7%	0.63
42	90.6%	0.63
43	90.4%	0.63
44	90.2%	0.63
45	90.1%	0.63
46	89.9%	0.63
47	89.7%	0.63
48	89.6%	0.63
49	89.4%	0.63
50	89.3%	0.61
51	89.1%	0.61
52	88.9%	0.61
53	88.8%	0.61
54	88.6%	0.61
55	88.5%	0.61
56	88.3%	0.61
57	88.2%	0.61
58	88.1%	0.61
59	87.9%	0.61

Table 2 (continued)

Cycle #	SoC	Turnover potential
60	87.8%	0.61
61	87.6%	0.59
62	87.5%	0.59
63	87.4%	0.59
64	87.2%	0.59
65	87.1%	-
66	87.0%	-
67	86.8%	-
68	86.7%	-
69	86.6%	-
70	86.5%	-
71	86.3%	-
72	86.2%	-
73	86.1%	-
74	86.0%	-
75	85.9%	-
76	85.8%	-
77	85.7%	-
78	85.6%	-
79	85.5%	-

Table 2 (continued)

Cycle #	SoC	Turnover potential
80	85.4%	-

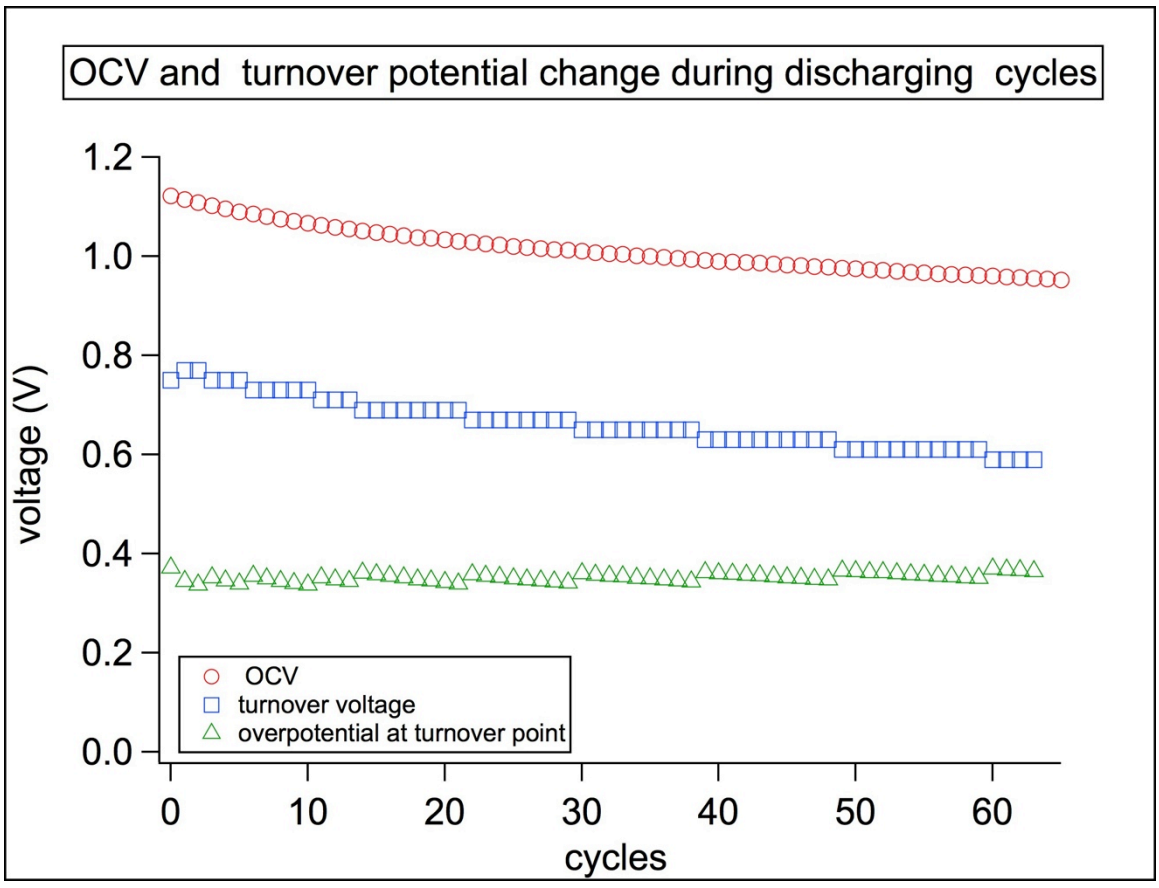


Figure 4.7 The Change of Turnover Potential during Cycling.The overpotential of the turnover potential was calculated from by subtracting the potential from the OCV. The results are shown in the triangles, which are relatively stable through in various SoC range.

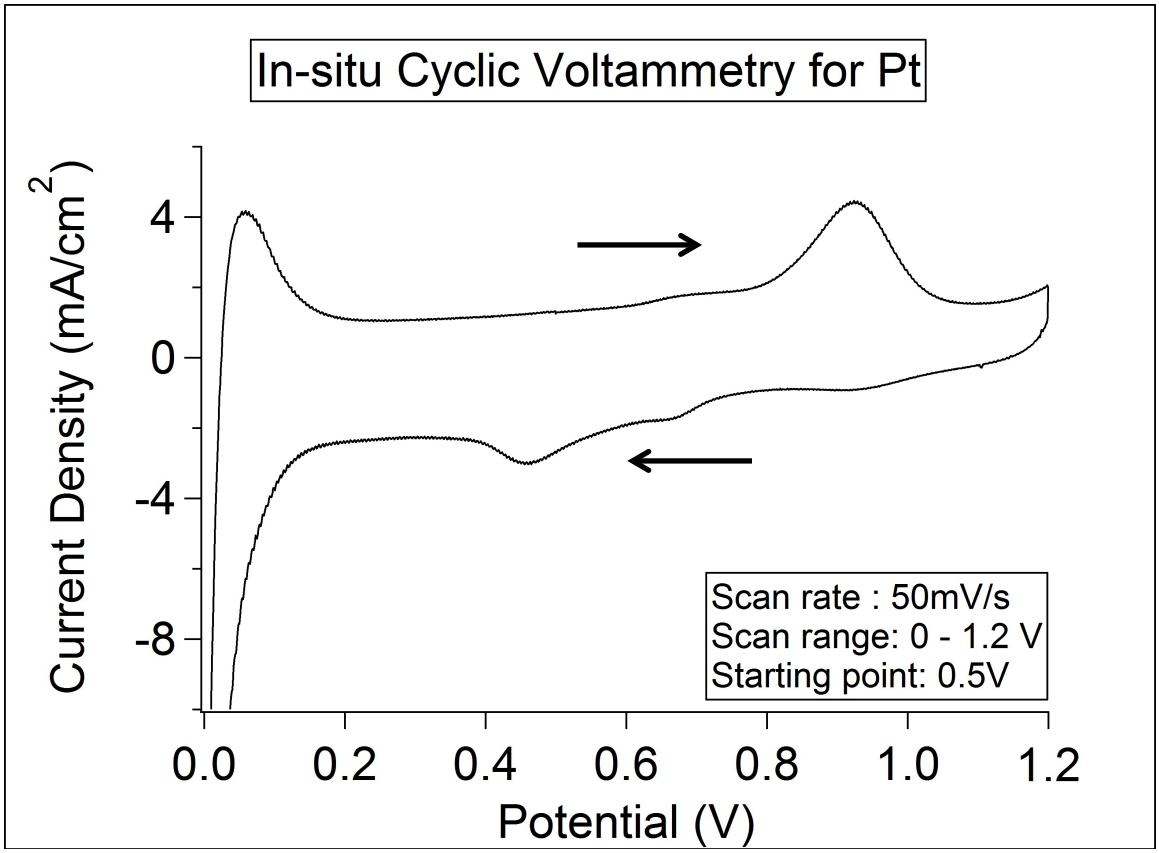


Figure 4.8 In-situ Cyclic Voltammetry for hydrogen on Pt

4.4 Conclusion

The insertion of a DHE reference electrode allows us to separately study the properties on a Tafel plot. The exchange current of charging and discharging on both H and Br electrode were calculated from the Tafel plot. It shows that bromine on carbon paper is approximately 60% that of H_2 on Pt under both charging and discharging circumstances. This fast kinetics allows the removal of Pt on bromine side of the battery. The performance issues of hydrogen bromine redox flow battery were further discussed in this chapter. A "hook" at the end of the polarization curve is observed. The turnover point starts to occur at relatively small overpotential. As the electrolytes are depleted, the electrode becomes more polarized and the "hook" gets smaller and eventually disappears. At 85% SoC, the potential of the discharge polarization curve decreases to 0.6V without observing the "hook". The power density curves show that higher SoC leads to a better performance. The overpotential at the turnover point, where the current density of the cell starts to decrease significantly, is calculated, which appears relatively stable at 0.37V. This phenomenon suggests the possibility of side reactions or adsorption process at certain potentials related to bromide. It is suspected that at high Br_2 concentration: (1) the Br_2 has slower mass transport in carbon paper electrode and lead to a local electrolyte deficiency; or (2) Br_2 could be adsorbed on the carbon electrode and block further reactions; or (3) due to the side reactions, BrO^- and BrO_3^- are formed at certain potentials; or (4) at 0.37 V, the bromide/bromine adsorption on Pt occurs, and therefore blocks the active sites for the hydrogen adsorption. A further study of these hypotheses will be discussed in next chapter.

Chapter 5

Electrochemical Impedance Spectroscopy (EIS) Study of Hydrogen Bromine Redox Flow Battery

5.1 Introduction

In Chapter 4, we have proposed 4 hypotheses that lead to the anomalous features in the polarization curves. Further study on cell performance with electrochemical impedance spectroscopy (EIS) will be discussed in this chapter. The polarization curve consists of three parts: kinetic, ohmic and mass transport. Compared with all-vanadium redox flow batteries, the kinetic loss of hydrogen bromine redox flow batteries is minor. Based on many of the polarization curves from last two chapters, the ohmic loss dominates the polarization curves before the mass transport limit. The polarization curve reaches the ambiguous mass transport limit, a "hook" as we described before.

One key route to cost reduction is an increase of cell current density at the desired operating voltage, permitting decreased cell and/or stack size. In previous work [214], a "zero-gap" cell configuration was demonstrated to achieve a greatly improved power density, in part due to large reductions in the ohmic resistance of the cell. However, iR-corrected data showed that the iR losses from the membrane could not fully compensate for all apparent ohmic losses. The overpotential that dominates the ohmic loss region remains substantial. Though DHE study shows that the ohmic losses in the "zero-gap" cell configuration are largely governed by the membrane (MEA), the remaining overpotentials, broadly comprising charge transfer kinetics and mass transport, originate

in electrode processes. These processes can be separated at the cell level with single-electrode methods through the use of a reference electrode.

In the previous two chapters we discussed the performance and potential losses based on polarization curves. In addition, the Tafel plot and kinetic study shows that the hydrogen electrode and bromine electrode have the same order of magnitude of exchange current density. The hydrogen electrode exchange current density is approximately two times that of the bromine electrode. To investigate the mechanism of the loss, we applied electrochemical impedance spectroscopy method using a dynamic hydrogen reference electrode (DHE). The two electrodes are thus separately investigated.

Electrochemical Impedance Spectroscopy (EIS) could be used to separate and analyze the overpotential loss from each part of a polarization curve. At high frequency, the intercept of the semicircle and the real axis indicates the high frequency resistance, iR loss, which presumably comes from the membrane and contact resistances. In some cases, due to the porous structure of electrode, a linear porous response could occur at the very beginning of an EIS plot in high frequency region. The electrode porosity, pore shape and tortuosity highly influence this feature,[219,220] introducing in much complexity in the high frequency region. The diameter of an arc in different frequency regions represents different sources of “resistance”. In the case of charge transfer, the semicircle results from the charge transfer resistance in parallel with a double layer capacitance, which can be determined by fitting to the corresponding equivalent circuit. In practice, due to the roughness of the electrode surface, the capacitance is usually not ideal and is called a constant phase element instead. A parameter p is introduced to correct the double layer

capacitance.[221] In addition, device impedance and induction features could also appear in the EIS plot. Therefore, the over potential is specifically analyzed in more detail using EIS measurement.

5.2 Experiment

The cell configuration and electrolyte composition are the same as described in Chapter 4. The cell is charged to 100% SoC using chronoamperomety as described previously. Electrochemical measurements were performed using a Bio-Logic HCP-803 high current potentiostat. Electrochemical impedance spectroscopy (EIS) was used to characterize the individual responses of the positive and the negative electrode to polarization. The electrode of interest was polarized for two minutes to reach a steady state current. The impedance of the electrode was then measured using a 5mV sinusoidal perturbation superimposed onto the DC polarization potential. After the impedance measurement, the DC polarization was increased incrementally to establish the steady state polarization curve for the individual electrode with a complex impedance spectrum measured at each point on the curve. The reference electrode response was checked by comparing the sum of the positive and the negative spectra with that of the full cell response, indicating that the reference electrode does not interfere with the impedance measurement at the frequency up to 60 kHz. Measurements were performed at 20 °C (monitored by a thermocouple). The open circuit voltage (OCV) was monitored before and after each discharge measurement. A constant flow rate of 50 mL/min was controlled

on bromine electrode. This stoichiometric flow rate is approximately 50 on the bromine electrode.

Two symmetric cells were also assembled with the same 5 cm^2 cell hardware. The symmetric cells are assembled to allow the same electrolyte to flow on both sides of the battery. The hydrogen symmetric cell MEA consists of two pieces of Nafion®117 half MEAs, which allows the insertion of a DHE reference electrode with Pt on both sides of the cell. Toray carbon paper was assembled on each side of the cell and the hydrogen flow rate was 50ml/min on both sides. The bromine symmetric cell consists of two pieces of Nafion®117 and two pieces of SGL 10AA carbon paper without any Pt. The bromine flow was split to feed in both sides of the battery.

5.3. Results and Discussion

With the assistance of a DHE reference electrode, we were able to separate and polarize each electrode to obtain the polarization curves as a function of cell current. As we discussed in Chapter 3, the positive and negative electrodes contribute approximately the same amount of overpotential to the whole cell overpotential, with the negative electrode slightly higher than the positive electrode. To further investigate the electrode voltage losses, electrochemical impedance spectroscopy (EIS) was conducted on each half-cell in an attempt to isolate the processes contributing to the total cell overpotential. Nyquist impedance plots at various overpotentials for the positive and the negative electrode are shown below. The reference electrode was sandwiched between two Nafion®212 membranes. Thus the high frequency resistance R_{hf}, is attributed to the

resistance of one membrane for each half-cell. The semicircle fitting equivalent circuit used for negative and positive electrode is show in the Fig 5.1a. It consists of the high frequency resistance R_{hf} in series with a parallel circuit of a faradaic charge transfer resistance R_{ct} and a constant phase element Q which is double layer capacitance corrected with a parameter p. In addition, the semicircle fitting equivalent circuit for the whole cell is show in the Fig 5.1b. It consists of the high frequency resistance R_{hf}, which is the summation of the high frequency resistance from negative and positive electrodes, respectively. The R_{hf} is in series with two parallel circuits representing negative and positive electrodes same as in Fig 5.1a.

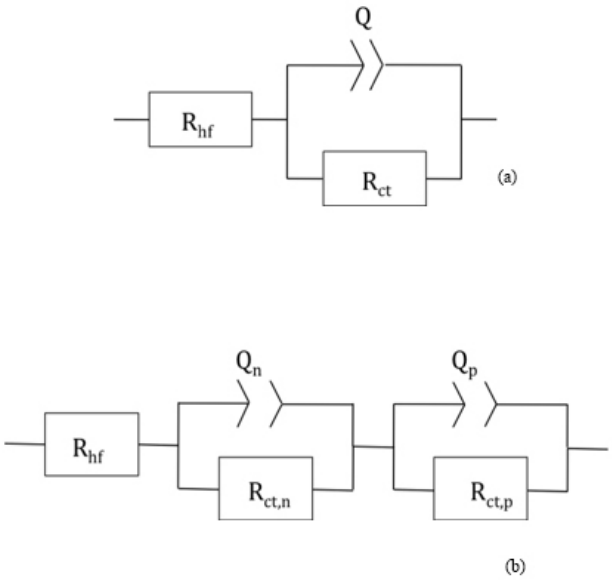


Figure 5.1 Equivalent Circuit of EISThe equivalent circuit of the half cell EIS. R_{hf} is the high frequency resistance, R_{ct}, is the charge transfer resistance, Q is the constant phase element from double layer capacitance (b) The equivalent circuit of the whole cell EIS. R_{hf} is the summation of the negative and positive electrodes high frequency resistance, $R_{ct,n}$, $R_{ct,p}$, are the charge transfer resistance on negative and positive electrodes, respectively. Q_n, Q_p are the constant phase elements on negative and positive electrodes, respectively.

5.3.1 Regular Asymmetric Whole Cell

The whole cell discharge polarization curve and its EIS are measured in a conventional cell setup without DHE. The EIS arc of whole cell represents the summation of impedances from positive and negative electrode EIS. Thus, Fig 5.2 shows the impedance change in general for a hydrogen bromine redox flow battery. The arc represents the EIS at each relevant overpotential shown in the sub-figure polarization curve. The high frequency resistance is consistent at 0.45 ohms•cm^2 with increasing overpotential. However, the arc size increases appreciably during discharging, especially at high overpotential (>0.2V). We previous showed that the "hook" feature appears at the end of the polarization curve, where the current density starts to decrease dramatically with increasing overpotential. The relevant impedance arc is shown as from D to E, where the arc size keeps increasing with increasing overpotential. This phenomenon might suggest that the cell impedance is not current dependent but overpotential dependent, since the arc only varies with respect to the overpotential. In addition, at D and E, the arc diameter increases dramatically, which suggests that the impedance increment is huge at that potential. As mentioned in chapter 4, a side reaction possibly occurs at this potential that blocked the reaction site and increased the diffusion.

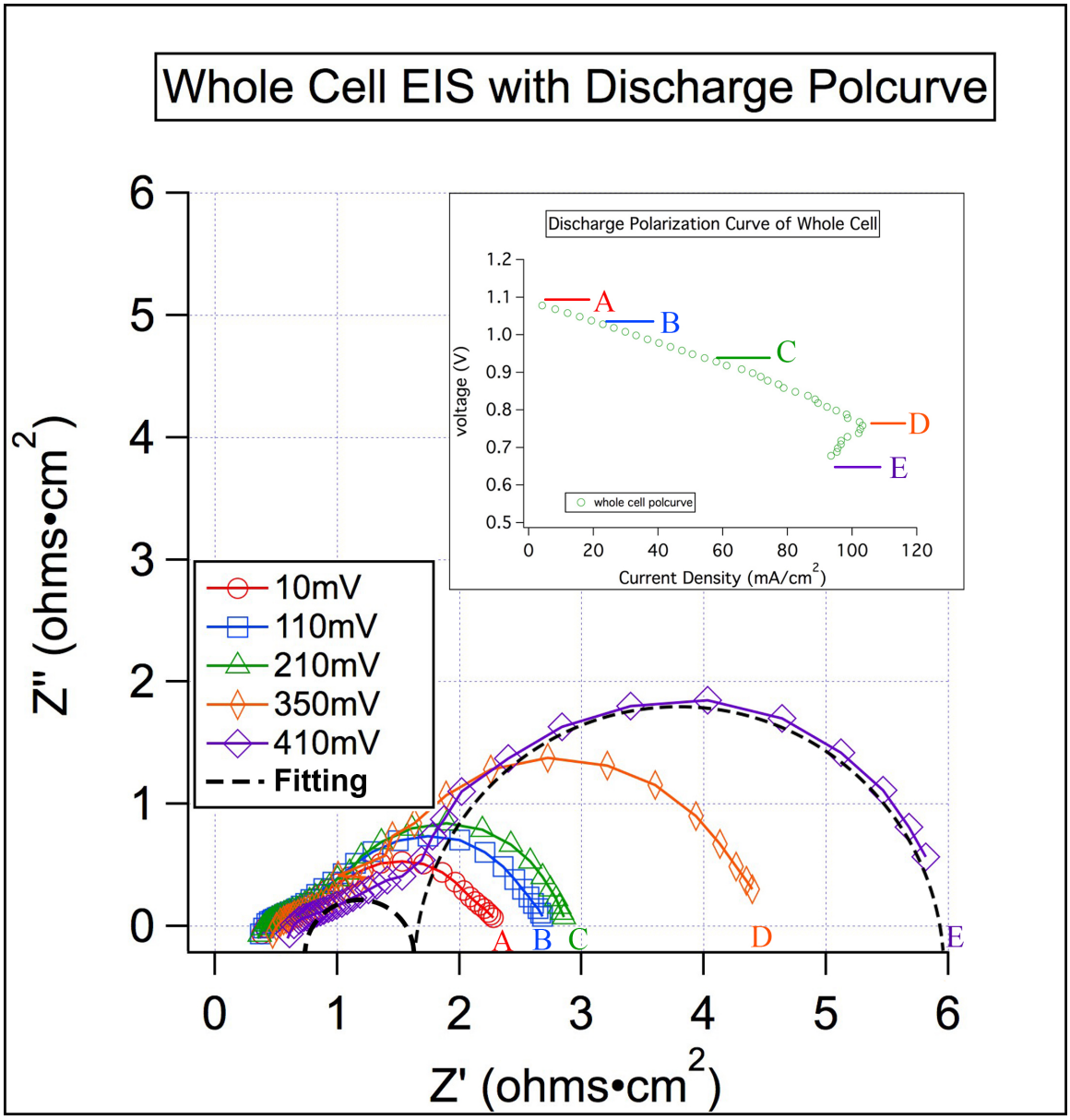


Figure 5.2 Whole Cell EIS The impedance measurement of the whole cell during a discharge polarization curve. The arc of the semicircle increases as cell discharging.

To further investigate the EIS, we inserted a DHE reference electrode to study the impedance on each electrode separately. The OCV of the cell was measured with the DHE, and the OCV of the cell equals the difference between the potential on each electrode. The real and imaginary parts of EIS on each side of the battery were calculated at each fixed frequency. The results added up to the whole cell impedance, thus validating the use of the DHE to monitor the EIS in the cell. The impedance measured for positive electrode is shown in Fig 5.3. R_{hf}, R_{ct}, and Q can be quantified by fitting the data according to the equivalent circuit in Fig 5.1. The resistance is normalized by the cell geometric area ($5cm^2$) and Q is normalized by electrode surface area measured with BET. Previous chapter proposed 4 hypotheses for the "hook" feature in the conclusion. Hypotheses (1) and (2) suggest the bromine in carbon paper hinders the further reactions. Here, on the positive electrode, bromine/bromide solution directly contacts the carbon paper, and the experimental conditions are the same as described before in the "hook"-feature discharge polarization curve. The sub-figure in Fig 5.1 shows that the discharge polarization curve on the bromine electrode does not present "hook" feature over the overpotential range (up to 0.4 V). This suggests that the hypotheses (1) and (2) are not applicable to the "hook" feature.

The arc shown in Fig 5.3 presents a pure kinetic feature, which the high frequency arc diameter decreases with increased overpotential. R_{hf}, R_{ct}, and Q are calculated and shown in Fig 5.4. As the current density increased, the high frequency resistance remained at 0.3 ohms•cm^2. We adapted the zero gap cell configuration, and the membrane was well hydrated in contact with HBr solution. Thus, high frequency

resistance (mainly from the membrane resistance) was not influenced appreciably by polarization. Meanwhile, Fig 5.4 shows the charge transfer resistance decreases exponentially with increasing polarization. The reason is that as the electrode is polarized, the energy barrier for charge transfer was lowered, which is preferable for charge transfer in electrode. The results are generally consistent with Tafel kinetics we measured in last chapter. In addition, the capacitance decreases according to a second order polynomial, with increasing polarization. This might suggest that (1) bromine or bromide is able to block active sites on electrode and lead to a loss in the capacitance; or (2) less of the electrode is accessed as the overpotential is increased. The mechanism of bromine reduction reaction on carbon has not been studied extensively, thus further experiments are needed to validate these hypotheses.

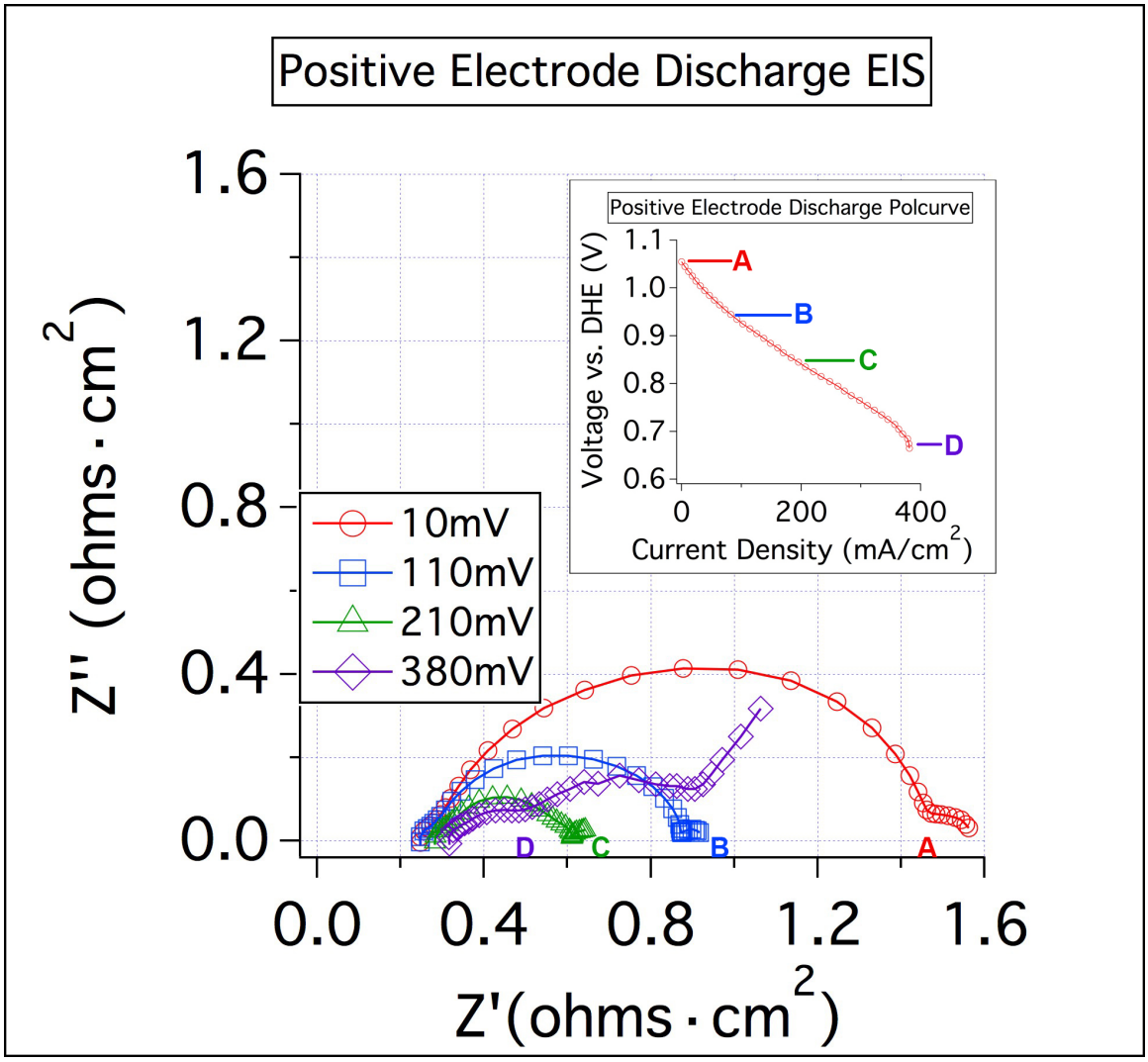


Figure 5.3 Bromine Electrode EIS The impedance measurement of bromine electrode during a discharge polarization curve.

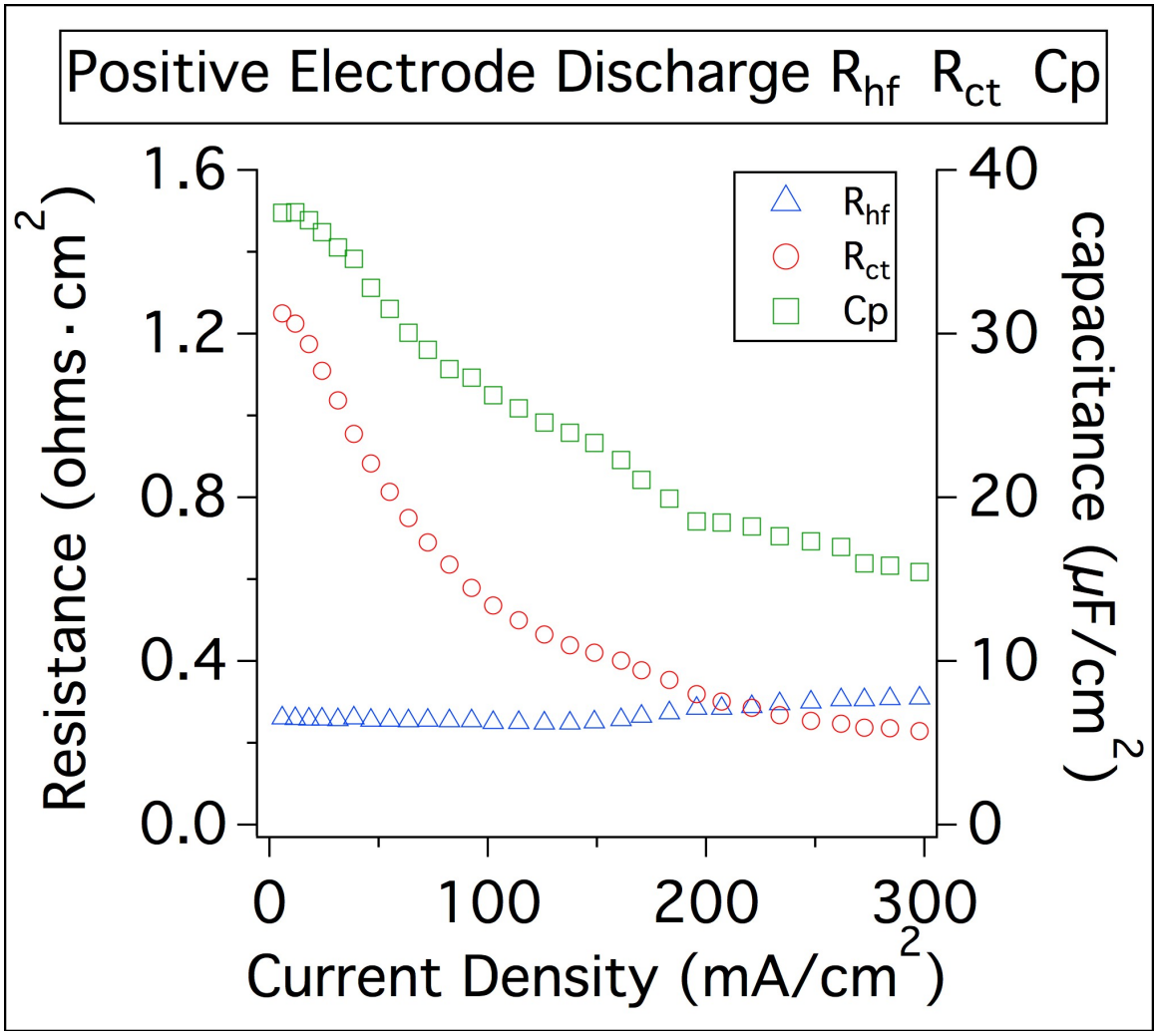


Figure 5.4 Resistances and Capacitance at the Bromine Electrode

The EIS on the negative electrode shows an even more complicated system. Previous studies show a strong the adsorption of bromide and bromine occurs on Pt surface, which involves the generation of tribromide.[222,223] The experiment was implemented by flipping the working and counter electrodes of the potentiostat on the current collectors; therefore the working electrode measured the negative electrode. The sub-figure in Fig 5.5 shows the iR-corrected polarization curve of this process. A "hook" at the end of the polarization curve is observed. This suggests that this anomalous feature of the hydrogen bromine redox flow battery occurs on the negative electrode. As we mentioned in preceding Chapter 4, the "hook" feature starts at a certain overpotential (0.37 V). It suggests the most likely hypothesis is that the bromide adsorption on the Pt surface at this overpotential, rather than the side reactions. The impedance measurement of negative electrode is shown in Fig 5.5. As the current density increased, the high frequency resistance was stable at 0.15 ohms•cm^2. Here, we note the negative electrode has a lower ASR than positive electrode. The reason is that the membrane on the negative electrode is hot-pressed with Pt that directly contacts with the carbon paper electrode and thus lowers the contact resistance in the cell. At extremely low overpotential the arc increases, (A -> B); following the arc decreases, (B -> C); at higher overpotential the impedance arc grows substantially (C -> D -> E -> F).

Fig 5.6 shows the normalized hydrogen electrode high frequency resistance, R_{hf}; charge transfer resistance, R_{ct}; and the double layer capacities, Q. R_{ct} is normalized by the cell geometric area (5cm^2) and Q is normalized by electrochemical surface area (ECSA). The integral of the resistance in Fig 5.6 over current density shows that the overpotential

is fully reflected in the impedance spectra. As we increasingly polarized the electrode, the high frequency resistance was consistent at 0.15 ohms•cm^2, which arises mainly from the membrane resistance and which was not influenced appreciably by polarization. Unlike the positive electrode, the charge transfer resistance R_{ct} increased initially, the decreased, and finally increased appreciably. The reason for the initial increase is unclear. It could due to the experimental initial conditioning process, as the electrode was not fully saturated with water initially and influenced the R_{ct}. The decrease in R_{ct} reflects the same reason as the positive electrode, when the energy barrier for charge transfer was lowered with increased overpotential. However, the R_{ct} increased tremendously at high overpotentials. It could due to the crossover of bromide or bromine thus competes with hydrogen on negative electrode. Fig 5.5 shows that the R_{ct} increases significantly with increased overpotential, especially in the "hook" region. Cyclic voltammetry study of hydrogen on Pt in bromide solution shows that the bromide can influence the hydrogen adsorption, however, only at high concentrations, it significantly diminishes the hydrogen adsorption.[198] However, the crossover rate of bromide is not substantially high.[197] Conway *et al*. showed that the presence of bromine increased the R_{ct} about 3 times than that in the pure bromide solution.[222] Lee and Loo *et al*. using Raman spectroscopy observed that bromine and tribromide coadsorbed on Pt surface.[224] Since Fig 5.5 shows the substantial increase of R_{ct} especially at high overpotentials, it is possible that, at high overpotentials, bromine or tribromide comes cross the membrane, and stagnates in the negative electrode or adsorbs on the Pt surface. This can lead to the significantly increase of the R_{ct} and obvious current density drops at high overpotentials, even a "hook" in the

polarization curve. The constant phase element capacitance Q increases with increased overpotential. This could be an artifact of analysis or it reflects a real physical phenomenon; further investigation of the ECSA is needed.

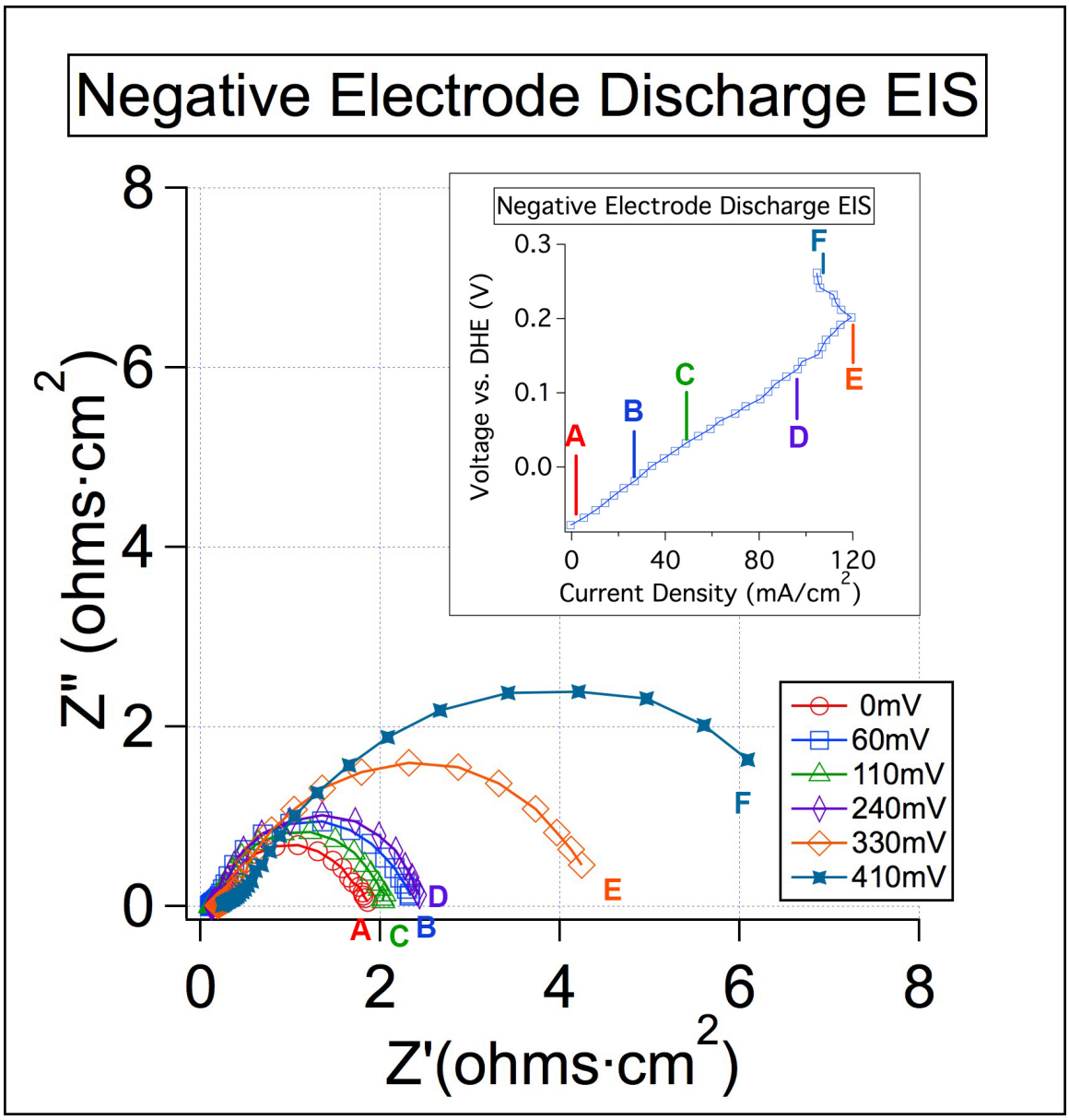


Figure 5.5 The Hydrogen Electrode Discharge Polarization Curve EIS

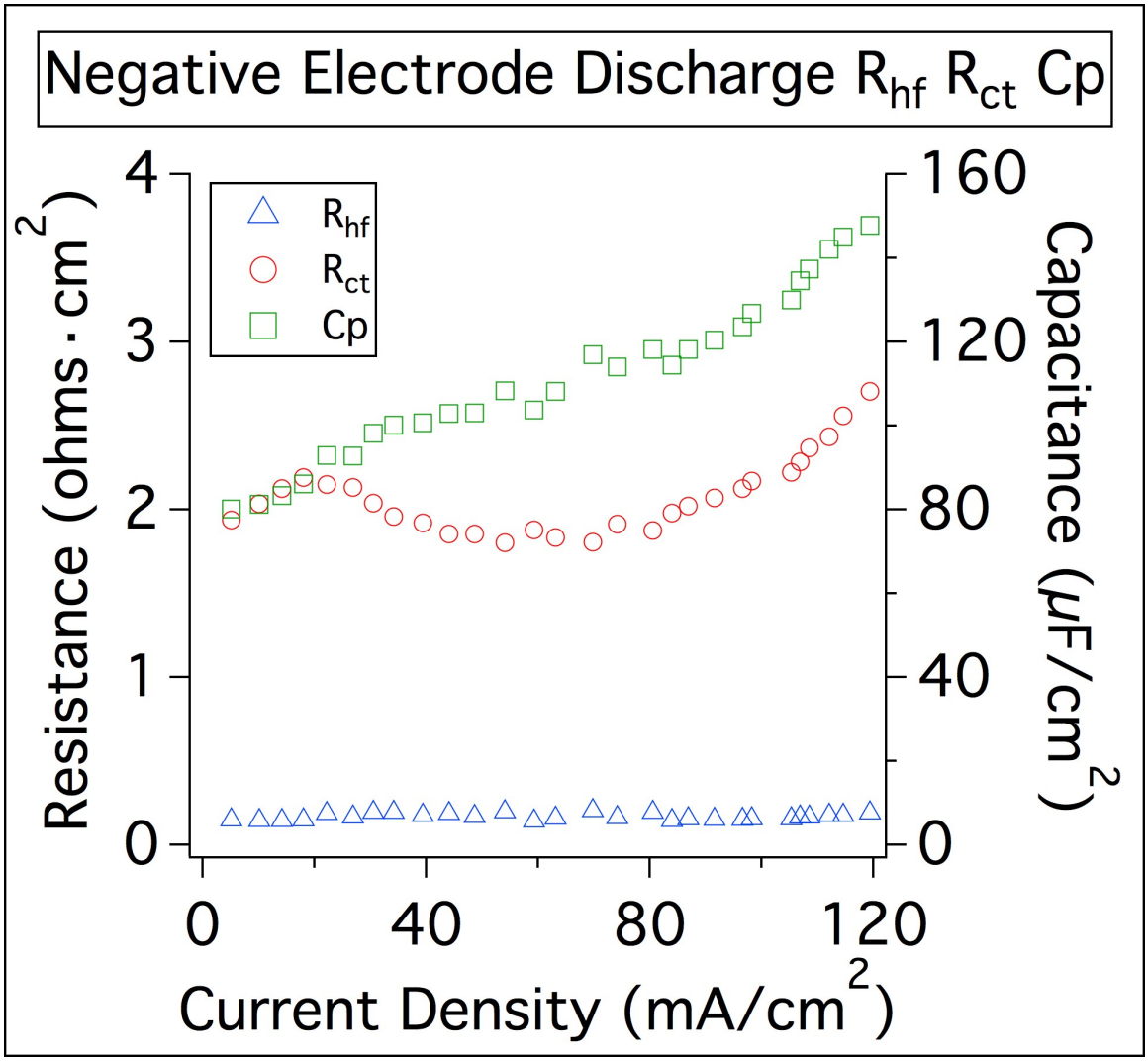


Figure 5.6 Resistance and Capacitance for the Hydrogen Electrode

5.3.2 Symmetric Cell

To investigate the performance of the hydrogen electrode in the hydrogen bromine redox flow battery, two symmetric cells were assembled. The hydrogen symmetric cell was designed in a way that hydrogen flows in both sides of the flow battery; and the bromine symmetric cell was designed to flow HBr/Br_2 on both sides of the flow battery. A DHE was inserted to separately study the cell performance. The reactions in the hydrogen and bromine symmetric battery are shown as below:

$$H_2 = 2H^+ + 2e^-;$$

$$Br_2 + 2e^- = 2Br^-$$

Fig 5.7 and 5.8 simulate the whole cell discharge polarization process in separated cells. The hydrogen electrode was positively polarized and the bromine electrode was negatively polarized. The negative electrode The EIS data is shown in Fig 5.7. Due to the dehydration of the hydrogen electrode, no data is available at higher overpotentials in the polarization curve in the sub-figure of Fig 5.7. Compared with Fig 5.5, the R_{hf} in a symmetric cell is much higher and grows much faster than the hydrogen electrode in a regular asymmetric cell. Chapter 3 discussed the dramatic proton conductivity loss due to the drying effect of the membranes. Himanen *et al*. measured impedance of the hydrogen electrode in a symmetrical hydrogen-hydrogen cell.[225] It shows that the impedance of the hydrogen electrode is dependent on the humidity of the ingoing hydrogen streams. The higher the humidity, the lower the R_{hf}. Here, the hydrogen symmetric cell configuration

contains no liquid water in contact with the membrane. Therefore, it suggests that the high R_{hf} in Fig 5.7 comes from the drying effect of the membrane. The impedance increases moderately over this overpotential range, which also agrees with the data from Himanen *et al*. In addition, compared with the whole cell measurement, the arc diameters of the hydrogen symmetric cell EIS is a much lower, which means a much lower R_{ct}. This suggests that, in absent of bromine/bromide electrolyte on the positive electrode, hydrogen can easily be adsorbed on the Pt surface. This also suggests that the "hook" feature more likely comes from the hypothesis of bromine/bromide adsorption than that of the side reactions.

The discharging of the bromine electrode is shown in Fig 5.8. The discharge of the bromine electrode shows a typical kinetic arc trend of charge transfer resistance: with increasing polarization, the bromine electrode shows consistent R_{hf} and substantial decrease in Rct. These results are the same as those from a regular whole cell measurement. The R_{ct} is slightly lower than the whole cell. The reason could be that the symmetric configuration sustains the electrolyte consistency in the cell, thus lower the R_{ct} as a whole. No "hook" feature is observed in polarization curve shown in the sub-figure of Fig 5.8.

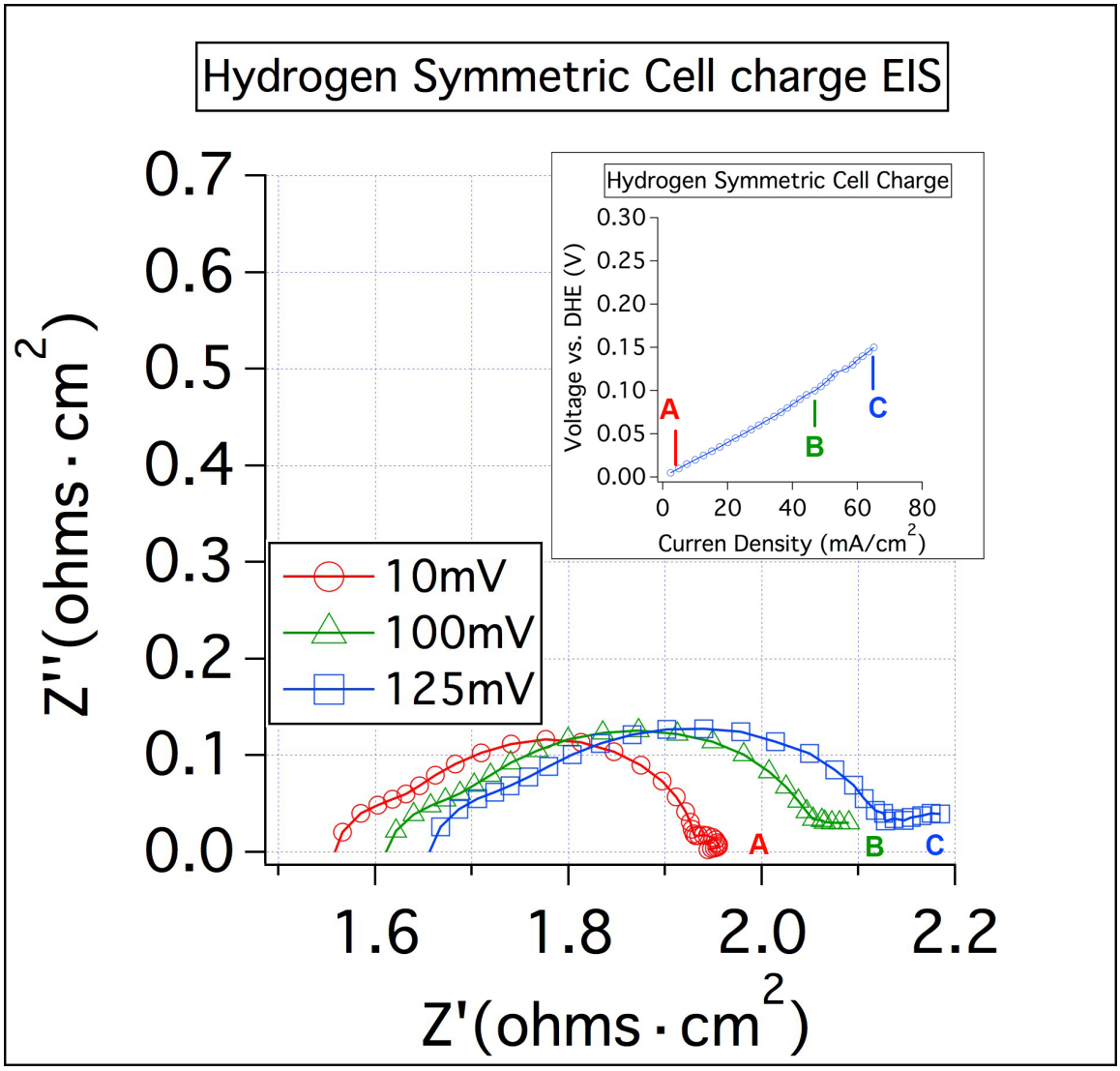


Figure 5.7 Hydrogen Symmetric Cell Charge EIS

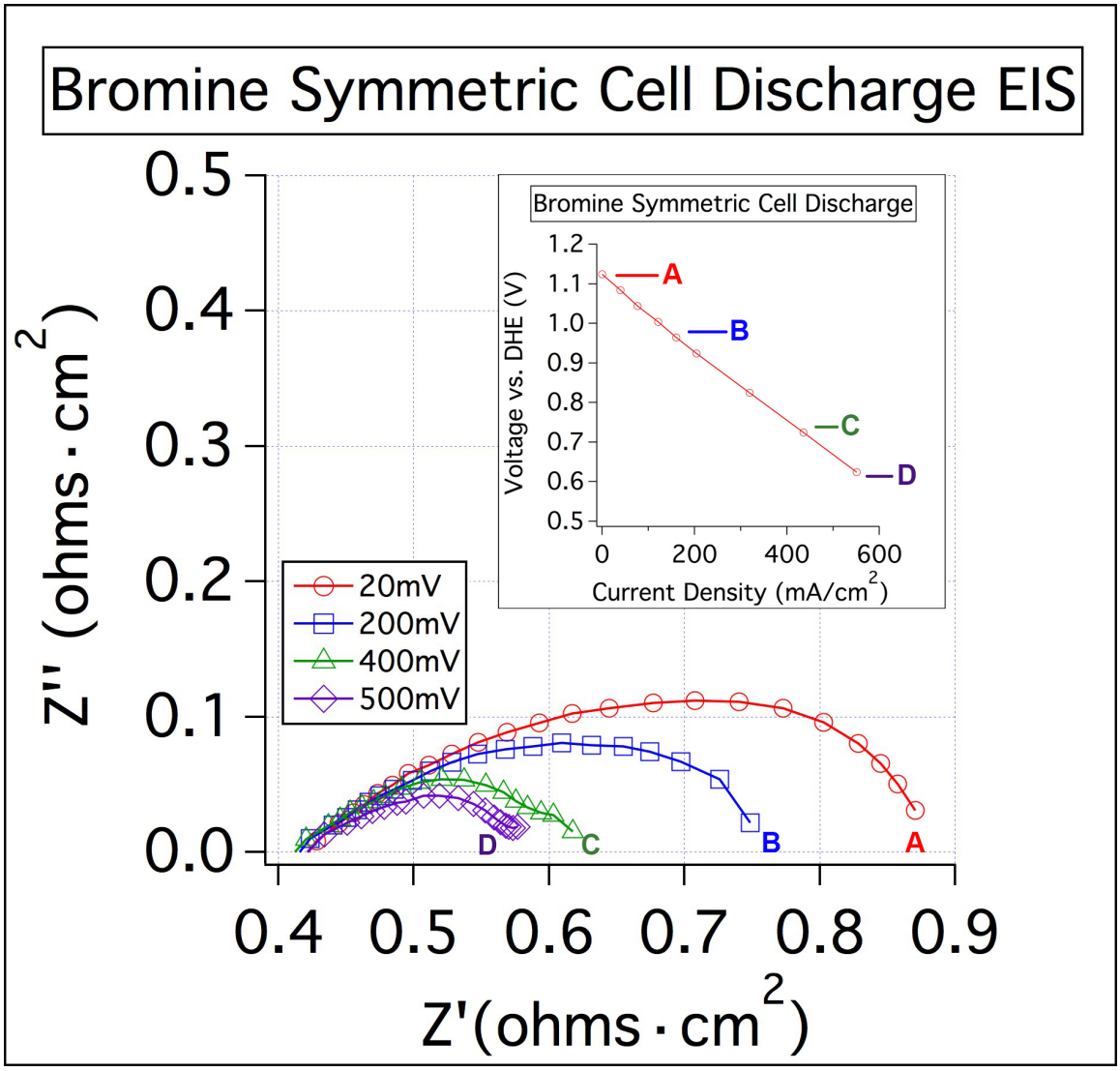


Figure 5.8 Bromine Symmetric Cell Discharge EIS

Fig 5.9 and 5.10 simulate the whole cell charge polarization process in separated cells. The hydrogen electrode was negatively polarized and the bromine electrode was positively polarized. Fig 5.9 shows that the hydrogen electrode charging EIS presents a similar feature as in the discharging EIS in Fig 5.7. The high R_{hf} comes from the membrane dehydration. Noticed that the hydrogen discharge R_{hf} (Fig 5.9) is lower than that of the charge R_{hf} (Fig 5.7), this results from the experimental procedure we applied. The hydrogen discharge measurement (Fig 5.9) was conducted first, thus the membrane dehydration was not as severe as the hydrogen charging measurement (Fig 5.7). Fig 5.9 shows that the arc diameters of hydrogen discharge are on the same magnitude as those of hydrogen charge (Fig 5.7). This further proves that, in absent of bromine electrode, the hydrogen electrode contains a much lower R_{ct} in both charge and discharge. In addition, compared with Fig 5.8, the EIS of bromine electrode is identical during charge and discharge, which means that the bromine electrode has the same R_{hf}, R_{ct}. In addition, the charge and discharge polarization curves of bromine electrode can overlap each other. This indicates that the bromine electrode is highly reversible during charge and discharge.

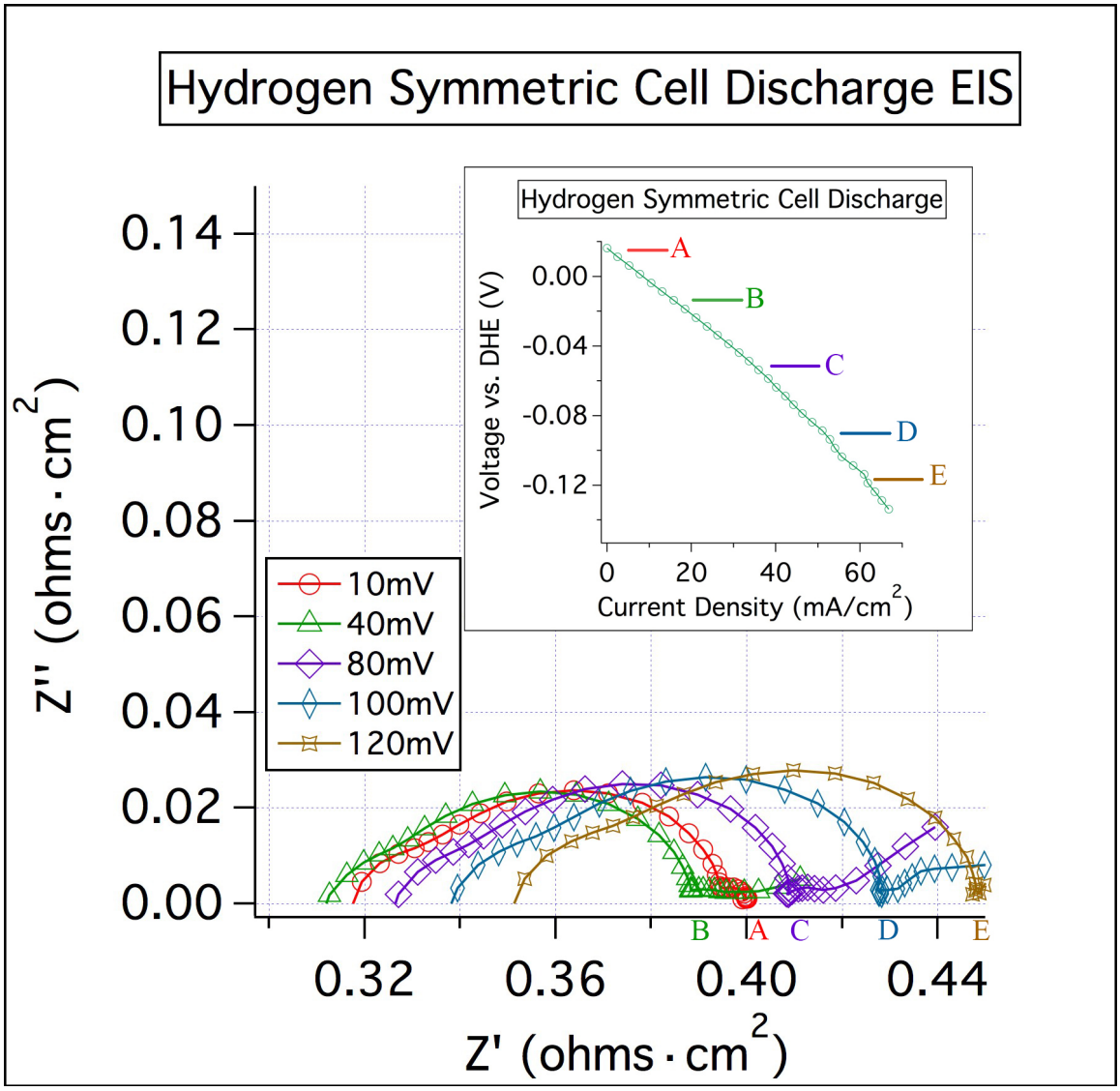


Figure 5.9 Hydrogen Symmetric Cell Discharge EIS

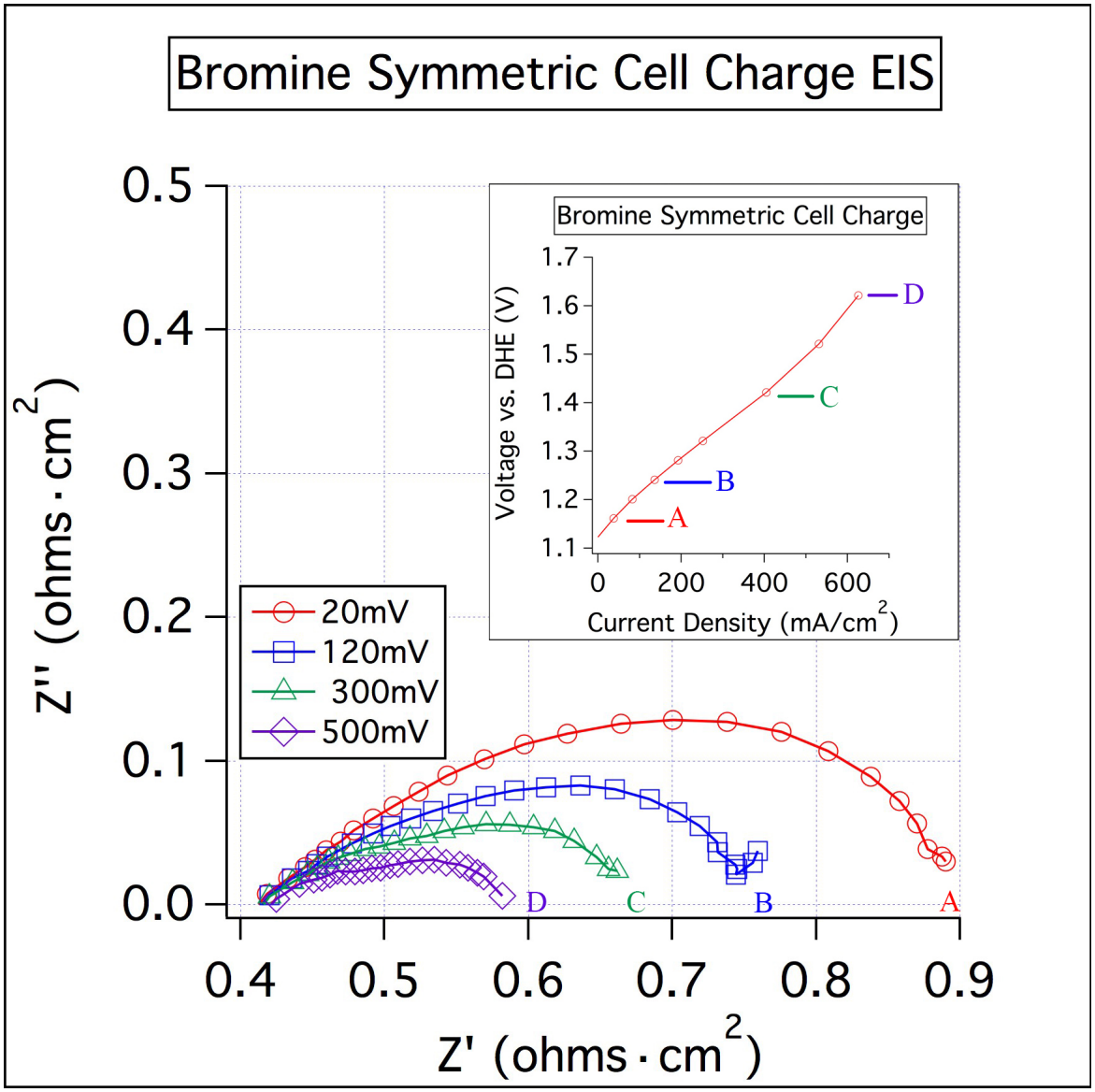


Figure 5.10 Bromine Symmetric Cell Charge EIS

5.4 Conclusion

In this chapter the use of electrochemical impedance spectroscopy (EIS) with a dynamic hydrogen reference electrode (DHE) is demonstrated. More detailed information on kinetic and ohmic losses vs. overpotential was collected from this study on both electrodes. Asymmetric cell study shows that the bromine electrode does not present "hook" feature over the overpotential range (up to 0.4 V), and it shows a pure kinetic response. The R_{ct} decreases as we increasingly polarize the electrode. In addition, the results of the hydrogen electrode show that the R_{ct} decreases at first, and increases dramatically at higher overpotentials. The polarization curves show that the "hook" feature is in only present on the negative electrode.

Furthermore, two symmetric cells were assembled to study each individual electrode separately. The hydrogen electrode in symmetric cell shows that the R_{hf} increases substantially, which can be explained as the membrane dehydration effect. The bromine electrode is highly reversible during charge and discharge. The hydrogen electrode contains a much lower R_{ct} in the symmetric cell than that in the whole cell measurement. Thus we conjecture that the crossover of bromine and tribromide could lead to their adsorption on the Pt surface. This mechanism competes with the hydrogen adsorption process and increases the R_{ct}, which eventually leads to the "hook" feature in the polarization curves.

List of References

1. Dresselhaus, M. S. & Thomas, I. L. Alternative energy technologies. *Nature* **414,** 332–7 (2001).

2. DOE Types of Fuel Cells. at <http://www1.eere.energy.gov/hydrogenandfuelcells/fuelcells/fc_types.html>

3. Wang, Y., Chen, K. S., Mishler, J., Cho, S. C. & Adroher, X. C. A review of polymer electrolyte membrane fuel cells: Technology, applications, and needs on fundamental research. *Appl. Energy* **88,** 981–1007 (2011).

4. Garche, J. & Jorissen, L. *Handbook of fuel cells. Fundamentals technology and applications*. **83,** (2003).

5. Dyer, C. K. Fuel cells for portable applications. *J. Power Sources* **106,** 31–34 (2002).

6. Gittleman, C. *et al.* Automotive fuel cell R&D needs. In: DOE fuel cell pre-solicitation workshop. (2010).

7. Schmittinger, W. & Vahidi, A. A review of the main parameters influencing long-term performance and durability of PEM fuel cells. *J. Power Sources* **180,** 1–14 (2008).

8. Borup, R. *et al.* Scientific aspects of polymer electrolyte fuel cell durability and degradation. *Chem. Rev.* **107,** 3904–51 (2007).

9. Steinbach, A. 2013 Annual Merit Review High Performance , Durable , Low Cost Membrane Electrode Assemblies for Transportation Applications. (2013).

10. DOE. Hydrogen and fuel cell activities, progress, and plans- report to congress. (2009). at <http://www.hydrogen.energy.gov/pdfs/ epact_report_sec811.pdf>

11. James, B. D. & Spisak, A. B. Mass Production Cost Estimation of Direct H 2 PEM Fuel Cell Systems for Transportation Applications. 1–62 (2012).

12. Smitha, B., Sridhar, S. & Khan, a. a. Solid polymer electrolyte membranes for fuel cell applications—a review. *J. Memb. Sci.* **259,** 10–26 (2005).

13. Merlo, L., Ghielmi, a., Cirillo, L., Gebert, M. & Arcella, V. Membrane Electrode Assemblies Based on HYFLON ® Ion for an Evolving Fuel Cell Technology. *Sep. Sci. Technol.* **42,** 2891–2908 (2007).

14. Li, Q., Jensen, J. O., Savinell, R. F. & Bjerrum, N. J. High temperature proton exchange membranes based on polybenzimidazoles for fuel cells. *Prog. Polym. Sci.* **34,** 449–477 (2009).

15. Paul, R. *et al.* Vehicle Mechanism , A New Model for the Interpretation of the Conductivity of Fast Proton Conductors Photochemical Oxidative Addition of Chlorine from. **122,** 1981–1982 (1982).

16. Kornyshev, A. A., Kuznetsov, a. M., Spohr, E. & Ulstrup, J. Kinetics of Proton Transport in Water. *J. Phys. Chem. B* **107,** 3351–3366 (2003).

17. Marx, D. & Parrinello, M. The nature of the hydrated excess proton in water. 601–604 (1999).

18. Springer, T. E., Zawodzinski, T. A. & Gottesfeld, S. Polymer Electrolyte Fuel Cell Model. *J. Elec* **138,** 2334–2342 (1991).

19. Cappadonia, M., Erning, J. W. & Stimming, U. Proton conduction of Nafion® 117 membrane between 140 K and room temperature. *J. Electroanal. Chem.* **376,** 189–193 (1994).

20. Wang, Y., Mukherjee, P. P., Mishler, J., Mukundan, R. & Borup, R. L. Cold start of polymer electrolyte fuel cells: Three-stage startup characterization. *Electrochim. Acta* **55,** 2636–2644 (2010).

21. Thompson, E. L., Capehart, T. W., Fuller, T. J. & Jorne, J. Investigation of Low-Temperature Proton Transport in Nafion Using Direct Current Conductivity and Differential Scanning Calorimetry. *J. Electrochem. Soc.* **153,** A2351 (2006).

22. Cappadonia, M., Erning, J. W., Niaki, S. M. S. & Stimming, U. Conductance of Nafion 117 membranes as a function of temperature and water content. *Solid State Ionics* **77,** 65–69 (1995).

23. Elfring, G. J. & Struchtrup, H. Thermodynamics of pore wetting and swelling in Nafion. *J. Memb. Sci.* **315,** 125–132 (2008).

24. Vallieres, C. *et al.* On Schroeder's paradox. *J. Memb. Sci.* **278,** 357–364 (2006).

25. Freger, V. Hydration of ionomers and Schroeder's paradox in Nafion. *J. Phys. Chem. B* **113,** 24–36 (2009).

26. Motupally, S., Becker, A. J. & Weidner, J. W. Diffusion of Water in Nafion 115 Membranes. *J. Electrochem. Soc.* **147,** 3171 (2000).

27. Zawodzlnski, T. A., Springer, T. E., Urlbe, F. & Gottesfeld, S. Characterization of polymer electrolytes for fuel cell applications. *Solid State Ionics* **60,** 199–211 (1993).

28. Ye, X. & Wang, C.-Y. Measurement of Water Transport Properties Through Membrane-Electrode Assemblies. *J. Electrochem. Soc.* **154,** B676 (2007).

29. Ge, S., Yi, B. & Ming, P. Experimental Determination of Electro-Osmotic Drag Coefficient in Nafion Membrane for Fuel Cells. *J. Electrochem. Soc.* **153,** A1443 (2006).

30. Xie, G. & Okada, T. Water Transport Behavior in Nation 117 Membranes. **142,** 2–7 (1995).

31. Fuller, T. F. & Newman, J. Experimental Determination of the Transport Number of Water in Nation 117 Membrane. **139,** 1332–1337 (1992).

32. Ise, M., Kreuer, K. D. & Maier, J. Electroosmotic drag in polymer electrolyte membranes : an electrophoretic NMR study. **125,** 213–223 (1999).

33. Adachi, M., Navessin, T., Xie, Z., Frisken, B. & Holdcroft, S. Correlation of In Situ and Ex Situ Measurements of Water Permeation Through Nafion NRE211 Proton Exchange Membranes. *J. Electrochem. Soc.* **156,** B782 (2009).

34. Bernardi, D. M. & Verbrugge, M. W. A Mathematical Model of the Solid-Polymer-Electrolyte Fuel Cell. **139,** (1992).

35. Buchi, F. N., Wakizoe, M. & Srinivasan, S. Microelectrocle Investigation of Oxygen Permeation in Perfluorinatecl Proton Exchange Membranes with Different Equivalent Weights. **143,** 927–932 (1996).

36. Weber, A. Z. & Newman, J. Transport in Polymer-Electrolyte Membranes. *J. Electrochem. Soc.* **150,** A1008 (2003).

37. Debe, M. *Final Report - Advanced Cathode Catalysts and Supports for PEM Fuel Cells*. (2010). doi:10.2172/1052138

38. Bashyam, R. & Zelenay, P. A class of non-precious metal composite catalysts for fuel cells. *Nature* **443,** 63–6 (2006).

39. Bezerra, C. *et al.* A review of Fe–N/C and Co–N/C catalysts for the oxygen reduction reaction. *Electrochim. Acta* **53,** 4937–4951 (2008).

40. Wang, B. Recent development of non-platinum catalysts for oxygen reduction reaction. *J. Power Sources* **152,** 1–15 (2005).

41. Gottesfeld, S. & Pafford, J. A New Approach to the Problem of Carbon Monoxide Poisoning in Fuel Cells Operating at Low Temperatures. 2651–2652

42. Dhathathreyan, K. & Rajalakshmi, N. *Polymer-electrolyte membrane fuel cell*. **2000,** (Anamaya Publishers, 2006).

43. Zelenay, P. Advanced cathode catalysts. *2010 Hydrog. Progr. Annu. merit Rev. ...* (2010). at <http://hydrogendoedev.nrel.gov/pdfs/review09/fc_21_zelenay.pdf>

44. Mukherjee, P. P. & Wang, C.-Y. Direct Numerical Simulation Modeling of Bilayer Cathode Catalyst Layers in Polymer Electrolyte Fuel Cells. *J. Electrochem. Soc.* **154,** B1121 (2007).

45. Mukherjee, P. P. & Wang, C.-Y. Stochastic Microstructure Reconstruction and Direct Numerical Simulation of the PEFC Catalyst Layer. *J. Electrochem. Soc.* **153,** A840 (2006).

46. Wang, G., Mukherjee, P. P. & Wang, C.-Y. Direct numerical simulation (DNS) modeling of PEFC electrodes Part I. Regular microstructure. *Electrochim. Acta* **51,** 3139–3150 (2006).

47. Wang, G., Mukherjee, P. P. & Wang, C.-Y. Direct numerical simulation (DNS) modeling of PEFC electrodes Part II. Random microstructure. *Electrochim. Acta* **51,** 3151–3160 (2006).

48. Ferreira, P. J. *et al.* Instability of Pt/C Electrocatalysts in Proton Exchange Membrane Fuel Cells. *J. Electrochem. Soc.* **152,** A2256 (2005).

49. Borup, R. L., Davey, J. R., Garzon, F. H., Wood, D. L. & Inbody, M. a. PEM fuel cell electrocatalyst durability measurements. *J. Power Sources* **163,** 76–81 (2006).

50. Akita, T. *et al.* Analytical TEM study of Pt particle deposition in the proton-exchange membrane of a membrane-electrode-assembly. *J. Power Sources* **159,** 461–467 (2006).

51. Wang, X., Kumar, R. & Myers, D. J. Effect of Voltage on Platinum Dissolution. *Electrochem. Solid-State Lett.* **9,** A225 (2006).

52. Yasuda, K., Taniguchi, A., Akita, T., Ioroi, T. & Siroma, Z. Characteristics of a Platinum Black Catalyst Layer with Regard to Platinum Dissolution Phenomena in a Membrane Electrode Assembly. *J. Electrochem. Soc.* **153,** A1599 (2006).

53. Kim, L., Chung, C. G., Sung, Y. W. & Chung, J. S. Dissolution and migration of platinum after long-term operation of a polymer electrolyte fuel cell under various conditions. *J. Power Sources* **183,** 524–532 (2008).

54. Yasuda, K., Taniguchi, A., Akita, T., Ioroi, T. & Siroma, Z. Platinum dissolution and deposition in the polymer electrolyte membrane of a PEM fuel cell as studied by potential cycling. *Phys. Chem. Chem. Phys.* **8,** 746–52 (2006).

55. Ismagilov, Z. R. *et al.* Development of active catalysts for low Pt loading cathodes of PEMFC by surface tailoring of nanocarbon materials. *Catal. Today* **102-103,** 58–66 (2005).

56. Wan, C.-H., Zhuang, Q.-H., Lin, C.-H., Lin, M.-T. & Shih, C. Novel composite anode with CO "Filter" layers for PEFC. *J. Power Sources* **162,** 41–50 (2006).

57. Franco, A. A., Guinard, M., Barthe, B. & Lemaire, O. Impact of carbon monoxide on PEFC catalyst carbon support degradation under current-cycled operating conditions. *Electrochim. Acta* **54,** 5267–5279 (2009).

58. Chen, C.-H., Chung, C.-C., Lin, H.-H. & Yan, Y.-Y. Improvement of CO Tolerance of Proton Exchange Membrane Fuel Cell by an Air-Bleeding Technique. *J. Fuel Cell Sci. Technol.* **5,** 014501 (2008).

59. Zamel, N. & Li, X. Transient analysis of carbon monoxide poisoning and oxygen bleeding in a PEM fuel cell anode catalyst layer. *Int. J. Hydrogen Energy* **33,** 1335–1344 (2008).

60. Uribe, F. A., Gottesfeld, S. & Zawodzinski, T. A. Effect of Ammonia as Potential Fuel Impurity on Proton Exchange Membrane Fuel Cell Performance. *J. Electrochem. Soc.* **149,** A293 (2002).

61. Zhang, S. *et al.* A review of platinum-based catalyst layer degradation in proton exchange membrane fuel cells. *J. Power Sources* **194,** 588–600 (2009).

62. Siegel, N. P. Development and Validation of a Computational Model for a Proton Exchange Membrane Fuel Cell. (2004).

63. Siegel, N. P., Ellis, M. W., Nelson, D. J. & Spakovsky, M. R. von. Single domain PEMFC model based on agglomerate catalyst geometry. *J. Power Sources* **115,** 81–89 (2003).

64. Harvey, D., Pharoah, J. G. & Karan, K. A comparison of different approaches to modelling the PEMFC catalyst layer. *J. Power Sources* **179,** 209–219 (2008).

65. Schwarz, D. H. & Djilali, N. 3D Modeling of Catalyst Layers in PEM Fuel Cells. *J. Electrochem. Soc.* **154,** B1167 (2007).

66. Shah, A. A., Kim, G.-S., Sui, P. C. & Harvey, D. Transient non-isothermal model of a polymer electrolyte fuel cell. *J. Power Sources* **163,** 793–806 (2007).

67. Wang, Y. & Feng, X. Analysis of Reaction Rates in the Cathode Electrode of Polymer Electrolyte Fuel Cell I. Single-Layer Electrodes. *J. Electrochem. Soc.* **155,** B1289 (2008).

68. Wang, Y. & Wang, C.-Y. Modeling Polymer Electrolyte Fuel Cells with Large Density and Velocity Changes. *J. Electrochem. Soc.* **152,** A445 (2005).

69. Wang, Y. & Wang, C.-Y. Simulation of flow and transport phenomena in a polymer electrolyte fuel cell under low-humidity operation. *J. Power Sources* **147,** 148–161 (2005).

70. Dutta, S., Shimpalee, S. & Van Zee, J. W. Three-dimensional numerical simulation of straight channel PEM fuel cells. *J. Appl. Electrochem.* 135–146 (2000).

71. Mazumder, S. & Cole, J. V. Rigorous 3-D Mathematical Modeling of PEM Fuel Cells I. Model Predictions without Liquid Water Transport. *J. Electrochem. Soc.* **150,** A1510 (2003).

72. Mazumder, S. & Cole, J. V. Rigorous 3-D Mathematical Modeling of PEM Fuel Cells II. Model Predictions with Liquid Water Transport. *J. Electrochem. Soc.* **150,** A1510 (2003).

73. Nam, J. H. & Kaviany, M. Effective diffusivity and water-saturation distribution in single- and two-layer PEMFC diffusion medium. *Int. J. Heat Mass Transf.* **46,** 4595–4611 (2003).

74. Pasaogullari, U. & Wang, C. Y. Liquid Water Transport in Gas Diffusion Layer of Polymer Electrolyte Fuel Cells. *J. Electrochem. Soc.* **151,** A399 (2004).

75. Birgersson, E., Noponen, M. & Vynnycky, M. Analysis of a Two-Phase Non-Isothermal Model for a PEFC. *J. Electrochem. Soc.* **152,** A1021 (2005).

76. Wang, Y. & Wang, C.-Y. A Nonisothermal, Two-Phase Model for Polymer Electrolyte Fuel Cells. *J. Electrochem. Soc.* **153,** A1193 (2006).

77. Meng, H. & Wang, C.-Y. Electron Transport in PEFCs. *J. Electrochem. Soc.* **151,** A358 (2004).

78. Wang, Y., Wang, C.-Y. & Chen, K. S. Elucidating differences between carbon paper and carbon cloth in polymer electrolyte fuel cells. *Electrochim. Acta* **52,** 3965–3975 (2007).

79. Benziger, J., Nehlsen, J., Blackwell, D., Brennan, T. & Itescu, J. Water flow in the gas diffusion layer of PEM fuel cells. *J. Memb. Sci.* **261,** 98–106 (2005).

80. Sinha, P. K. & Wang, C.-Y. Liquid water transport in a mixed-wet gas diffusion layer of a polymer electrolyte fuel cell. *Chem. Eng. Sci.* **63,** 1081–1091 (2008).

81. Wang, Y. Modeling of two-phase transport in the diffusion media of polymer electrolyte fuel cells. *J. Power Sources* **185,** 261–271 (2008).

82. Pasaogullari, U. & Wang, C.-Y. Two-Phase Modeling and Flooding Prediction of Polymer Electrolyte Fuel Cells. *J. Electrochem. Soc.* **152,** A380 (2005).

83. Lin, G. & Nguyen, T. Van. A Two-Dimensional Two-Phase Model of a PEM Fuel Cell. *J. Electrochem. Soc.* **153,** A372 (2006).

84. Gostick, J. T., Ioannidis, M. a., Fowler, M. W. & Pritzker, M. D. Pore network modeling of fibrous gas diffusion layers for polymer electrolyte membrane fuel cells. *J. Power Sources* **173,** 277–290 (2007).

85. Wang, C.-Y. Fundamental models for fuel cell engineering. *Chem. Rev.* **104,** 4727–65 (2004).

86. Gostick, J. T., Ioannidis, M. a., Fowler, M. W. & Pritzker, M. D. On the role of the microporous layer in PEMFC operation. *Electrochem. commun.* **11,** 576–579 (2009).

87. Pasaogullari, U., Wang, C.-Y. & Chen, K. S. Two-Phase Transport in Polymer Electrolyte Fuel Cells with Bilayer Cathode Gas Diffusion Media. *J. Electrochem. Soc.* **152,** A1574 (2005).

88. Weber, A. Z. & Newman, J. Effects of Microporous Layers in Polymer Electrolyte Fuel Cells. *J. Electrochem. Soc.* **152,** A677 (2005).

89. Natarajan, D. & Van Nguyen, T. A Two-Dimensional, Two-Phase, Multicomponent, Transient Model for the Cathode of a Proton Exchange Membrane Fuel Cell Using Conventional Gas Distributors. *J. Electrochem. Soc.* **148,** A1324 (2001).

90. Wang, Z. H., Wang, C. Y. & Chen, K. S. Two-phase flow and transport in the air cathode of proton exchange membrane fuel cells. *J. Power Sources* **94,** 40–50 (2001).

91. Leverett, M. Capillary behavior in porous solids. *Trans AIME* **142,** 69 (1941).

92. Fairweather, J. D., Cheung, P., St-Pierre, J. & Schwartz, D. T. A microfluidic approach for measuring capillary pressure in PEMFC gas diffusion layers. *Electrochem. commun.* **9,** 2340–2345 (2007).

93. Wood, D. L., Rulison, C. & Borup, R. L. Surface Properties of PEMFC Gas Diffusion Layers. *J. Electrochem. Soc.* **157,** B195 (2010).

94. Wood, D. L. & Borup, R. L. Estimation of Mass-Transport Overpotentials during Long-Term PEMFC Operation. *J. Electrochem. Soc.* **157,** B1251 (2010).

95. Li, X. & Sabir, I. Review of bipolar plates in PEM fuel cells: Flow-field designs. *Int. J. Hydrogen Energy* **30,** 359–371 (2005).

96. Jeon, D. The effect of serpentine flow-field designs on PEM fuel cell performance. *Int. J. Hydrogen Energy* **33,** 1052–1066 (2008).

97. Wang, X., Duan, Y., Yan, W. & Lee, D. Channel aspect ratio effect for serpentine proton exchange membrane fuel cell: role of sub-rib convection. *J. Power Sources* **193,** 684–690 (2009).

98. Wang, Y. Porous-Media Flow Fields for Polymer Electrolyte Fuel Cells. *J. Electrochem. Soc.* **156,** B1124 (2009).

99. Inoue, G., Matsukuma, Y. & Minemoto, M. Effect of gas channel depth on current density distribution of polymer electrolyte fuel cell by numerical analysis

including gas flow through gas diffusion layer. *J. Power Sources* **157,** 136–152 (2006).

100. Perng, S. & Wu, H. Non-isothermal transport phenomenon and cell performance of a cathodic PEM fuel cell with a baffle plate in a tapered channel. *Appl. Energy* **88,** 52–67 (2011).

101. Perng, S.-W., Wu, H.-W., Jue, T.-C. & Cheng, K.-C. Numerical predictions of a PEM fuel cell performance enhancement by a rectangular cylinder installed transversely in the flow channel. *Appl. Energy* **86,** 1541–1554 (2009).

102. Karvonen, S., Hottinen, T., Saarinen, J. & Himanen, O. Modeling of flow field in polymer electrolyte membrane fuel cell. *J. Power Sources* **161,** 876–884 (2006).

103. Tüber, K., Pócza, D. & Hebling, C. Visualization of water buildup in the cathode of a transparent PEM fuel cell. *J. Power Sources* **124,** 403–414 (2003).

104. Bazylak, A. Liquid water visualization in PEM fuel cells: A review. *Int. J. Hydrogen Energy* **34,** 3845–3857 (2009).

105. Zhang, F. Y., Yang, X. G. & Wang, C. Y. Liquid Water Removal from a Polymer Electrolyte Fuel Cell. *J. Electrochem. Soc.* **153,** A225 (2006).

106. Yang, X. G., Zhang, F. Y., Lubawy, a. L. & Wang, C. Y. Visualization of Liquid Water Transport in a PEFC. *Electrochem. Solid-State Lett.* **7,** A408 (2004).

107. Adrianowycz, O. Next Generation Bipolar Plates for Automotive PEM Fuel Cells. *DOE 2009 Annu. Prog. Rep. V. Fuel cells* (2010). doi:10.2172/975485

108. Brady, M. P., Weisbrod, K. & Paulauskas, I. Preferential thermal nitridation to form pin-hole free Cr-nitrides to protect proton exchange membrane fuel cell metallic bipolar plates. *Scr. Mater.* **50,** 1017–1022 (2004).

109. Brady, M. *et al.* Growth of Cr-Nitrides on commercial Ni–Cr and Fe–Cr base alloys to protect PEMFC bipolar plates. *Int. J. Hydrogen Energy* **32,** 3778–3788 (2007).

110. Brady, M. & Toops, T. *Nitrided metallic bipolar plates*. *DOE 2009 Annu. Prog. Rep. V. Fuel cells* (2009). at <http://www.hydrogen.energy.gov/pdfs/review10/fc022_tortorelli_2010_o_web.pdf>

111. Jiao, K., Park, J. & Li, X. Experimental investigations on liquid water removal from the gas diffusion layer by reactant flow in a PEM fuel cell. *Appl. Energy* **87,** 2770–2777 (2010).

112. Spernjak, D., Advani, S. & Prasad, A. K. Experimental Investigation of Liquid Water Formation and Transport in a Transparent Single-Serpentine PEM Fuel Cell. *ASME 2006 Fourth Int. Conf. Fuel Cell Sci. Eng. Technol. Parts A B* **2006,** 453–461 (2006).

113. Chen, K. S., Hickner, M. A. & Noble, D. R. Simplified models for predicting the onset of liquid water droplet instability at the gas diffusion layer/gas flow channel interface. *Int. J. Energy Res.* **29,** 1113–1132 (2005).

114. Zhu, X., Sui, P. C. & Djilali, N. Three-dimensional numerical simulations of water droplet dynamics in a PEMFC gas channel. *J. Power Sources* **181,** 101–115 (2008).

115. He, G., Ming, P., Zhao, Z., Abudula, A. & Xiao, Y. A two-fluid model for two-phase flow in PEMFCs. *J. Power Sources* **163,** 864–873 (2007).

116. Zhan, Z., Xiao, J., Pan, M. & Yuan, R. Characteristics of droplet and film water motion in the flow channels of polymer electrolyte membrane fuel cells. *J. Power Sources* **160,** 1–9 (2006).

117. Cai, Y. H., Hu, J., Ma, H. P., Yi, B. L. & Zhang, H. M. Effects of hydrophilic/hydrophobic properties on the water behavior in the micro-channels of a proton exchange membrane fuel cell. *J. Power Sources* **161,** 843–848 (2006).

118. Park, J. W., Jiao, K. & Li, X. Numerical investigations on liquid water removal from the porous gas diffusion layer by reactant flow. *Appl. Energy* **87,** 2180–2186 (2010).

119. Chen, K. Modeling water-droplet detachment from GDL/channel interface in PEM fuel cells. *ASME 2008 6th Int. Conf. Fuel Cell Sci. Eng. Technol.* 797–803 (2008). doi:10.1115/FuelCell2008-65137

120. Promislow, K. & Wetton, B. A simple, mathematical model of thermal coupling in fuel cell stacks. *J. Power Sources* **150,** 129–135 (2005).

121. Berg, P. Electrical coupling in proton exchange membrane fuel cell stacks: mathematical and computational modelling. *IMA J. Appl. Math.* **71,** 241–261 (2005).

122. Kim, G., St-Pierre, J., Promislow, K. & Wetton, B. Electrical coupling in proton exchange membrane fuel cell stacks. *J. Power Sources* **152,** 210–217 (2005).

123. Chang, P. A. C., St-Pierre, J., Stumper, J. & Wetton, B. Flow distribution in proton exchange membrane fuel cell stacks. *J. Power Sources* **162,** 340–355 (2006).

124. Baschuk, J. & Li, X. Mathematical model of a PEM fuel cell incorporating CO poisoning and O2(air) bleeding. *Int J Glob. Energy Issues* **20,** 245–76 (2003).

125. Karimi, G., Baschuk, J. J. & Li, X. Performance analysis and optimization of PEM fuel cell stacks using flow network approach. *J. Power Sources* **147,** 162–177 (2005).

126. Chen, C.-H., Jung, S.-P. & Yen, S.-C. Flow distribution in the manifold of PEM fuel cell stack. *J. Power Sources* **162,** 340–55 (2006).

127. Yu, X., Zhou, B. & Sobiesiak, A. Water and thermal management for Ballard PEM fuel cell stack. *J. Power Sources* **147,** 184–195 (2005).

128. Park, J. & Li, X. Effect of flow and temperature distribution on the performance of a PEM fuel cell stack. *J. Power Sources* **162,** 444–459 (2006).

129. Chang, P., Kim, G.-S., Promislow, K. & Wetton, B. Reduced dimensional computational models of polymer electrolyte membrane fuel cell stacks. *J. Comput. Phys.* **223,** 797–821 (2007).

130. Zawodzinski, T. A. *et al.* A Comparative Study of Water Uptake By and Transport Through Ionomeric Fuel Cell Membranes. *J. Electrochem. Soc.* **140,** 1981–1985 (1993).

131. Zawodzinski, T. A. *et al.* Water Uptake by and Transport Through Nation117 Membranes. *J. Electrochem. Soc.* **140,** 1041–1047 (1993).

132. Zawodzinski, T. A., Davey, J., Valerio, J. & Gottesfeld, S. The Water Content Dependence Electro-osmotic Drag in Proton-Conducting Polymer Electrolytes. *Electrochim. Acta* **40,** 297–302 (1995).

133. Janssen, G. J. M. & Overvelde, M. L. J. Water transport in the proton-exchange-membrane fuel cell : measurements of the effective drag coefficient. *J. Power Sources* **101,** 117–125 (2001).

134. Hickner, M. A., Fujimoto, C. H. & Cornelius, C. J. Transport in sulfonated poly(phenylene)s: Proton conductivity, permeability, and the state of water. *Polymer.* **47,** 4238–4244 (2006).

135. Stumper, J., Löhr, M. & Hamada, S. Diagnostic tools for liquid water in PEM fuel cells. *J. Power Sources* **143,** 150–157 (2005).

136. Okada, T. Theory for water management in membranes for polymer electrolyte fuel cells Part 1 . The effect of impurity ions at the anode side on the membrane performances. *J. Electroanalytical Chemistry* **465,** 1–17 (1999).

137. Knights, S. D., Colbow, K. M., St-Pierre, J. & Wilkinson, D. P. Aging mechanisms and lifetime of PEFC and DMFC. *J. Power Sources* **127,** 127–134 (2004).

138. Sone, Y., Ekdunge, P. & Simonsson, D. Proton Conductivily of Nafion 117 as Measured by a Four-Electrode AC Impedance Method. *J. eletrochem. Soc.* **143,** 1254–1259 (1996).

139. Meng, H. & Wang, C.-Y. Model of Two-Phase Flow and Flooding Dynamics in Polymer Electrolyte Fuel Cells. *J. Electrochem. Soc.* **152,** A1733 (2005).

140. Natarajan, D. & Van Nguyen, T. Current distribution in PEM fuel cells. Part 1: Oxygen and fuel flow rate effects. *AIChE J.* **51,** 2587–2598 (2005).

141. Barbir, F., Gorgun, H. & Wang, X. Relationship between pressure drop and cell resistance as a diagnostic tool for PEM fuel cells. *J. Power Sources* **141,** 96–101 (2005).

142. Pasaogullari, U., Wang, C.-Y. & Chen, K. S. Two-Phase Transport in Polymer Electrolyte Fuel Cells with Bilayer Cathode Gas Diffusion Media. *J. Electrochem. Soc.* **152,** A1574 (2005).

143. Eikerling, M., Kornyshev, A. A., Kucernak, A. R., Platonov, A. & Man, C. Water in polymer electrolyte fuel cells : Friend or foe ? *Phys. Today* (2006).

144. Rodatz, P., Büchi, F., Onder, C. & Guzzella, L. Operational aspects of a large PEFC stack under practical conditions. *J. Power Sources* **128,** 208–217 (2004).

145. Eckl, R., Zehtner, W., Leu, C. & Wagner, U. Experimental analysis of water management in a self-humidifying polymer electrolyte fuel cell stack. *J. Power Sources* **138,** 137–144 (2004).

146. Li, G. & Pickup, P. G. Dependence of Electrode Overpotentials in PEM Fuel Cells on the Placement of the Reference Electrode. *Electrochem. Solid-State Lett.* **9,** A249 (2006).

147. Nguyen, T. V & White, R. E. A Water and Heat Management Model for Proton-Exchange-Membrane Fuel Cells. *J. eletrochem. Soc.* **140,** 2178 (1993).

148. Le Canut, J.-M., Abouatallah, R. M. & Harrington, D. A. Detection of Membrane Drying, Fuel Cell Flooding, and Anode Catalyst Poisoning on PEMFC Stacks by Electrochemical Impedance Spectroscopy. *J. Electrochem. Soc.* **153,** A857 (2006).

149. Wang, Y. & Wang, C.-Y. Dynamics of polymer electrolyte fuel cells undergoing load changes. *Electrochim. Acta* **51,** 3924–3933 (2006).

150. Aspects, F. Operating Proton Exchange Membrane Fuel Cells Without External Humidification of the Reactant Gases Fundamental Aspects. **144,** 2767–2772 (1997).

151. Huang, X. *et al.* Mechanical Endurance of Polymer Electrolyte Membrane and PEM Fuel Cell Durability. 2346–2357 (2006). doi:10.1002/polb

152. Yu, J., Matsuura, T., Yoshikawa, Y., Islam, M. N. & Hori, M. In Situ Analysis of Performance Degradation of a PEMFC under Nonsaturated Humidification. *Electrochem. Solid-State Lett.* **8,** A156 (2005).

153. He, W., Lin, G. & Van Nguyen, T. Diagnostic tool to detect electrode flooding in proton-exchange-membrane fuel cells. *AIChE J.* **49,** 3221–3228 (2003).

154. Li, H. *et al.* A review of water flooding issues in the proton exchange membrane fuel cell. *J. Power Sources* **178,** 103–117 (2008).

155. Sridhar, P., Perumal, R., Rajalakshmi, N., Raja, M. & Dhathathreyan, K. S. Humidification studies on polymer electrolyte membrane fuel cell. *J. Power Sources* **101,** 72–78 (2001).

156. Weber, A. Z. & Newman, J. *Modeling transport in polymer-electrolyte fuel cells. Chem. Rev.* **104,** 4679–726 (2004).

157. Um, S. & Wang, C.-Y. Computational study of water transport in proton exchange membrane fuel cells. *J. Power Sources* **156,** 211–223 (2006).

158. Piela, P., Springer, T. E., Davey, J. & Zelenay, P. Direct Measurement of iR-Free Individual-Electrode Overpotentials in Polymer Electrolyte Fuel Cells. *J. Phys. Chem. C* **111,** 6512–6523 (2007).

159. Wei, Z. D. *et al.* MnO2–Pt/C composite electrodes for preventing voltage reversal effects with polymer electrolyte membrane fuel cells. *J. Power Sources* **160,** 246–251 (2006).

160. Ji, M. B., Wei, Z. D., Chen, S. G. & Li, L. A Novel Antiflooding Electrode for Proton Exchange Membrane Fuel Cells. *J. Phys. Chem. C* **113,** 765–771 (2009).

161. Ge, S. & Wang, C.-Y. Liquid Water Formation and Transport in the PEFC Anode. *J. Electrochem. Soc.* **154,** B998 (2007).

162. Costamagna, P. & Srinivasan, S. Quantum jumps in the PEMFC science and technology from the 1960 to the year 2000 part I. *J Power Source* **102,** 242–54 (2001).

163. Appleby, A., Fuel cell handbook. (1988). at <http://www.osti.gov/energycitations/product.biblio.jsp?osti_id=5616450>

164. De Grotthuss, C., *Ann Chim* 58–54 (1806). at <http://scholar.google.com/scholar?hl=en&btnG=Search&q=intitle:Ann+Chim#0>

165. Breslaul, B. R. & Miller, I. F. A Hydrodynamic Model for Electroosmosis. *Ind. Eng. Chem. Fundam* **10,** (1971).

166. Kreuer, K.-D., Paddison, S. J., Spohr, E. & Schuster, M. Transport in proton conductors for fuel-cell applications: simulations, elementary reactions, and phenomenology. *Chem. Rev.* **104,** 4637–78 (2004).

167. Deluca, N. W. & Elabd, Y. A. Polymer Electrolyte Membranes for the Direct Methanol Fuel Cell : A Review. 2201–2225 (2006). doi:10.1002/polb

168. Hogarth, W. H. J., Diniz da Costa, J. C. & Lu, G. Q. (Max. Solid acid membranes for high temperature (¿140° C) proton exchange membrane fuel cells. *J. Power Sources* **142,** 223–237 (2005).

169. Souzy, R. & Ameduri, B. Functional fluoropolymers for fuel cell membranes. *Prog. Polym. Sci.* **30,** 644–687 (2005).

170. Kariduraganavar, M. Y., Nagarale, R. K., Kittur, A. A. & Kulkarni, S. S. Ion-exchange membranes: preparative methods for electrodialysis and fuel cell applications. *Desalination* **197,** 225–246 (2006).

171. Rikukawa, M. & Sanui, K. Proton-conducting polymer electrolyte membranes based on hydrocarbon polymers. *Prog. Polym. Sci.* **25,** 1463–1502 (2000).

172. Higashihara, T., Matsumoto, K. & Ueda, M. Sulfonated aromatic hydrocarbon polymers as proton exchange membranes for fuel cells. *Polymer (Guildf).* **50,** 5341–5357 (2009).

173. Soczka-Guth, T. patent. (1999).

174. Hong, Y. T. *et al.* Improvement of electrochemical performances of sulfonated poly(arylene ether sulfone) via incorporation of sulfonated poly(arylene ether benzimidazole). *J. Power Sources* **175,** 724–731 (2008).

175. Lee, J. K., Li, W. & Manthiram, A. Poly(arylene ether sulfone)s containing pendant sulfonic acid groups as membrane materials for direct methanol fuel cells. *J. Memb. Sci.* **330,** 73–79 (2009).

176. Wen, S., Gong, C., Tsen, W.-C., Shu, Y.-C. & Tsai, F.-C. Sulfonated poly(ether sulfone) (SPES)/boron phosphate (BPO4) composite membranes for high-temperature proton-exchange membrane fuel cells. *Int. J. Hydrogen Energy* **34,** 8982–8991 (2009).

177. Gowariker, V., Vishwanathan, N. & Sridhar, J. Polymer science. (1999).

178. Xu, T., Wu, D. & Wu, L. Poly(2,6-dimethyl-1,4-phenylene oxide) (PPO)—A versatile starting polymer for proton conductive membranes (PCMs). *Prog. Polym. Sci.* **33,** 894–915 (2008).

179. Xu, T., Woo, J.-J., Seo, S.-J. & Moon, S.-H. In situ polymerization: A novel route for thermally stable proton-conductive membranes. *J. Memb. Sci.* **325,** 209–216 (2008).

180. Nafion material safety data sheet (MSDS). at <http://ion-power.com/nafion/naf001.html:2001>

181. Larminie, J. & Dicks, A. in (2000). doi:10.1016/S0378-7753(00)00571-1

182. Sakai, T., Takenako, H., Wakabayashi, N., Kawami, Y. & Torikai, E. Gas Permeation Properties of Solid Polymer Electrolyte (SPE) Membranes. **117,**

183. Watkins, D. Fuel cell systems. (1993).

184. Smitha, B., Sridhar, S. & Khan, A. Synthesis and characterization of proton conducting polymer membranes for fuel cells. *J. Memb. Sci.* **225,** 63–76 (2003).

185. Smitha, B., Sridhar, S. & Khan, A. Polyelectrolyte complexes of chitosan and poly(acrylic acid) for fuel cell applications. *Macromolecules* **37,** 2233 (2004).

186. Ramírez-Salgado, J. Study of basic biopolymer as proton membrane for fuel cell systems. *Electrochim. Acta* **52,** 3766–3778 (2007).

187. Colicchio, I., Wen, F., Keul, H., Simon, U. & Moeller, M. Sulfonated poly(ether ether ketone)–silica membranes doped with phosphotungstic acid. Morphology and proton conductivity. *J. Memb. Sci.* **326,** 45–57 (2009).

188. Mahreni, A., Mohamad, A. B., Kadhum, A. A. H., Daud, W. R. W. & Iyuke, S. E. Nafion/silicon oxide/phosphotungstic acid nanocomposite membrane with enhanced proton conductivity. *J. Memb. Sci.* **327,** 32–40 (2009).

189. Price, A. Proceedings of the ICE - Civil Engineering. in 4–11 (2005).

190. GILEADI, E. *et al.* Electrochemically Regenerative Hydrogen Chlorine Energy-Storage System For Electric Utilities. *J. Power Sources* **2,** 191–200 (1977).

191. Srinivasan, S., Yeo, R. S. & Beaufrere, A. in Proc. Second Information Meeting for Hydrogen Contractors in DOE Hydrogen Energy Program. in (1976).

192. Beaufrere, A., Yeo, R. S., Srinivasan, S., McElroy, J. & Hart, G. inter-Sot. in *12th Inter- Sot. Energy Conv. Eng. Conf.* (1977). doi:779148

193. Chin, D. T., Yeo, R. S., McBreen, J. & Srinivasan, S. An Electrochemically Regenerative Hydrogen-Chlorine Energy Storage System. *J. eletrochem. Soc.* **126,** 714 (1979).

194. Kosek, J. A. & Laconti, A. B. Advanced Hydrogen Electrode For A Hydrogen Bromine Battery. *J. Power Sources* **22,** 293–300 (1988).

195. Li, W., Dahn, J. R. & Wainwright, D. S. Rechargeable lithium batteries with aqueous electrolytes. *Science* **264,** 1115–8 (1994).

196. Weber, A. Z. *et al.* Redox flow batteries: a review. *J. Appl. Electrochem.* **41,** 1137–1164 (2011).

197. Heintz, A. & Illenberger, C. Diffusion coefficients of Br2 in cation exchange membranes. *J. Memb. Sci.* **113,** 175–181 (1996).

198. Goor-Dar, M., Travitsky, N. & Peled, E. Study of hydrogen redox reactions on platinum nanoparticles in concentrated HBr solutions. *J. Power Sources* **197,** 111–115 (2012).

199. Morrissey, P., Vesely, D. & Cooley, G. Stability of sulphonate type membranes in aqueous bromine/bromide environments. *J. Memb. Sci.* **247,** 169–178 (2005).

200. Livshits, V., Ulus, a. & Peled, E. High-power H2/Br2 fuel cell. *Electrochem. commun.* **8,** 1358–1362 (2006).

201. Peled, E., Duvdevani, T., Aharon, A. & Melman, A. A Direct Methanol Fuel Cell Based on a Novel Low-Cost Nanoporous Proton-Conducting Membrane. *Polymer (Guildf).* **3,** 525–528 (2000).

202. Peled, E., Duvdevani, T., Aharon, a. & Melman, a. New Fuels as Alternatives to Methanol for Direct Oxidation Fuel Cells. *Electrochem. Solid-State Lett.* **4,** A38 (2001).

203. Peled, E., Duvdevani, T. & Melman, A. A Novel Proton-Conducting Membrane. **i,** 210–211 (1998).

204. Price, A., Bartley, S. & Male, S. A novel approach to utility scale energy storage. *POWER Eng. J.* 122–129 (2000).

205. Ge, S. H., Yi, B. L. & Zhang, H. M. Study of a high power density sodium polysulfide/bromine energy storage cell. *J. Appl. Electrochem.* **34,** 181–185 (2004).

206. Price, A. & Mccarthy, L. *Power generation using renewables and the Regenesys energy storage system*. *... E Semin Publ,(15, Power Gener. by Renewables)* (2000). at <http://scholar.google.com/scholar?hl=en&btnG=Search&q=intitle:Power+generation+using+renewables+and+the+regenesys+energy+storage+system#3>

207. Zhao, P., Zhang, H., Zhou, H. & Yi, B. Nickel foam and carbon felt applications for sodium polysulfide/bromine redox flow battery electrodes. *Electrochim. Acta* **51,** 1091–1098 (2005).

208. Zawodzinski, T. A., Gottesfeld, S., Shoichet, S. & McCarthy, T. J. The contact angle between water and the surface of perfluorosulphonic acid membranes. *J. Appl. Electrochem.* **23,** (1993).

209. Kusoglu, A., Hexemer, A., Jiang, R., Gittleman, C. S. & Weber, A. Z. Effect of compression on PFSA-ionomer morphology and predicted conductivity changes. *J. Memb. Sci.* **421-422,** 283–291 (2012).

210. Yeo, R. S. Transport Properties of Nafion Membranes in Electrochemically Regenerative Hydrogen/Halogen Cells. *J. Electrochem. Soc.* **126,** 1682 (1979).

211. Yeo, R. S. A Hydrogen-Bromine Cell for Energy Storage Applications. *J. Electrochem. Soc.* **127,** 549 (1980).

212. Yeo, R. S. Transport Properties of Nafion Membranes in Electrochemically Regenerative Hydrogen/Halogen Cells. *J. Electrochem. Soc.* **126,** 1682 (1979).

213. Cho, K. T., Ridgway, P., Weber, A., Haussener, S., Battaglia, V., Srinivasan, V., High Performance Hydrogen/Bromine Redox Flow Battery for Grid-Scale Energy Storage. *J. Electrochem. Soc.* **159,** A1806–A1815 (2012).

214. Aaron, D., Tang, Z., Papandrew, A. B. & Zawodzinski, T. A. Polarization curve analysis of all-vanadium redox flow batteries. *J. Appl. Electrochem.* **41,** 1175–1182 (2011).

215. Aaron, D., Sun, C.-N., Bright, M., Papandrew, A., Mench, M., Zawodzinski, T., In Situ Kinetics Studies in All-Vanadium Redox Flow Batteries. *ECS Electrochem. Lett.* **2,** A29–A31 (2013).

216. Tang, Z., Keith, R., Aaron, D., Lawton, J., Papandrew, A., Zawodzinski, T., Proton Exchange Membrane Performance Characterization in VRFB. *ECS Trans.* **41,** 25–34 (2012).

217. Aaron, D., Liu, Q., Tang, Z., Grim, G., Papandrew, A., Turhan, A., Zawodzinski, T., Mench, M. Dramatic performance gains in vanadium redox flow batteries through modified cell architecture. *J. Power Sources* **206,** 450–453 (2012).

218. Tang, Z., Aaron, D. S., Papandrew, A. B. & Zawodzinski, T. A. Monitoring the State of Charge of Operating Vanadium Redox Flow Batteries Zhijiang Tang. *ECS Trans.* **41,** 1–9 (2012).

219. Lefebvre, M. C., Martin, R. B. & Pickup, P. G. Characterization of Ionic Conductivity Profiles within Proton Exchange Membrane Fuel Cell Gas Diffusion Electrodes by Impedance Spectroscopy. *Electrochemical and Solid-State Letters* **2,** 259–261 (1999).

220. Springer, E., Zawodzinski, A., Wilson, M. S. & Golfesfeld, S. Characterization of Polymer Electrolyte Fuel Cells Using AC Impedance Spectroscopy. *J. Electrochem. Soc.* **143,** 587–599 (1996).

221. Gabrielli, C., *Electrochemical Impedance Spectroscopy: Principles, Instrumentation, and Application.* 243 (1995).

222. Conway, B. E., Phillips, Y. & Qian, S. Y. Surface Electrochemistry and Kinetics of Anodic Bromine Formation at Platinum. *J. chem. soc faraday trans.* **91,** 283–293 (1995).

223. Dabosi, F., Jacquet, F. & Gaset, A. Electrochemical impedance study of the reaction mechanism for electro-oxidation of isosorbide. *J. Applied Electrochemistry* **21,** 690–696 (1991).

224. Loo, B. H. & Lee, Y. G. Surface-Enhanced Raman Spectroscopy of Platinum Enhanced Light Scattering of Electrogenerated Bromine and Tribromide Ions Coadsorbed on a Platinum Electrode. *American Chemical Society*, **4159,** 706–709 (1984).

225. Himanen, O., Hottinen, T., Mikkola, M. & Saarinen, V. Characterization of membrane electrode assembly with hydrogen–hydrogen cell and ac-impedance spectroscopy. *Electrochim. Acta* **52,** 206–214 (2006).

Vita

Yujia Bai was born in Shenyang, China. He attended TongZe Elementary School and continued to Shenyang Foreign Language Middle School and Liaoning Shiyan High School. After graduation, he left his hometown to Dalian University of Technology in Dalian, China. He chose to join chemical engineering department in 2005, majoring in polymer science and engineering. He received his Bachelor degree in 2009 and accepted the offer from University of Tennessee for further graduate study and research in Knoxville, Chemical and Biomolecular Engineering department. He joined the Dr. Thomas Zawodzinski group and has worked in the realm of electrochemistry since 2009.